



Peer Reviewed

Title:

Surface Plasmon Assisted High Resolution and High Contrast Optical Imaging

Author:

[Wei, Feifei](#)

Acceptance Date:

2014

Series:

[UC San Diego Electronic Theses and Dissertations](#)

Degree:

Ph. D., [Physics](#)UC San Diego

Permalink:

<http://escholarship.org/uc/item/9qh6r7d4>

Local Identifier:

b8139085

Abstract:

This thesis presents theoretical and/or experimental demonstrations of several Surface Plasmon (SP) assisted high-resolution or high-contrast microscopy techniques, including Plasmonic Structured Illumination Microscopy (PSIM), Plasmonic Darkfield (PDF) Microscopy, Plasmonic Evanescent field (PEF) Microscopy and Localized Surface Plasmon Assisted Contrast (LSPAC) Microscopy. The PSIM combines tunable SP interference with structured illumination microscopy (SIM) to achieve super-resolution. By replacing the laser interference fringes in conventional SIM with SP interference (SPI) patterns, PSIM possesses higher image resolving power compared to that of SIM. Both theoretical and experimental concept demonstration shows more than 2.6-fold resolution improvement compared with conventional epi-fluorescence microscopy, whereas SIM only achieves about 2 times resolution improvement. This new PSIM technique is a wide field super resolution imaging technique and potentially could be used for high speed biomedical imaging. The PDF microscopy is a compact, alignment-free dark-field microscopy technique. Experimental results show that it is capable of forming dark-field images of the specimens by utilizing a highly integrated chip-scale plasmonic condenser. The PEF microscopy is a similar technique that exploits the extremely short z decay length of high wave vector SP waves for achieving selective excitation of fluorophores very close to the substrate. Both the PDF and PEF microscopy possess high z resolution and high imaging contrast and are suitable for the dynamics study near the contact regions of living cells and the substrate. The LSPAC microscopy combines localized surface plasmon resonance (LSPR) and dark field microscopy technique for high contrast purpose. Because of the sensitive response of LSPR with the change of surrounding media refractive indices, this technique can convert the refractive index variation to the scattering intensity difference and form a high contrast, diffraction limited image of a thin unstained transparent specimen with small refractive index variation



eScholarship
University of California

eScholarship provides open access, scholarly publishing services to the University of California and delivers a dynamic research platform to scholars worldwide.

Copyright Information:

All rights reserved unless otherwise indicated. Contact the author or original publisher for any necessary permissions. eScholarship is not the copyright owner for deposited works. Learn more at http://www.escholarship.org/help_copyright.html#reuse



eScholarship
University of California

eScholarship provides open access, scholarly publishing services to the University of California and delivers a dynamic research platform to scholars worldwide.

UNIVERSITY OF CALIFORNIA, SAN DIEGO

Surface Plasmon Assisted High Resolution and High Contrast Optical Imaging

A dissertation submitted in partial satisfaction of the
requirements for the degree
Doctor of Philosophy

in

Physics

by

Feifei Wei

Committee in charge:

Professor Zhaowei Liu, Chair
Professor Oleg Shpyrko, Co-Chair
Professor Yu-Hwa Lo
Professor Sunil K. Sinha
Professor Douglas E. Smith

2014

Copyright
Feifei Wei, 2014
All rights reserved.

The dissertation of Feifei Wei is approved, and it is acceptable in quality and form for publication on microfilm and electronically:

Co-Chair

Chair

University of California, San Diego

2014

EPIGRAPH

We're here to put a dent in the universe.

—Steve Jobs

TABLE OF CONTENTS

Signature Page	iii
Epigraph	iv
Table of Contents	v
List of Figures	viii
Acknowledgements	xii
Vita	xiv
Abstract of the Dissertation	xv
Chapter 1 Introduction	1
1.1 Background of imaging system and diffraction limit	1
1.1.1 Coherent and incoherent imaging system	1
1.1.2 Diffraction limit	3
1.2 Review of advanced microscopy techniques	3
1.2.1 Traditional methods of improving the resolving power	4
1.2.2 Super-resolution fluorescence microscopy techniques	5
1.2.3 Structured Illumination Microscopy SIM	6
1.3 Background of surface plasmon (SP)	8
1.4 This thesis	11
Chapter 2 Theory of plasmonic structured illumination microscopy (PSIM)	13
2.1 Principles of PSIM	13
2.2 PSIM image reconstruction algrithom	15
2.3 Numerical demonstration of PSIM concept	18
2.3.1 Thick plasmonic substrate and its imaging capability demonstration	18
2.3.2 Thin plasmonic substrate and its imaging capability demonstration	21
2.4 Discussion	24
2.5 Conclusion	25
Chapter 3 Experimental demonstration of PSIM	27
3.1 Instrument development for PSIM	27
3.1.1 PSIM system overview	27
3.1.2 Light source module and illumination angle control module	27

3.1.3	PSIM system synchronization and data acquisition	31
3.1.4	Illumination angle characterization module	31
3.2	Plasmonic substrate design and fabrication	33
3.2.1	Plasmonic substrate design	34
3.2.2	Plasmonic substrate fabrication	36
3.3	Experimental demonstration of the SPI lateral translation	36
3.3.1	PSIM sample preparation and measurements	36
3.3.2	Demonstration of the lateral translation of the SPI	38
3.4	Experimental demonstration of PSIM super-resolution imaging capability	39
3.4.1	Super-resolution image reconstruction through Fourier space based algorithm	39
3.4.2	Super-resolution image reconstruction through Blind-SIM based algorithm	41
3.5	Discussion	46
3.6	Conclusion	49
 Chapter 4	 Plasmonic dark field (PDF) microscopy and plasmonic evanescent field (PEF) microscopy	50
4.1	Introduction	50
4.1.1	Background of dark field microscopy	50
4.1.2	Background of total internal reflection fluorescence (TIRF) microscopy	51
4.2	Experimental demonstration of PDF microscopy	53
4.2.1	Principles of PDF microscopy	53
4.2.2	Experimental demonstration of OLED-based PDF microscopy	55
4.2.3	Discussion	58
4.3	Numerical demonstration of PEF microscopy	63
4.3.1	Principles of PEF microscopy	63
4.3.2	Numerical verification of a metamaterial substrate	65
4.4	Conclusion	67
 Chapter 5	 Localized SP assisted contrast (LSPAC) microscopy	69
5.1	Background	69
5.2	Principles of LSPAC microscopy	71
5.3	Experimental demonstration of LSPAC	73
5.3.1	Sample fabrication	73
5.3.2	High contrast imaging capability demonstration for uniform thin object	73
5.3.3	High contrast imaging capability demonstration for non-uniform thin object	75

5.3.4	High contrast imaging capability demonstration using bio-specimens	78
5.4	Discussion	79
5.5	Conclusion	80
Chapter 6	Future directions and summary	81
6.1	Future directions	81
6.1.1	Future directions for PSIM	81
6.1.2	Future directions for PDF microscopy, PEF mi- croscopy and LSPAC microscopy	83
6.2	Thesis summary	84

LIST OF FIGURES

<p>Figure 1.1: Concept of resolution enhancement in SIM. (a) An example object with small features; (b) a structured illumination pattern; (c) Moiré fringes formed by superposing the structured illumination pattern with the object; (d) SIM fourier space representation.</p> <p>Figure 1.2: Schematic of the dispersion curves of the photon (red line) in the dielectric and surface plasmon (blue line).</p> <p>Figure 1.3: Cross-section view of various SP coupling structures. (a) A prism coupling structure; (b) a grating coupling structure; (c) a defect coupling structure; (d) a near field coupling structure. The gray areas corresponds to the plasmonic material.</p> <p>Figure 2.1: Illustration of the SIM and PSIM principles. (a) SIM and (b) PSIM resolution improvement representation in Fourier space. The dashed circles represent the Fourier space region detectable by SIM and PSIM respectively.</p> <p>Figure 2.2: Numerical demonstration of the lateral shift of the SP interference pattern. (a-c) The time-averaged electrical energy density distribution of the SP interference pattern with incident angle equal to 0°, 4.6°, and 8.0°, respectively.</p> <p>Figure 2.3: Image space and Fourier space representation of SIM.</p> <p>Figure 2.4: Numerical demonstrations of the SP interference at thick film-dielectric interface. (a) Structure configuration; (b,c) time-averaged electric energy density distribution excited by 563 and 390 nm light; (d,e) Fourier transform of (b,c) respectively.</p> <p>Figure 2.5: PSF of (a) epi-fluorescence microscopy, (b) PSIM using 563 nm, (c) PSIM using both 563 and 390 nm, (d) PSIM using 390 nm excitation light. (e-h) Imaging performance for (a-d). (i-l) Corresponding k space representations.</p> <p>Figure 2.6: (a) Structure and SP interference pattern (time-averaged electric energy density distribution) excited by 442 nm light; (b) Fourier transform of interference pattern measured 20 nm under Ag film.</p> <p>Figure 2.7: PSIM imaging ability demonstration. (a) Conventional epi-fluorescence and (b-d) Reconstructed images; (e-h) Corresponding k space representations. Different colors represents the information obtained from different orders of the illumination patterns.</p> <p>Figure 3.1: Schematics of the automated PSIM system. Modules 1-4 represent the light source module, the illumination angle control module, the fluorescence image detection module and the illumination angle characterization module, respectively.</p>	<p>7</p> <p>9</p> <p>11</p> <p>14</p> <p>15</p> <p>16</p> <p>19</p> <p>20</p> <p>22</p> <p>23</p> <p>28</p>
--	---

Figure 3.2: Photos of the PSIM system with four modules highlighted by solid squares. (a) Light source module. (b) Front view. (c) Side view.	30
Figure 3.3: (a) Photo of the illumination angle control module. (b) Schematic view of the sample region.	31
Figure 3.4: (a) Time sequence of the synchronization signals; (b) Illumination angle in x-z plane vs. the control signal voltage of the s2 scanning mirror; (c) a photo of the control electronics.	32
Figure 3.5: (a) Schematics and (b) photo of the illumination angle characterization system.	33
Figure 3.6: (a) The dispersion curve for SP mode supported. (b) Directly transmitted E-field vs. Ag thickness for perpendicular illumination. (c) The intensity Z decay length vs. SP mode wave vector with water as surrounding media ($n=1.33$).	35
Figure 3.7: Major procedures for substrate fabrication. The blue squares represent the electron beam resist or nano-imprint resist, and the dark gray squares represent the deposited Ag film.	37
Figure 3.8: The plasmonic substrate characterization. (a) Bright field and (b) the sanning electron microscopy (SEM) image of the substrate. (c) The magnified SEM image of one unit cell and (d) further magnified SEM image of the slits.	37
Figure 3.9: (a) Schematics of the SPI lateral translation characterization configuration. (b-c) Fluorescence intensity vs. illumination angle change. (d-i) Six PSIM fluorescence images excited by 6 SPI patterns.	40
Figure 3.10: (a) Conventional epi-fluorescence, (b) reconstructed PSIM and (d) the SEM image of the object; (d) Fourier transform of (b); (e) Cross section comparison along line 1 (top) and line 2 (bottom).	41
Figure 3.11: The workflow of the Blind-SIM algorithm.	42
Figure 3.12: (a-e) The recovered object at different iteration steps; (f) The recovered object after applying additional Wiener filter estimated by the theoretical super-resolution psf; (g) The value of the cost function vs. the number of iterations.	44
Figure 3.13: (a) Conventional epi-fluorescence, (b) reconstructed PSIM, and (c) the corresponding SEM image. (d-e) Fourier transform of (a-b). (f) Fluorescence intensity cross-section comparison of the single bead.	45
Figure 3.14: (a) Epi-fluorescence image, (b) its deconvolution. (c) The reconstructed PSIM image. (d-j) Images within the white dashed and solid line boxes. (g, k) The corresponding SEM images. (l-m) The fluorescence intensity cross-section comparison.	47

Figure 4.1:	Schematics of (a) transmission dark field microscopy and (b) reflection dark field microscopy.	51
Figure 4.2:	Schematics of TIRF microscopy. (a) TIRF microscopy working principle; (b) TIRF microscopy illumination and detection configuration for objective based TIRF.	52
Figure 4.3:	Schematics configuration of (a) grating-based passive PC; (b) fluorescence-dye-based active PC; (c) electroluminescence-material-based active PC.	54
Figure 4.4:	Schematic configurations of the device in (a) top view and (b) cross-sectional view. (c) Photo of the OLED taken from the ITO side with 6 V DC voltage applied between the electrodes. (d) Electric luminescence spectrum of the OLED at 20 mA/cm ²	56
Figure 4.5:	(a) Image obtained by OLED-based PDF microscopy, (b) magnified image of chosen area in (a), (c) interpolation of (b), and (d) noise reduction and deconvolution of (c). The objects are self-assembled polystyrene beads (diameter $\sim 2 \mu\text{m}$).	57
Figure 4.6:	(a) Intensity transmission spectrum of p-polarized light for OLED /Al/NPB-Air structure. (b) E field intensity distribution of SP mode 1 and (c) E field intensity distribution of SP mode 2 supported by OLED/Al/NPB-Air structure.	58
Figure 4.7:	(a) Power dissipation spectrum for 40 nm dipole/Al separation. (b) The energy coupling efficiency to SP mode 2 (η_1) for 30 nm and 60 nm Al film. (c) The final energy coupling efficiency to the field of mode 2 in air for 40 nm dipole/Al separation	60
Figure 4.8:	(a) The energy coupling efficiency to the propagating light for mode 1 excitation (η_0) and (b) that to SP mode 1 (η_1) as a function of dipole/Al separation for 30nm and 60nm Al film. (c) The final energy coupling efficiency	61
Figure 4.9:	(a) Energy coupled to the field at NPB/air interface, and (b) total E field intensity profile (log scale) with contribution from both SP modes supported by 30 nm Al (red [upper	61
Figure 4.10:	Comparison of the intensity decay length for conventional TIRF microscopy and PEF microscopy.	64
Figure 4.11:	(a) Cross section view; (b) RCWA characterization; (c) Comsol characteriztion of the designed substrate.	65
Figure 4.12:	Schematics of substrate fabrication. (a) Pattern generation through electron beam lithography; (b) pattern transfer through reactive ion etching; (c) Ag grating deposition and residue resist removal; (d) multilayer deposition.	66
Figure 5.1:	Schematics of the optical train of a phase contrast microscope .	70
Figure 5.2:	Schematic configuration of the LSPAC microscopy system . . .	72

Figure 5.3:	(a) SEM image, (b) AFM image, (c) dark field image and (d) the normalized scattering spectra of the deposited porous Ag film.	74
Figure 5.4:	(a) The scattering image of the LSPAC sample; (b) The cross section comparison of (a, c-d); (c) The phase contrast image and (d) the reflection dark field image of the control sample.	76
Figure 5.5:	(a) Schematics of the Al_2O_3 taper deposited on the porous Ag substrate; (b) the bright field and dark field image of the control sample. (c) The LSPAC image, (d) its cross section (blue line), and AFM measurement (green line) of the Al_2O_3 taper.	77
Figure 5.6:	(a) The LSPAC image of the lipid deposited on a porous Ag substrate. (b) The bright field image and (c) the dark field image of the control sample with lipid deposited on a cover slip.	78
Figure 6.1:	Schematics of a localized SP substrate. The blue region represents a transparent SiO_2 substrate. The hexagonal array of the gray circles corresponds to metallic nano-disks embedded into the SiO_2 substrate.	82
Figure 6.2:	The fluorescence image of actin filaments of HeLa cells grown on a SiO_2 protected Ag plasmonic substrate, with (a) LED and (b) SPI as the excitation source, respectively.	82

ACKNOWLEDGEMENTS

First, I want to thank my advisor, professor Zhaowei Liu for his continuous support. Professor Liu not only introduced me to the fields of optical microscopy and plasmonics, but also guided me throughout my research. His research philosophy and unique perspective on technical issues influenced me a lot.

I would also like to thank my committee members, professor Yu-Hwa Lo, professor Oleg Shpyrko, professor Sunil K. Sinha, and professor Douglas E. Smith. I am grateful that they shared their knowledge and experiences with me and kept me on the right track during the pursuit of my Ph. D. degree.

Besides my advisor and committee members, I also want to thank my lab-mates and friends. I am thankful for their assistance on projects, spending time hanging out with me, sharing their happiness with me, supporting me, and cheering me up when things seemed grim. I learned a lot from them too, both in research and in life. Time spent with them was both colorful and memorable during my five years in San Diego.

Finally, I want to dedicate this thesis to my father, mother, sister, my husband, and my extended family. Thank you for your unconditional love and support. You guys are always by my side, in good times and bad times. I would not have finished my Ph. D. without you.

Chapter 1, in part, is a reprint of the material as it appears in Nano Letters, 2010, 10, 2531-2536. Feifei Wei, Zhaowei Liu, “Plasmonic Structured Illumination Microscopy”. The dissertation author was the first author of this paper.

Chapter 2, in part, is a reprint of the material as it appears in Nano Letters 2010, 10, 2531-2536. Feifei Wei, Zhaowei Liu, “Plasmonic Structured Illumination Microscopy”. The dissertation author was the first author of this paper.

Chapter 3, in part, has been submitted for publication of the material as it may appear in Nature Photonics, 2014. Feifei Wei, Dylan Lu, Hao Shen, Weiwei Wan, Joseph Ponsetto, Eric Huang, Zhaowei Liu, “Experimental Demonstration of Wide Field Plasmonic Structured Illumination Microscopy”. The dissertation author was the first author of this paper.

Chapter 4, in part, is a reprint of the material as it appears in Optics

Letters, 2012, vol 37, no 21, 4359-4361. Feifei Wei, Yi Wan O, Guixin Li, Kok Wai Cheah and Zhaowei Liu, “Organic light-emitting-diode-based plasmonic dark-field microscopy”. The dissertation author was the first author of this paper.

Chapter 5, in part, is currently being prepared for submission for publication. The dissertation author was the first author of this paper.

VITA

2007	B. S. in Physics, University of Science and Technology of China
2007-2008	Graduate Teaching Assistant, University of Minnesota, Twin Cities
2009-2010	Graduate Teaching Assistant, University of California, San Diego
2014	Ph. D. in Physics, University of California, San Diego

PUBLICATIONS

Feifei Wei, Zhaowei Liu, “Plasmonic structured illumination microscopy for super-resolution imaging”, *Pan Standord*, Book Chapter in preparation.

Feifei Wei, Dylan Lu, Ryan Aguinaldo, Zhaowei Liu, “Localized surface plasmon assisted high contrast microscopy”, Paper in preparation.

Feifei Wei, Dylan Lu, Hao Shen, Weiwei Wan, Joseph Ponsetto, Eric Huang, Zhaowei Liu, “Experimental Demonstration of Wide Field Plasmonic Structured Illumination Microscopy”, Paper submitted.

Joseph Ponsetto, **Feifei Wei**, Zhaowei Liu, “Localized Plasmon Assisted Structured Illumination Microscopy for Wide-Field High-Speed Dispersion-Independent Super Resolution Imaging”, Paper submitted.

Yuchun Zhou, Samia Nawar Rahman, Yu-Hsin Liu, Dylan Lu, **Feifei Wei**, Yi-Che Chen, David Hall, Zhaowei Liu, Yu-Hwa Lo, “Optically excited cascaded exciton ionization in co-doped core-shell silicon nanowires”, Paper submitted.

Feifei Wei, Yin Wan O, Guixin Li, Kok Wai Cheah, Zhaowei Liu, “Organic Light Emitting Diode Based Plasmonic Dark Field Microscopy”, *Optics Letters*, 2012, 37, 21, 4359-4361.

Feifei Wei, Zhaowei Liu, “Plasmonic Structured Illumination Microscopy”, *Nano Letters*, 2010, 10, 2531-2536.

Feifei Wei, Yin Wan O, Guixin Li, Kok Wai Cheah, Zhaowei Liu, “Fluorescent Dye and OLED Based Plasmonic Dark Field Microscopy”, *Frontiers in Optics (FiO) proceedings*, San Jose, California, October 16-20, 2011, Page FWL5.

Feifei Wei, Zhaowei Liu, “Plasmonic imaging beyond the diffraction limit”, *LEOS Annual Meeting proceedings*, 2009, 355-356.

ABSTRACT OF THE DISSERTATION

Surface Plasmon Assisted High Resolution and High Contrast Optical Imaging

by

Feifei Wei

Doctor of Philosophy in Physics

University of California, San Diego, 2014

Professor Zhaowei Liu, Chair
Professor Oleg Shpyrko, Co-Chair

This thesis presents theoretical and/or experimental demonstrations of several Surface Plasmon (SP) assisted high-resolution or high-contrast microscopy techniques, including Plasmonic Structured Illumination Microscopy (PSIM), Plasmonic Darkfield (PDF) Microscopy, Plasmonic Evanescent field (PEF) Microscopy and Localized Surface Plasmon Assisted Contrast (LSPAC) Microscopy.

The PSIM combines tunable SP interference with structured illumination microscopy (SIM) to achieve super-resolution. By replacing the laser interference fringes in conventional SIM with SP interference (SPI) patterns, PSIM possesses higher image resolving power compared to that of SIM. Both theoretical and ex-

perimental concept demonstration shows more than 2.6-fold resolution improvement compared with conventional epi-fluorescence microscopy, whereas SIM only achieves about 2 times resolution improvement. This new PSIM technique is a wide field super-resolution imaging technique and potentially could be used for high-speed biomedical imaging.

The PDF microscopy is a compact, alignment-free dark-field microscopy technique. Experimental results show that it is capable of forming dark-field images of the specimens by utilizing a highly integrated chip-scale plasmonic condenser. The PEF microscopy is a similar technique that exploits the extremely short z decay length of high wave vector SP waves for achieving selective excitation of fluorophores very close to the substrate. Both the PDF and PEF microscopy possess high z resolution and high imaging contrast and are suitable for the dynamics study near the contact regions of living cells and the substrate.

The LSPAC microscopy combines localized surface plasmon resonance (LSPR) and dark field microscopy technique for high-contrast purpose. Because of the sensitive response of LSPR with the change of surrounding media refractive indices, this technique can convert the refractive index variation to the scattering intensity difference and form a high contrast, diffraction limited image of a thin unstained transparent specimen with small refractive index variation.

Chapter 1

Introduction

1.1 Background of imaging system and diffraction limit

Since its introduction around the 1600s, optical microscopy has made big strides in improvements owing to the invention of achromatic lens system, Köhler illumination configuration, as well as the development in lens manufacturing processes. Currently, the optical microscope is an indispensable tool for biological research due to its non-invasive probing ability to examine bio-specimens.

1.1.1 Coherent and incoherent imaging system

Depending on whether the light coming from the sample is spatially coherent or not, imaging systems could be separated to coherent imaging system and incoherent imaging system. A coherent imaging system, such as the transmission or reflection microscopy with a coherent illumination light source, is a linear system with respect to the electric field. The electric field in the image plane $E_i(x, y)$ can be written as a convolution of the electric field in the object plane $E_o(x, y)$ and the electric field impulse response function of the system $h(x, y)$. By taking the square of electric field amplitude, the intensity detected at the image plane $I_i(x, y)$ can be calculated. The Fourier transform of Equation (1.1) reveals that the spectrum of the electric field in the image plane $F_{E_i}(f_x, f_y)$ equals to the spectrum of the

electric field in the object plane $F_{E_o}(f_x, f_y)$ times the amplitude transfer function of the system $H(f_x, f_y)$, as shown in Equation (1.2). Since the amplitude transfer function can be written as a scaled pupil function of the system, it could be interpreted as a band pass filter with certain passing band for diffraction-limited imaging systems, whose pupil functions are 1 within certain region and 0 outside [1].

$$\begin{aligned} E_i(x, y) &= E_o(x, y) * h(x, y) \\ &= \int_{-\infty}^{+\infty} \int_{-\infty}^{+\infty} E_o(x_o, y_o) h(x - x_o, y - y_o) dx_o dy_o \end{aligned} \quad (1.1)$$

$$F_{E_i}(f_x, f_y) = F_{E_o}(f_x, f_y) \cdot H(f_x, f_y) \quad (1.2)$$

$$I_i(x, y) = |E_i(x, y)|^2 = |E_o(x, y) * h(x, y)|^2 \quad (1.3)$$

In regard to incoherent image systems such as fluorescence microscopy, since the phase variation of different points in the object plane is uncorrelated, it is a linear system with respect to the intensity. The intensity at the image plane $I_i(x, y)$ is a convolution of the intensity at the object plane $I_o(x, y)$ and the point-spread-function of the system $psf(x, y)$. By taking the Fourier transform of Equation (1.4), the spectrum of the image intensity $F_{I_i}(f_x, f_y)$ can be written as the spectrum of the object intensity $F_{I_o}(f_x, f_y)$ times the optical transfer function of the imaging system $OTF(f_x, f_y)$. The optical transfer function of the imaging system is the Fourier transform of the intensity impulse response function $|h(x, y)|^2$, and can be further expressed as the normalized autocorrelation function of the amplitude transfer function [1]. Therefore, the optical transfer function of a diffraction-limited imaging system is also a band pass filter. The highest spatial frequency detected in the image plane is determined by the cutoff frequency of the OTF of the diffraction-limited imaging system and spatial frequency information higher than that in the object plane could not go through the system.

$$I_i(x, y) = I_o(x, y) * psf(x, y) = I_o(x, y) * |h(x, y)|^2 \quad (1.4)$$

$$F_{I_i}(f_x, f_y) = F_{I_o}(f_x, f_y) \cdot OTF(f_x, f_y) \quad (1.5)$$

1.1.2 Diffraction limit

Due to the band-passing nature of conventional imaging systems, either coherent or incoherent, the finest feature in the image plane is limited by diffraction. Even today, after more than four hundred years of improvements, diffraction limit is still a barrier for most optical microscopes.

The resolution limit of a microscope system characterizes the ability of an optical system to resolve close by point objects as separate points from one another. There are several criteria to define the lateral resolution limit of an optical system. Rayleigh criterion defines two points source to be just resolved as the maximum of the diffraction pattern of one point source coincide with the first minimum of the diffraction pattern of the other [2]. Since the diffraction-limited image of a point source formed by lenses with circular apertures is an Airy disk, Rayleigh criterion for these system equals $0.61\lambda/NA$, the distance between the center maximum and first minimum of an Airy disk, with λ being the wavelength of the light and NA being the numerical aperture of the lens systems. Besides the Rayleigh criterion, Abbe limit, which defines the resolution limit of an imaging system as $\lambda/(2NA)$, is another criterion widely used in microscopy field. The image of two point sources with separation equals Abbe limit still has a small dip in the middle, although not as distinct as that with separation equals Rayleigh criterion. A third criterion of resolution limit is the Sparrow limit, which is widely used in Astronomy. The Sparrow limit is defined as that the image of two point sources no longer has a dip in the middle and equals to $0.47\lambda/NA$ for lens system with circular apertures. Although there are small coefficient differences among Rayleigh criteria, Abbe limit and Sparrow limit, they are all proportional to the wavelength length of the light used and inversely proportional to the numerical aperture of the lens system.

1.2 Review of advanced microscopy techniques

As more and more biological studies require sub-100 nm or even molecular scale resolution, improving the lateral resolution of optical microscopes to such scales has become a hotly researched field.

1.2.1 Traditional methods of improving the resolving power

Since the diffraction limit is proportional to the wavelength of the light, decreasing the detection wavelength to ultraviolet spectrum, X-ray spectrum or even electron beam will significantly increase the resolving power (decrease the resolution limit). However, these high-energy probes would result in significant damage to bio-samples and could not be used for living specimen measurements. Another straightforward way of improving the resolving ability of optical microscopy is to increase the NA of the objective. By using immersion liquid such as oil, the NA of the objective can reach up to 1.4. However, the NA of these immersion objectives is then restricted by the refractive index of the immersion media. Since there are only several choices of high-refractive index liquids as immersion media, the improvement of the optical microscope resolving power is limited.

Besides decreasing the wavelength and increasing the NA of the imaging system, exploiting the high spatial frequency information carried by the evanescent waves emerging from the object is another way of improving the resolving power of an imaging system. Since the intensity of an evanescent wave decreases exponentially with the distance from the object, placing a probe at the near field zone of the object is necessary. Near-field scanning microscopy (NSOM), invented around 1980s, utilizes a sub-wavelength scale tip or aperture within the near field zone of the object to detect the evanescent waves. With the help of scanning stages and feedback mechanisms to keep the probe within the near field zone, images with sub-diffraction limited resolution can be formed. The resolution of NSOM systems is limited by the size of the tip or aperture, and image resolution smaller than one tens of the wavelength has been demonstrated [3]. Although NSOM has significantly improved resolution when compared to conventional optical microscopy, placing the probe within several tens of nanometer of the object is still quite challenging for certain applications such as studies involving living cells or intracellular cellular structure.

1.2.2 Super-resolution fluorescence microscopy techniques

Within the past two decades, multiple super-resolution fluorescence microscope techniques, such as stimulated emission depletion microscopy (STED) [4, 5, 6, 7] single molecular localization techniques [8, 9, 10, 11, 12, 13], structured illumination microscopy (SIM) [14, 15, 16], have been proposed and experimentally demonstrated. These techniques can resolve fluorescent features around tens of nanometers or less by switching the fluorescent molecules on and off sequentially.

STED microscopy achieves super-resolution resolution by confining the excitation of fluorescence molecules to a sub-diffraction limited region through stimulated emission depletion process. In order to form a 2D super-resolution image, two co-axially aligned synchronized illuminations sources consisting of an excitation beam and a STED beam are used to scan the sample. Due to the stimulated emission depletion effect, only fluorescent molecules within the overlap region of the excitation beam and the dark area of the STED beam could fluoresce. The resolving power of the STED microscopy is determined by the power of the depletion laser, but the extreme high power may result in rapid photobleaching of the sample [4, 5]. Researchers have used STED microscopy to resolve individual vesicles (~ 40 nm in diameter) in the synapse and reveals the behavior of the synaptotagmin I in mildly active or intensely stimulated nerve terminals [6]. In 2008, Stefan W. Hell's group also demonstrated 28 frames per second (fps) video-rate STED microscopy of synaptic vesicles in living cells with 62 nm resolution and 1.8 μm by 1.8 μm field of view using a resonant Galvo scanning mirror [7]. However, since STED is a scanning technique, the time needed for one frame scales linearly to the imaging area. Different from STED microscopy, stochastic optical reconstruction microscopy (STORM) and photoactivated localization microscopy (PALM) overcome the diffraction-limit by high-accuracy localization of photoswitchable fluorophores [8, 9, 10, 11, 12, 13]. In each imaging cycle of PALM and STORM microscopy, only a sparse set of the fluorescent molecules, with center-to-center distance larger than conventional diffraction limit, are turned on. Therefore, the image of these fluorescent molecules has little overlaps and the location of each fluorophore can be determined to nanometer accuracy through fitting its corresponding image with

a Gaussian function. By combining the processed images from multiple imaging cycles, a super-resolution image of the fluorophore distribution could be reconstructed. For PALM and STORM, the resolution is determined by the localization accuracy, which is eventually limited by the number of photons captured from the fluorophore within one imaging cycle [8, 9, 10, 11, 12, 13]. Later, three-dimensional (3D) STORM was developed to achieve 3D resolution improvement with 20-30 nm lateral-resolution and 50-60 nm axial-resolution through using optical astigmatism introduced by a cylindrical lens [9, 10]. Recently, high speed STORM was demonstrated with microtubule dynamics in living cells at 3 seconds time resolution and $2.6 \mu\text{m}$ by $2.6 \mu\text{m}$ field of view [11]. With the help of compressive sensing, the updated particle location extraction algorithm can successfully recover the fluorophore distributions with fluorophore density up to one order of magnitude higher than that could be handle by conventional STORM data process algorithm. Despite the significant speed improvement, the number of raw measurements needed for reconstructing a super-resolution image is still on the order of 100 for $2.6 \mu\text{m}$ by $2.6 \mu\text{m}$ field of view even with the most up to date algorithm, which also increases as the imaging area increases [11].

1.2.3 Structured Illumination Microscopy SIM

Among the high-resolution imaging techniques, SIM is a method of special interest. It is suitable for *in vivo* biological imaging applications because it utilizes visible light (low energy photon) for imaging and it is a wide field super-resolution technique, which can potentially achieve high-imaging speed. SIM with a resolution of about twice the diffraction limit has already been experimentally demonstrated and used to acquire 3D multicolor high-resolution images of the nucleus of mammalian cells [14, 15, 16]. With the help of liquid crystal spatial light modulator and ferroelectric liquid crystal phase retarders, the speed of PSIM was then improved to 4-11 fps with 32×32 to $8 \times 8 \mu\text{m}$ [17]. Since SIM is a wide field imaging technique, the time it takes to acquire one super-resolution image is less than that of STED, STORM and PALM with the same imaging area.

In conventional epi-fluorescence microscopy, only information with spatial

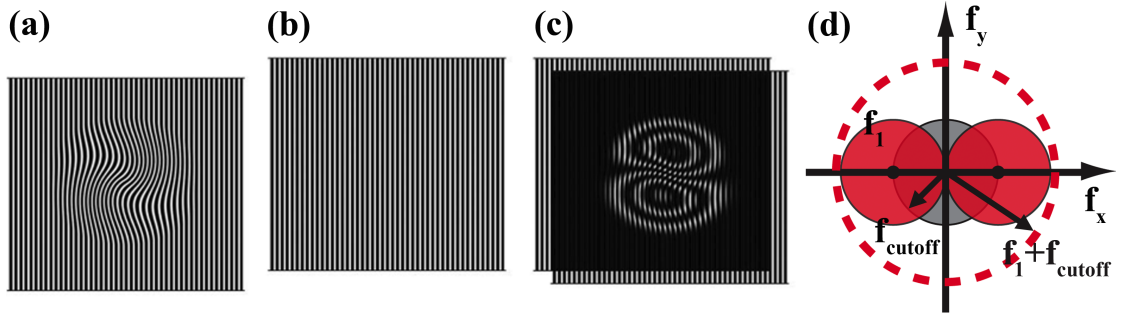


Figure 1.1: Concept of resolution enhancement in SIM. (a) An example object with small features; (b) a structured illumination pattern; (c) Moiré fringes formed by superposing structured illumination pattern (b) with object (a); (d) Fourier space representation of the SIM. The gray circle with radius f_{cutoff} corresponds to the accessible area of epi-fluorescence microscopes; the two red solid circles represent the high-spatial frequency information that can be coupled into the detectable region through structured illumination shown in (b). The shift in Fourier space is determined by the spatial frequency of the illumination pattern f_1 .

frequencies that reside within the passband of the optical transfer function (OTF) of the objective can be detected. The OTF corresponds to a circular region of radius f_{cutoff} around the origin in Fourier space (the gray circle in Figure 1.1 d), where f_{cutoff} defines the maximum resolvable spatial frequency, which is equal to $\lambda/(2NA)$ for conventional epi-fluorescence microscopes. SIM utilizes the so-called Moiré effect to couple some of the high spatial frequency information from outside of the detectable region to inside the region to improve the resolution. For example, when an object with spatial frequency f (Figure 1.1 a) overlaps with an illumination pattern with spatial frequency f_1 (Figure 1.1 b), a Moiré fringe that contains spatial frequency $f - f_1$, f and $f + f_1$ (Figure 1.1 c) is generated. If the spatial frequency of the Moiré fringe is smaller than f_{cutoff} , the Moiré fringe can be detected by an optical microscope. The observed Moiré fringe image contains the contribution from all three components in Fourier space (represented by the red circles and the gray circle in Figure 1.1 d) due to the spatial frequency mixing introduced by the structured illumination. In order to obtain a faithful high-resolution image, the three components in Fourier space need to be solved and moved back to their original positions. Therefore, multiple images with different illumination

phases should be recorded and used to reconstruct the final high-resolution image through a numerical algorithm [14, 15, 16]. The saturated structured illumination microscopy (SSIM), proposed by R. Heintzmann [18] and experimentally demonstrated by M. G. L. Gustafsson [19], can achieve even higher resolution compared to SIM by utilizing the nonlinear dependence of the fluorescence emission rate on the illumination intensity. The SSIM, however, has to cope with additional limitations such as fluorescence bleaching by strong illumination light intensity and slower imaging speed compared with SIM.

In SIM, $f_1 + f_{\text{cutoff}}$ defines the largest spatial frequency that can be coupled into the passband of the OTF. The resolution improvement, $(f_1 + f_{\text{cutoff}})/f_{\text{cutoff}}$, is limited by the ratio f_1/f_{cutoff} . If we use the same objective for illumination and detection, the spatial frequency shift $f_1 = 2NA/\lambda_{\text{excitation}}$ and the cutoff frequency $f_{\text{cutoff}} = 2NA/\lambda_{\text{emission}}$ are all determined by the NA of the objective. Considering excitation and emission are close for most cases, f_1 usually is close to f_{cutoff} . Therefore, the resolution for SIM is about $\lambda_{\text{emission}}/4NA$, roughly about twice resolution improvement compared with conventional epi-fluorescence microscopy [15, 16].

1.3 Background of surface plasmon (SP)

Surface plasmons (SPs), also known as surface plasmon polaritons (SPPs), are electromagnetic excitations propagating at the metal/dielectric interface, formed by the collective oscillation of the electrons at a metal boundary [20]. These electromagnetic waves are evanescently confined along the direction perpendicular to the interface. The fundamental properties of SPs have been extensively studied since the 1970s and widely applied thereafter in many fields [21, 22, 23, 24, 25].

The dispersion relation of SPs can be derived based on the Maxwell's equations and the boundary conditions at the interface. The SPs wave vector for semi-infinite metal/dielectric interface can be written as Equation (1.6) and Equation (1.7), with k_0 representing the wave vector of the free space light and ϵ_1, ϵ_2 representing the dielectric constants of metal and the dielectric respectively. The typical dispersion curve for SPs described by Equation (1.6) is represented by the

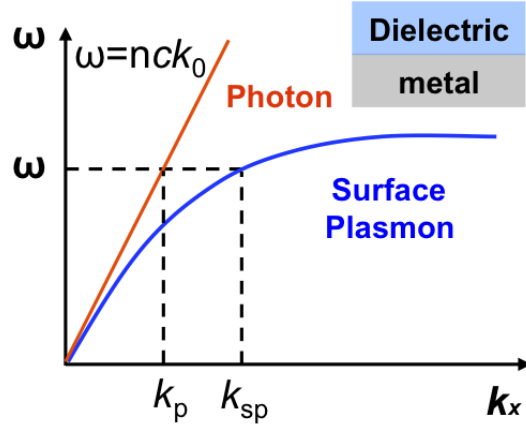


Figure 1.2: Schematic of the dispersion curves of the photon (red line) in the dielectric and surface plasmon (blue line).

blue line in Figure 1.2. Since the dispersion curves of SPs always lie on the right side to that of the photon (red line in Figure 1.2), k_{sp} is always larger than the corresponding k_{photon} . The ratio k_{sp}/k_{photon} can be tuned by adjusting the frequency of the excitation light, the refractive index of the surrounding dielectric, or the thickness of the metal film [26, 27, 28]. For instance, as the frequency of the excitation light approaches the SPs resonant frequency, k_{sp}/k_{photon} becomes extremely large. For excitation light with a specific frequency, the ratio increases if the refractive index of the dielectric is increased. If both excitation light and surrounding media are fixed, the SP modes can also be adjusted by changing the thickness of the metal film.

$$k_{sp} = k_0 \sqrt{\frac{\epsilon_1 \epsilon_2}{\epsilon_1 + \epsilon_2}} \quad (1.6)$$

$$k_{zi} = \sqrt{\epsilon_i k_0^2 - k_x^2}, i = 1, 2 \quad (1.7)$$

Since the wave vector of the photon and the SP is different, this momentum mismatch should be compensated by coupling structures in order to excite SPs with light. Figure 1.3 shows several examples of the coupling structures. In a prism coupling structure, the momentum of the SP is provided by the momentum of the photon inside the prism, which means that the refractive index of the prism should be larger than the relative SP wave vector (in unit k_0) supported at the top surface of the plasmonic material. At the resonance angle, at which the in-plane component

of the photon wave vector matches with the SP wave vector, the intensity of the reflected light is significantly reduced and part of the energy is coupled to the SP at the top surface of the plasmonic material. In a grating coupling structure, the momentum mismatch between an incident photon and the SP is provided by the diffraction from the grating structure. When the summation of the momentum provided by the grating structure and the in-plane momentum of the illumination photon equals that of the SP, SPs could be effectively excited on the top surface of the plasmonic material. Besides utilizing periodic grating structure, a single defect can also provide this momentum mismatch through scattering, as shown in Figure 1.3 c, although the percentage energy scattered to the waves with appropriate wave vector for the SP excitation is lower compared with grating case. Moreover, the SP can also be excited through near field coupling between the active media and the plasmonic material, as shown in Figure 1.3 d. The evanescent field emerging from the active media can be used to provide the SP wave vector and excite the SP at the top surface of the plasmonic material. Due to the exponentially decay of the evanescent field, the plasmonic material should be placed within the near field region of the active media for effective coupling. The active media could be any kind of luminescent material, such as photo luminescent or electrical luminescent material etc.

Due to their large wave vector, SPs are especially suitable for nanophotonics sub-wavelength scale applications. Recently, because of the significant advancement in nanoscale fabrication techniques, various fascinating applications of SPs have been experimentally demonstrated, including sub-diffraction limited imaging [29, 30, 31, 32, 33, 34], sub-diffraction limited focusing or lithography [26, 27, 28, 35], sub-wavelength waveguide [36, 37], and optical negative refraction [38]. In the area of super-resolution imaging, various techniques have been proposed or experimentally demonstrated to achieve sub-diffraction limited resolution, such as far field superlens (FSL) [29, 30, 31], hyperlens [32, 33, 34], metalens [39, 40, 41] , SP assisted super-resolution microscopy [42, 43, 44, 45, 46] etc. For example, the far-field superlens, placed at the near field of the object, enhances the scatter evanescent waves with a slab of superlens and converts the enhanced

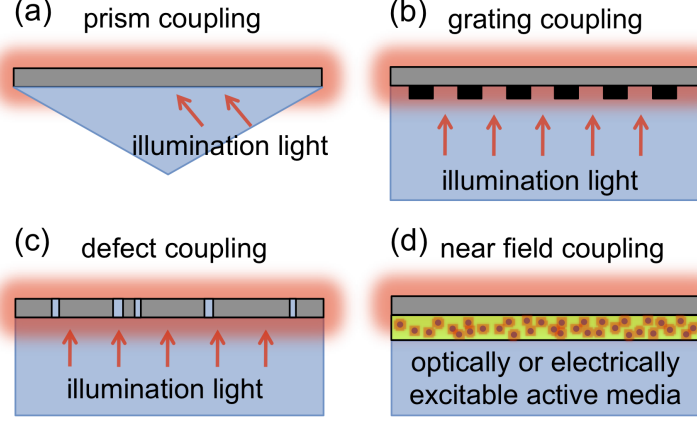


Figure 1.3: Cross-section view of various SP coupling structures. (a) A prism coupling structure; (b) a grating coupling structure; (c) a defect coupling structure; (d) a near field coupling structure. The gray areas corresponds to the plasmonic material.

field to propagating light with periodic corrugations [29, 30, 31]. The propagating light is detected in the far field and used to reconstruct the super-resolution image through a numerical process [29, 30, 31]. Similar to the case for the far field superlens, the object of a hyperlens should also be placed at its near field. However, instead of coupling the evanescent waves to propagating light with gratings, the hyperlens supports the propagation of the evanescent waves along the radial direction of a layered hyperbolic metamaterial and compresses its tangential wave vectors as the waves travel outward due to the conservation of angular momentum. As a result, a magnified image that with features larger than the diffraction limit will form at the out boundary of the hyperlens and could be detected by a conventional microscope [32, 33, 34].

1.4 This thesis

In this thesis, we will theoretically and/or experimentally demonstrate several Surface Plasmon (SP) assisted high-resolution and high-contrast microscopy techniques, including Plasmonic Structured Illumination Microscopy (PSIM), Plasmonic Dark Field (PDF) Microscopy, Plasmonic Evanescent Field (PEF) mi-

croscopy and Localized Surface Plasmon Assisted Contrast (LSPAC) Microscopy.

Earlier in Chapter 1, we briefly introduced the coherent and incoherent imaging system, as well as the diffraction limit, and then reviews multiple advanced microscopy techniques. The background about SP and localized SP is presented in the end of the chapter.

Chapters 2 and 3 focus on the theoretical and experimental demonstration of the PSIM, respectively. Chapter 2 explains the physical principles of this technique and numerically verifies the super-resolution imaging capability of PSIM with Comsol and Matlab simulation. Then, Chapter 3 describes our custom built PSIM system and then presented the super-resolution image of 100 nm fluorescence beads reconstructed from six diffraction limited images and discusses the advantages of this technique.

Chapters 4 and 5 are about SP assisted high-contrast technique. The first part of Chapter 4 shows the principles as well as the experimental demonstration of the PDF technique, which utilizes the evanescent field nature of SP for dark field imaging purpose. The second part of this chapter discusses the principle of a highly related technique, PEF microscopy, and numerically confirms the super-z resolution capability of metalmaterials. Finally, the principles of LSPAC microscopy and its experimental concept demonstration are presented in Chapter 5, with porous silver (Ag) film serving as the plasmonic substrate.

In the end, Chapter 6 presents several future directions of the four techniques discussed before and summarizes this thesis.

Chapter 1, in part, is a reprint of the material as it appears in Nano Letters 2010, 10, 2531-2536. Feifei Wei, Zhaowei Liu, “Plasmonic Structured Illumination Microscopy”. The dissertation author was the first author of this paper.

Chapter 2

Theory of plasmonic structured illumination microscopy (PSIM)

2.1 Principles of PSIM

As discussed in Chapters 1, the resolution of SIM is roughly twice of the epi-fluorescence microscopy resolution. As shown in Figure 2.1 a, the resolution improvement of SIM is mainly limited by the spatial frequency of the illumination patterns, which also couldn't not exceed f_{cutoff} in the free space laser interference case [15, 16]. To achieve a higher resolution improvement using the same SIM principles, one straightforward way is to increase the spatial frequency of the illumination patterns. Techniques utilizing high refractive index dielectric, such as using a cover slip or using Si to form the evanescent field interference with spatial frequency higher than the f_{cutoff} of the objective have been proposed and demonstrated either numerically or experimentally [47, 48, 49].

Besides light or evanescent field at the dielectric interface, surface plasmon (SP) is another good candidate to form sub-wavelength scale interference features [26, 27, 28] due to their larger wave vector compared to light at the same frequency. In addition, the SP wave vector is mainly determined by the permittivity of the plasmonic material and the surrounding media, instead of the NA of the objective. Because of its large wave vector, SP is widely used in nanophotonics sub-wavelength

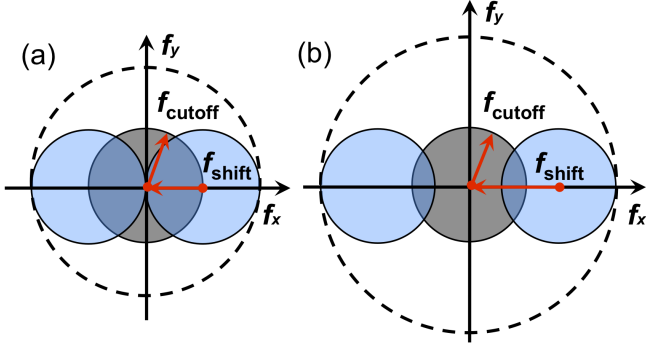


Figure 2.1: Illustration of the SIM and PSIM principles. (a) SIM and (b) PSIM resolution improvement representation in Fourier space. The gray circles in (a) and (b) correspond to the spatial information within the pass band of conventional microscopy. The blue circles in (a) and (b) correspond to the side-band high spatial frequency information components accessible by SIM and PSIM, respectively. The dashed circles represent the Fourier space region detectable by SIM and PSIM respectively.

scale research [26, 27, 28, 50, 51, 42, 43, 44, 45, 46, 52, 53]. Specifically in the imaging field, several SP assisted super-resolution imaging techniques have been explored either theoretically or experimental [42, 43, 44, 45, 46]. In Chapter 2 and Chapter 3, we will present the numerical and experimental concept demonstration of an alternative approach, termed as PSIM. In PSIM, the SPI pattern with period smaller than $\lambda/(2NA)$ replaces the laser interference illumination to achieve higher wide field resolving power compared with conventional SIM, as shown in Figure 2.1.

In the proposed PSIM technique, edges or slits are used to excite SPs because they could couple broadband light into SPs due to their broadband Fourier spectrum. When the patterned plasmonic structure is illuminated by a laser beam, the SPI pattern with period equal to $\lambda_{sp}/2$ is formed by the interference of the counter propagating SP waves generated at the adjacent slits or edges [26, 27, 28]. To proceed with the super-resolution image reconstruction, the illumination fringes should be laterally translated multiple times during the image acquisition process [15, 16, 18, 19]. For SPI case, the lateral shift of the interference pattern is realized by adjusting the phase difference between the counter-propagating SP, which can

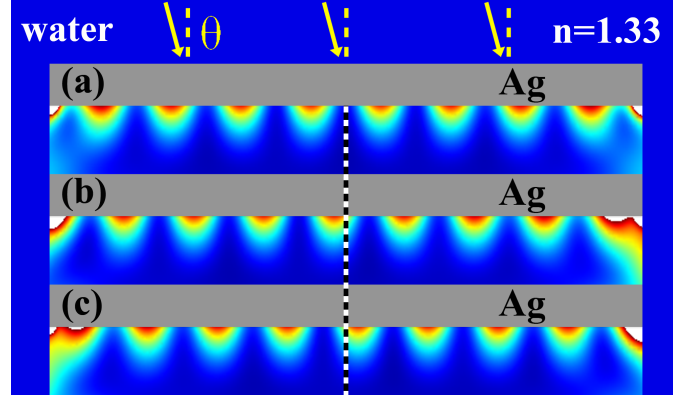


Figure 2.2: Numerical demonstration of the lateral shift of the SP interference pattern formed by the 563 nm excitation light with different incident angles. The simulation structure consists of a 1700 nm wide and 100 nm thick silver (Ag, gray area) stripe surrounded by water (blue area, $n=1.33$). (a-c) The time-averaged electrical energy density distribution of the SP interference pattern with incident angle equal to 0° , 4.6° , and 8.0° , respectively. The three interference patterns show 120° mutual phase difference along the lateral direction.

be achieved by changing the incident angle θ of the illumination laser [50]. Under different incident angles, the light incident on the two adjacent edges or slits possesses a phase difference $\phi(\theta)$; this difference causes the relative phase difference between the excited SPs and thus changing the phase of the interference patterns. The simulation results in Figure 2.2 clearly show that the SP interference pattern shifts laterally with various incident angles.

2.2 PSIM image reconstruction algorithm

In the proposed PSIM technique, we focus on the super-resolution fluorescence microscopy. Since the light emitted from fluorescent molecules are spatially incoherent, the whole system should be considered as an incoherent system. As discussed in §1.1.1, the image formation of an incoherent imaging system under 1D interference fringe illumination $illum(x, y) = 1 + \cos(2\pi f_0 x + \phi)$ can be formulated as Equation (2.1) below, with $f_0, \phi, I_{i,illum}(x, y), I_o(x, y)$ and $psf(x, y)$ represent the spatial frequency and the phase of the interference fringe, the intensity at the image plane (Figure 2.3 e), the intensity at the object plane (Figure 2.3

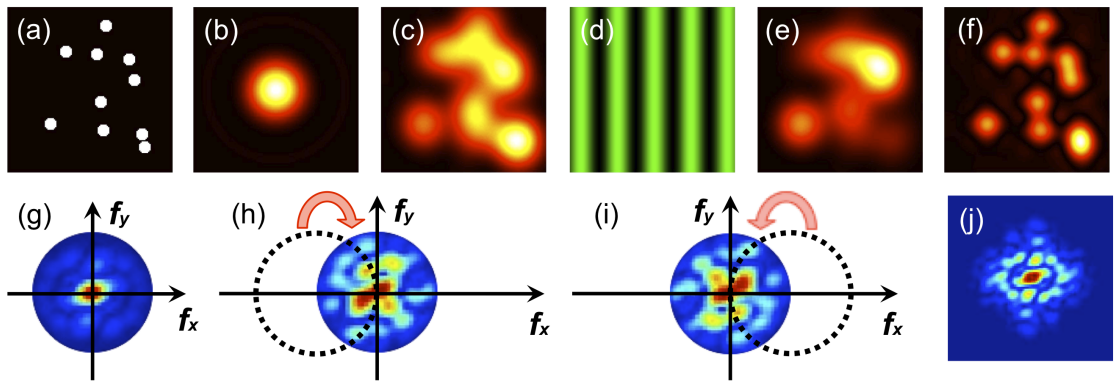


Figure 2.3: Image space and Fourier space representation of SIM. (a) Object, consisting of randomly distributed fluorescent beads; (b) point spread function of the microscope system; (c) conventional diffraction limited fluorescence image; (d) structured illumination along horizontal direction; (e) fluorescence image under (d) illumination pattern; (f) reconstructed 2D super-resolution image; (g) Fourier transform of (c), corresponding to the Fourier space diffraction limited information $F_{I_o}(f_x, f_y) \cdot OTF$; (h-i) high spatial frequency information that are shifted to the passing band of the OTF of the imaging system due to the structured illumination, corresponding to $F_{I_o}(f_x + f_0, f_y) \cdot OTF$ and $F_{I_o}(f_x - f_0, f_y) \cdot OTF$, respectively; (j) extended Fourier space information acquired through structured illumination along both horizontal and vertical directions. (f) is the Fourier transform of (j).

a) and the point spread function of the system (Figure 2.3 b), respectively. The Fourier transform of Equation (2.1) is shown in Equation (2.2), with $F_{I_{i,illum}}(f_x, f_y)$, $F_{I_o}(f_x, f_y)$, $F_{illum}(f_x, f_y)$ and $OTF(f_x, f_y)$ correspond to the Fourier transform of $I_{i,illum}(x, y)$, $I_o(x, y)$, $illum(x, y)$ and $psf(x, y)$ accordingly. After plugging in $illum(x, y) = 1 + \cos(2\pi f_0 x + \phi)$, Equation (2.2) can be expanded to Equation (2.3), with $F_{I_o}(f_x, f_y) \cdot OTF$ (Figure 2.3 g), $F_{I_o}(f_x + f_0, f_y) \cdot OTF$ (Figure 2.3 h) and $F_{I_o}(f_x - f_0, f_y) \cdot OTF$ (Figure 2.3 i), representing the un-shifted accessible spectrum of the object and the shifted high spatial frequency information of the object. Therefore, by taking the diffraction-limited image under the interference fringe illumination with three different phases, both the un-shifted accessible spectrum of the object and shifted high spatial frequency information of the object could be solved, with Equation (2.4) and Equation (2.5) showing the matrix forms of this process. To achieve a 2D resolution improvement, this process should be performed for both horizontal and vertical directions. After shifting the high spatial frequency information components to their original location, assembling them together with the accessible spectrum of the object, and performing the inverse Fourier transform, a super-resolution image could be reconstructed, as shown in Equation (2.6) and Figure 2.3 f.

$$I_{i,illum}(x, y) = [I_o(x, y) \cdot illum(x, y)] * psf(x, y) \quad (2.1)$$

$$F_{I_{i,illum}}(f_x, f_y) = [F_{I_o}(f_x, f_y) * F_{illum}(f_x, f_y)] \cdot OTF(f_x, f_y) \quad (2.2)$$

$$\begin{aligned} F_{I_{i,illum}}(f_x, f_y) &= [F_{I_o}(f_x, f_y) \cdot OTF + \\ &\quad 0.5F_{I_o}(f_x + f_0, f_y)e^{-i\phi} \cdot OTF + 0.5F_{I_o}(f_x - f_0, f_y)e^{i\phi} \cdot OTF] \end{aligned} \quad (2.3)$$

$$\begin{aligned} \begin{pmatrix} F_{I_{i,illum1}}(f_x, f_y) \\ F_{I_{i,illum2}}(f_x, f_y) \\ F_{I_{i,illum3}}(f_x, f_y) \end{pmatrix} &= \begin{pmatrix} 1 & 0.5e^{-\phi_1} & 0.5e^{\phi_1} \\ 1 & 0.5e^{-\phi_2} & 0.5e^{\phi_2} \\ 1 & 0.5e^{-\phi_3} & 0.5e^{\phi_3} \end{pmatrix} \begin{pmatrix} F_{I_o}(f_x, f_y) \cdot OTF \\ F_{I_o}(f_x - f_0, f_y) \cdot OTF \\ F_{I_o}(f_x + f_0, f_y) \cdot OTF \end{pmatrix} \\ &= A \begin{pmatrix} F_{I_o}(f_x, f_y) \cdot OTF \\ F_{I_o}(f_x - f_0, f_y) \cdot OTF \\ F_{I_o}(f_x + f_0, f_y) \cdot OTF \end{pmatrix} \end{aligned} \quad (2.4)$$

$$\begin{pmatrix} F_{I_o}(f_x, f_y) \cdot OTF \\ F_{I_o}(f_x - f_0, f_y) \cdot OTF \\ F_{I_o}(f_x + f_0, f_y) \cdot OTF \end{pmatrix} = A^{-1} \begin{pmatrix} F_{I_{i,illum1}}(f_x, f_y) \\ F_{I_{i,illum2}}(f_x, f_y) \\ F_{I_{i,illum3}}(f_x, f_y) \end{pmatrix} \quad (2.5)$$

$$\begin{aligned} I_{\text{recon}} = & F^{-1}[F_{I_o}(f_x, f_y) \cdot OTF + \\ & F_{I_o}(f_x, f_y) \cdot OTF(f_x - f_0, f_y) + F_{I_o}(f_x, f_y) \cdot OTF(f_x + f_0, f_y) + \\ & F_{I_o}(f_x, f_y) \cdot OTF(f_x, f_y - f_0) + F_{I_o}(f_x, f_y) \cdot OTF(f_x, f_y + f_0)] \end{aligned} \quad (2.6)$$

2.3 Numerical demonstration of PSIM concept

In the following, we present two specific plasmonic designs, thick-metal-film/dielectric and thin-metal-film/dielectric structures, to serve as examples for PSIM demonstration and a guide for future development. The final reconstructed images are also provided to demonstrate the imaging performance of each design.

The structures of the two designs both consist of a layer of silver (Ag) film as the metal film and water as the surrounding dielectric. Ag is chosen as the supporting material because the SP frequency at the Ag/dielectric interface covers the entire visible spectrum with relatively little loss. Water is used as the surrounding dielectric because many biological samples are in an aqueous environment. In the SP interference simulation, the permittivity of Ag and Cr at different excitation frequencies was calculated by interpolating data from reference [54] and [55].

2.3.1 Thick plasmonic substrate and its imaging capability demonstration

Specifically, for the thick-metal-film/dielectric structure, the thickness of the Ag film was chosen to be 100 nm so that it is thick enough to be treated as a semi-infinite interface. Excitation light with wavelengths of 390 nm and 563 nm were used to excite SP interference patterns. We assumed the fluorescent objects (for example quantum dots) absorb light at these excitation wavelengths and emit light at 580 nm. The fluorescent signal is detected by an objective with

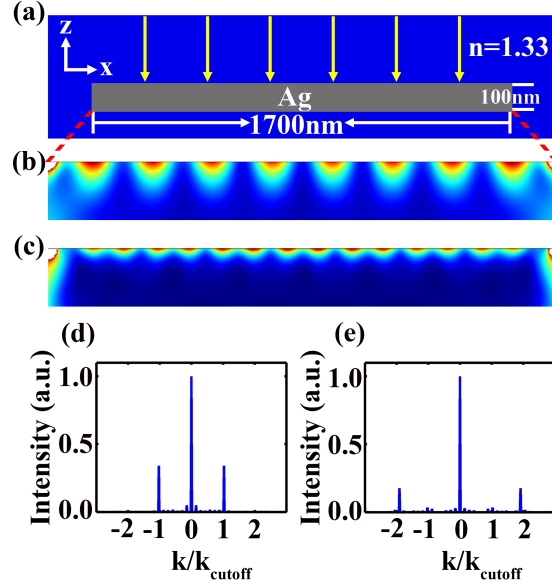


Figure 2.4: Numerical demonstrations of the SP interference at thick film-dielectric interface. (a) Structure configuration; (b,c) time-averaged electric energy density distribution excited by 563 and 390 nm light; (d,e) Fourier transform of (b,c) respectively.

NA=1.4. The distributions of the time-averaged electric energy density under the two illumination lights are shown in Figure 2.4 b and c. The Fourier transforms of the illumination patterns, measured 20 nm under the Ag film, reveal peaks around $1k_{\text{cutoff}}$ and $2k_{\text{cutoff}}$, which is consistent with the calculated value from the analytical equation ($2|\mathbf{k}_{sp1}|$ and $2|\mathbf{k}_{sp2}|$).

In the imaging performance simulations, SP interference patterns serve as the structured illumination patterns to illuminate a fluorescent object. For each orientation of illumination, a sequence of 3 images taken under illumination with different phases 0° , 90° and 180° were used to solve the 0^{th} , $\pm 1^{\text{st}}$ order components (gray and blue circles in Figure 2.1 b in Fourier space). The orientation of the illumination pattern is then rotated three times with steps of 45° in the x-y plane to cover more region in Fourier space, yielding a total of 12 intermediate images for each final high-resolution image. The numerical algorithm of reconstructing high-resolution image from intermediate images is the same as that of SIM [14, 15, 47, 16, 18, 19, 56]. In the simulation, a 4 nm quantum dot (emission

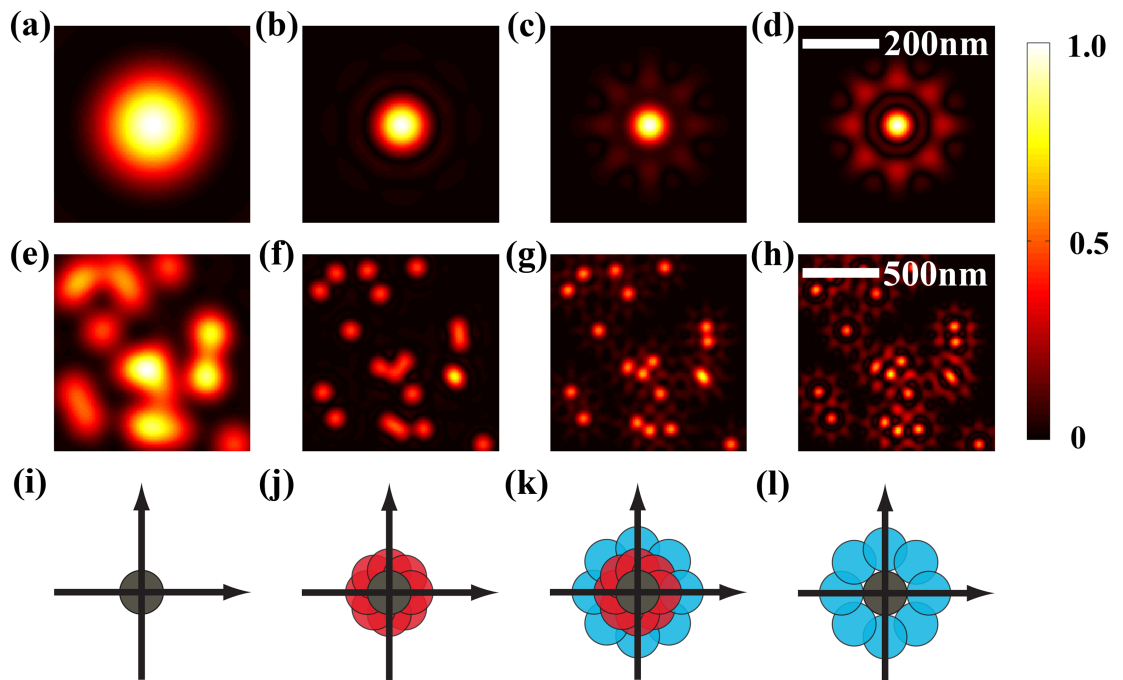


Figure 2.5: Point spread function of (a) conventional epi-fluorescence microscopy. (b) PSIM using 563 nm excitation light. (c) PSIM using both 563 and 390 nm excitation light. (d) PSIM using 390 nm excitation light. (e-h) Imaging performance demonstration for the case (a-d). Notice the scale bar difference between (a-d) and (e-h). (i-l) Corresponding k space representations. The gray circle represents the low spatial frequency information that can be acquired through the epi-fluorescence microscope; the red and blue circles represent the high spatial frequency information that can be coupled into the passband of the OTF through SP interference illumination excited by 563 and 390 nm light, respectively.

wavelength 580 nm) is used to acquire the point spread function (PSF). The full width half maximum (FWHM) of the PSF shown in Figure 2.5 a and Figure 2.5 c are about 214 nm and 74 nm respectively. The comparison between the PSF of conventional epi-fluorescence microscopy (Figure 2.5 a) and that of PSIM (Figure 2.5 b-d) shows a \sim 3-fold resolution improvement, which is better than the typical two-fold improvement in SIM [15, 16]. The simulation is also repeated for an object formed by randomly positioned 10 nm quantum dots (emission wavelength 580 nm) to further illustrate the imaging performance. Compared with the conventional epi-fluorescence microscopy image (Figure 2.5 e), the reconstructed PSIM image sourced from 563 nm excitation light (Figure 2.5 f), from 390 nm light (Figure 2.5 h), and from the combination of the two (Figure 2.5 g) all show drastic resolution improvements. Such improvement is also obvious from the coverage in the Fourier space representations (Figure 2.5 i-l). The resolutions are about the same for Figure 2.5 g and Figure 2.5 h because the radii of the covered area in Fourier space are almost the same. However, the process of getting image (d) is twice as fast as that of getting image (c) because SP interference patterns with only one spatial frequency are used as the illumination source. Moreover, in principle, the artifacts in (d) and (h) can be removed by numerical processes [15, 16, 19, 57].

2.3.2 Thin plasmonic substrate and its imaging capability demonstration

Since SP modes on thin-metal-film/dielectric interfaces possess even larger k vector compared with that on semi-infinite-metal/dielectric interface, we also designed a thin-metal-film/dielectric structure for PSIM. As shown in the structure of a unit cell (Figure 2.6 a), an optimized Cr structure is used to excite the SP modes in the Ag thin film with relatively good efficiencies. When two modes (Figure 2.6 blue lines) are excited at the same time on the thin-metal-film/dielectric interface, the counter-propagating SP waves excited from two adjacent slits can form an interference pattern containing multiple spatial frequencies [58]. The thickness of the Ag film chosen is determined by the SP modes needed. In general, the larger the SP mode needed, the thinner the metal film. In this particular design, the thick-

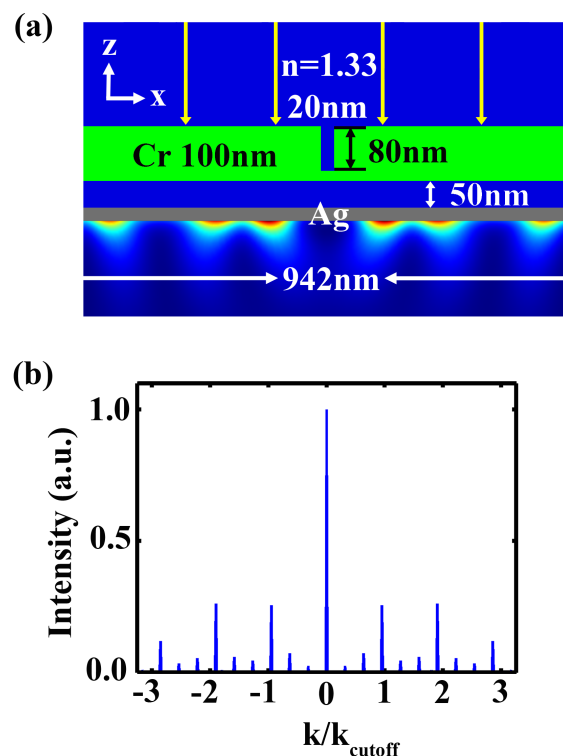


Figure 2.6: (a) Structure and SP interference pattern (time-averaged electric energy density distribution) excited by 442 nm light; (b) Fourier transform of interference pattern measured 20 nm under Ag film.

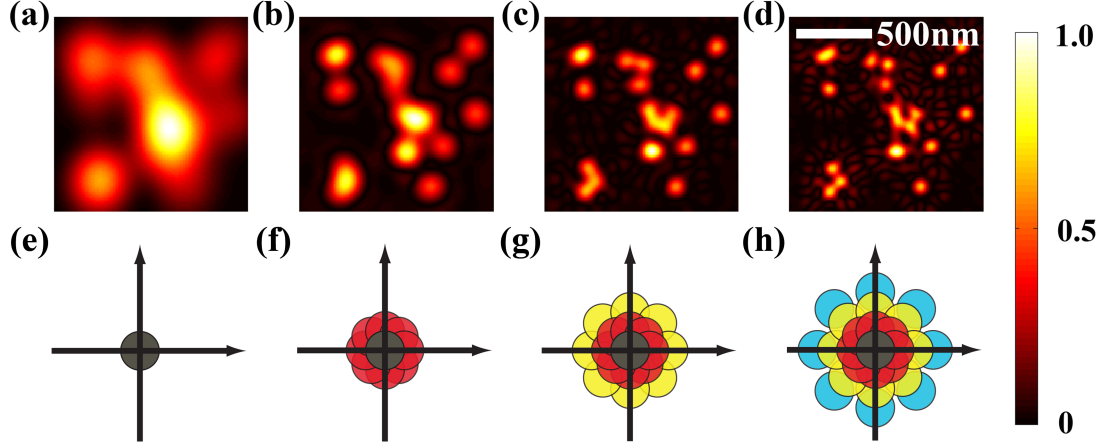


Figure 2.7: PSIM imaging ability demonstration. (a) Conventional epi-fluorescence microscope image; (b-d) Reconstructed images; (e-h) Corresponding k space representations. Different colors represents the information obtained from different orders of the illumination patterns.

ness of the Ag film is 17 nm. 442 nm excitation light and fluorescent particles with 508 nm emission wavelength were used in the simulation. The NA is set to 0.85 so that a dry objective lens can be used for this design. The time-averaged electric energy density distribution measured 20 nm under the Ag film (Figure 2.6 a) shows the multi-mode interference pattern. The corresponding Fourier Transform (Figure 2.6 b) has peaks around $1k_{\text{cutoff}}$, $2k_{\text{cutoff}}$ and $3k_{\text{cutoff}}$, which is consistent with the first three peaks of the calculated values from the interference between the two SP modes ($(|k'_{sp2}| - |k'_{sp1}|, 2|k'_{sp1}|, |k'_{sp1}| + |k'_{sp1}|)$). The intensity of the 4th peak is so weak for this specific design that its contribution can be reasonably ignored. Using the same method as thick film simulations, we conducted the PSF simulation and imaging performance simulation for thin film structure. The conventional epi-fluorescence microscopy image and reconstructed images of an object formed by randomly positioned 10 nm fluorescent particles are presented in Figure 2.7. The full width half maximum (FWHM) of PSF that corresponds to Figure 2.7 h is about 76 nm, which corresponds to a ~ 4 -fold resolution improvement compared with the conventional epi-fluorescence microscopy.

2.4 Discussion

One assumption we made in imaging simulations is that the fluorescence signal is proportional to the SP intensity. The second assumption is that the change of the SP interference patterns is negligible with the presence of the fluorescence object, because the existence of the fluorescence dye will not considerably alter the SP propagation length in experiment [59]. Moreover, we want to emphasize that the detected light is not the SP interference patterns but the emission light from fluorescent particles or quantum dots. Therefore, although the SP interference patterns only exist at the near field of the metallic surface, we can still record the image from far field. The two designs described above serve as examples to demonstrate the imaging principles and performance of PSIM. Based on the simulation results, we can conclude that PSIM can achieve sub-diffraction limit resolution. Moreover, the wave vector of SP mode is adjustable by changing the structure. Depending on the applications, various parameters such as the excitation wavelength, refractive index of the surrounding media, material, as well as structures can be adjusted in order to get better improvement in terms of resolution, speed, or both. While we only showed 1D SP interference pattern in our numerical simulations, it is possible to acquire 2D SP interference pattern through proper designs [27, 28]. There is no limitation on the imaging size of the PSIM if a periodic plasmonic structure is utilized, although the period of the structure should be limited by the SP propagation length.

One of the advantages of PSIM is that the resolution does not solely depend on the NA of the optical microscope, as with SIM. The resolution of SIM can be written as $\lambda_{\text{emission}}/[2NA + 2NA(\lambda_{\text{emission}}/\lambda_{\text{excitation}})]$, which is approximately $\lambda_{\text{emission}}/4NA$ when $\lambda_{\text{emission}}/\lambda_{\text{excitation}}$ is about 1; while the resolution of PSIM is $\lambda_{\text{emission}}/2(2NA + 2NA_{\text{effective}})$, in which $NA_{\text{effective}}$ is $\lambda_{\text{emission}}/\lambda_{sp}$. Since $\lambda_{\text{emission}}/\lambda_{sp}$ is independent of objectives and usually larger than a possible NA provided by common objectives, PSIM can achieve higher resolution than SIM even with small NA objectives. Also, PSIM has higher resolution improvement compared with a pure dielectric structure. Since the dispersion curve of SPs lie on the right side of that of the photons in the same media, metal/dielectric structures can

always generate interference patterns with larger spatial frequency compared to a dielectric structure. Moreover, PSIM can selectively excite fluorescent objects in a thin region close to the metal surface because the SP exponentially decays along the z direction. Therefore, specimens that are far from the interface won't contribute to the strong background as in the case of epi-fluorescence microscopy. In general, the z direction imaging depth depends on the resolution improvement along the x-y directions, and usually decreases as the x-y resolution increases [20]. If the imaging region of interest is only several tens of nanometers away from the interface, PSIM is a good imaging tool to use. Multicolor imaging is possible since different fluorescent dyes can be excited if SP modes with different frequency can be excited on a properly designed metallic structure. PSIM itself doesn't require a high power laser, but it can also be combined with the nonlinear dependence of the emission rate on the illumination intensity. Similarly to SSIM, through utilizing higher harmonic peaks, saturated PSIM can achieve even larger resolution.

Besides the various advantages mentioned above, this technique also has its limitations. PSIM is intrinsically a 2D imaging technique that can only form a high-resolution image of objects close to the metal surface. Although a spacer layer between the object and the metal film can reduce the quenching effect [60, 61], the fluorescence efficiency is less in PSIM than in conventional SIM. Moreover, complicated designs might be needed for higher resolution improvement. Since the decay length along both x-y and z directions gets shorter as the wave vector of the SP increases, researchers may need to find a balance when doing actual designs.

2.5 Conclusion

In conclusion, a new super-resolution imaging technique, plasmonic structured illumination microscopy (PSIM) is numerically demonstrated. Simulation results have shown that a resolution improvement larger than that of SIM can be achieved without utilizing nonlinear dependence of the fluorescence emission rate on the illumination intensity. The reconstructed images using two plasmonic designs show three-four fold resolution improvement compared to epi-fluorescence

microscopy. The PSIM may have important applications in the field of high-resolution biomedical imaging.

The authors thank A. A. Schfagans, R. Aguinaldo and G. C. So for their useful discussions. This research is partially supported by NSF-ECCS under Grant 0969405.

Chapter 2, in part, is a reprint of the material as it appears in Nano Letters 2010, 10, 2531-2536. Feifei Wei, Zhaowei Liu, "Plasmonic Structured Illumination Microscopy". The dissertation author was the first author of this paper.

Chapter 3

Experimental demonstration of PSIM

3.1 Instrument development for PSIM

3.1.1 PSIM system overview

To performing the PSIM experiments, the designed PSIM system should fulfill two primary functions: (1) changing the illumination angle to laterally translate the SPI; (2) detecting the diffraction-limited fluorescence image from the sample for PSIM reconstruction. The PSIM imaging system was built based on an upright Zeiss Axioskop microscope, consisting of four major modules: (1) light source module, (2) illumination angle control module, (3) illumination angle characterization module and (4) fluorescence image detection module, as shown in Figure 3.1.

3.1.2 Light source module and illumination angle control module

Three continuous lasers with wavelength at 405 nm, 488 nm and 532 nm were used as the light source due to their wide application in bio-sample fluorescence microscopy. The three light beams are aligned and combined together

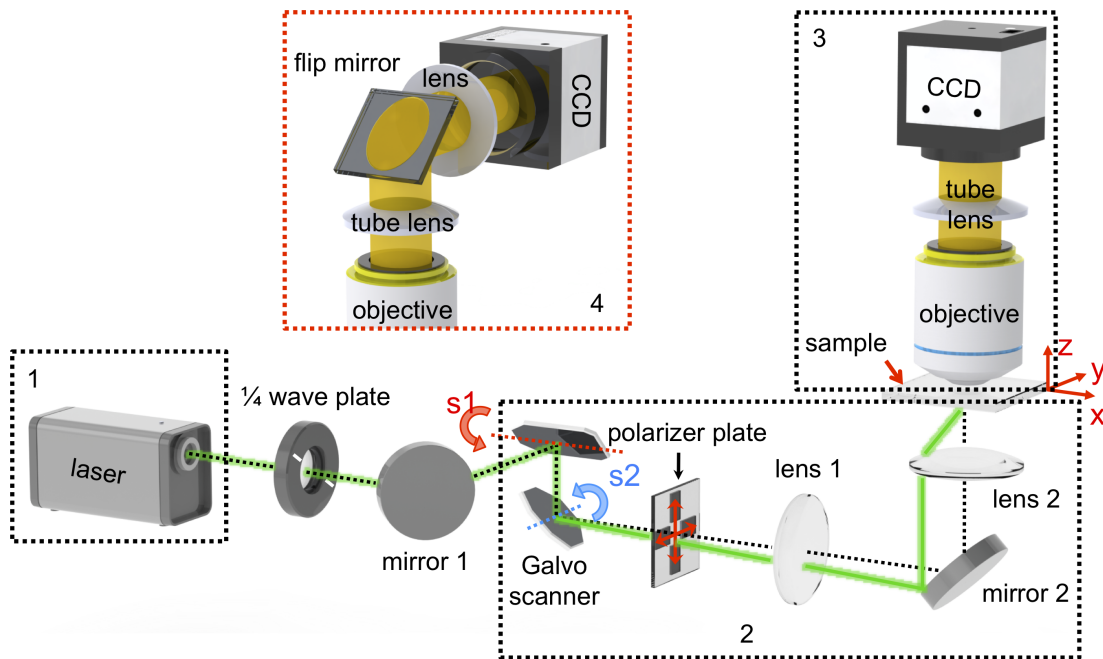


Figure 3.1: Schematics of the automated PSIM system, with the four modules highlighted by dashed squares. Modules 1-4 represent the light source module, the illumination angle control module, the fluorescence image detection module and the illumination angle characterization module, respectively.

through two dichroic beam splitters as shown in Figure 3.2 a. The aligned light beam is then guided to the microscope through the illumination angle control module (Figure 3.2 a) to illuminate the PSIM substrate. The illumination angle control module consists of a 2D Galvo scanner, a polarizer plate, and a 4f system formed by lens 1 and 2, as shown in Figure 3.3 a. When a 2D slit array patterned plasmonic structure is illuminated by the laser beam, as shown in Figure 3.3 b, the SPI pattern is formed by the interference of the counter propagating SP waves generated at the adjacent slits. The lateral shift of the SPI pattern is realized by adjusting the phase difference between the counter-propagating SP, which is achieved by changing the illumination angle with the 2D Galvo scanner combined with the 4f lens system. The Galvo scanner is chosen due to its high-speed kHz rate angle tuning capability and high efficiency. The 2D Galvo scanner based illumination angle tuning system has higher efficiency compared with DMD based system, because it is based on mirror rotation, instead of amplitude grating diffraction for angle tuning. The reflectivity of the 3 mm protected silver (Ag) mirrors used in the Galvo scanner is more than 85% across the whole visible spectrum [62]. The illumination angle tuning in x-z and y-z planes are controlled by the rotation of the s2 and s1 mirror of the Galvo scanner, respectively, with s2 mirror placed at the focal plane of lens 1 and the sample placed at the focal plane of lens 2. The orientation of the SPI pattern is controlled by both the orientation of the slits as well as the polarization direction of the incident light. To excite the SP wave with desired propagation direction and form 1D SPI, p-polarized light (with its polarization direction in the illumination plane) is needed as the illumination light source. This could be achieved by passing the laser light through a custom-made phase plate. Different areas of that polarization plate is made of polarizers with different polarization directions, as indicated by the phase plate in Figure 3.1, in which the polarization directions of the horizontal pair and vertical pair of polarizers are indicated by the red horizontal and vertical arrows respectively. Finally, the fluorescence light excited by SPI illumination is collected by an objective and forms a diffraction-limited image through a tube lens onto an electron multiplying charge coupled device (EMCCD).

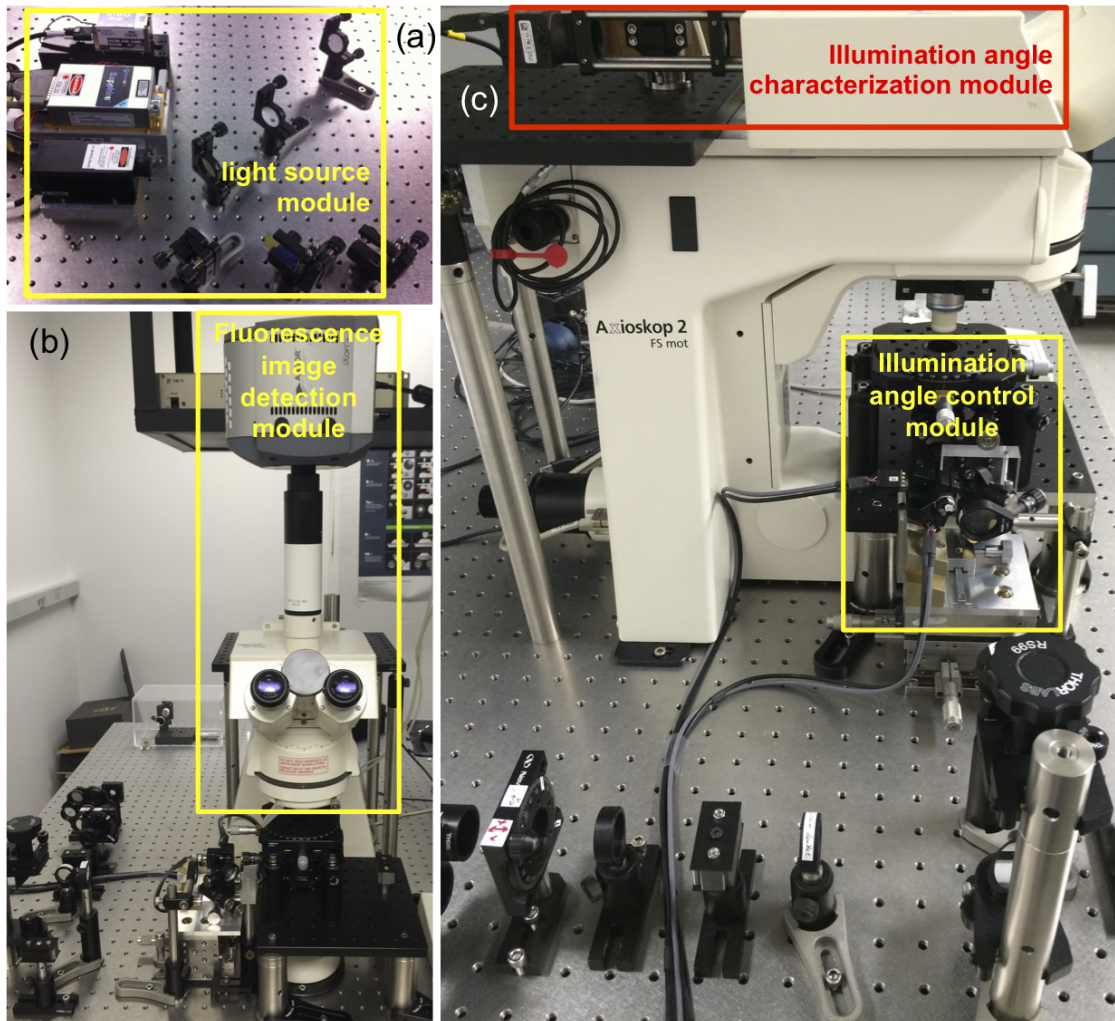


Figure 3.2: Photos of the PSIM system with four modules highlighted by solid squares. (a) Light source module. (b) Front view. (c) Side view.

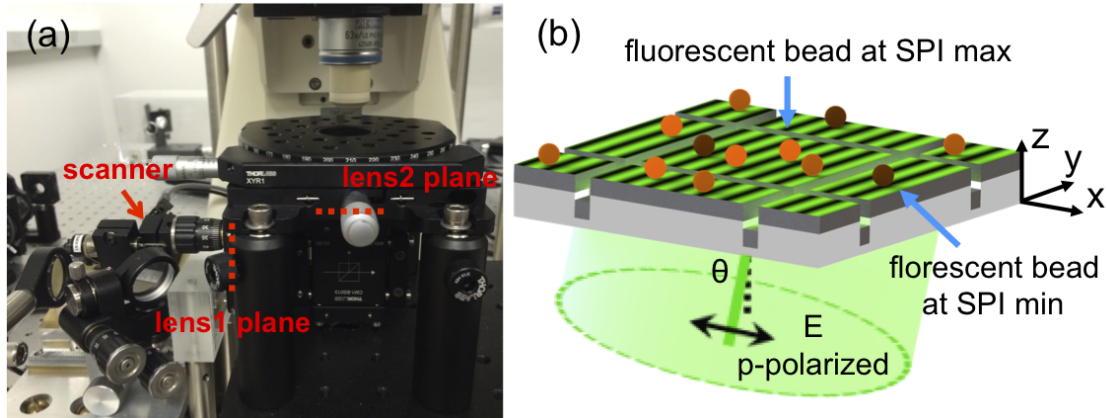


Figure 3.3: (a) Photo of the illumination angle control module. (b) Schematic view of the sample region.

3.1.3 PSIM system synchronization and data acquisition

The PSIM system is synchronized through three synchronized signals, two analog and one digital. The two synchronized analog signals, as shown in Figure 3.4 the red and green signals, are used to control the rotation angle of the horizontal and vertical scanning mirror respectively, with the mirror rotation angle proportional to the amplitude of the control signal. As a result, the illumination angle increases accordingly as the voltage of the scanning mirror control signal increases, as is shown in Figure 3.4 b. After certain delay time specified by the user in LabView, a digital pulse signal (represented as the blue signal in Figure 3.4 a) is generated to trigger the Andor Xion 897 camera for image acquisition. Moreover, the frequency of the synchronization signal can be further increased by a microcontroller unit (MCU) based or linked function generators based synchronization algorithm for high-speed PSIM purpose.

3.1.4 Illumination angle characterization module

The illumination angle is measured through a custom-built Fourier-space imaging system (schematics and photo shown in Figure 3.5 a and Figure 3.5 b respectively), which consists of a lens and a charge coupled device (CCD) placed at its focal plane. With the help of a flip mirror, the light collected by the objective

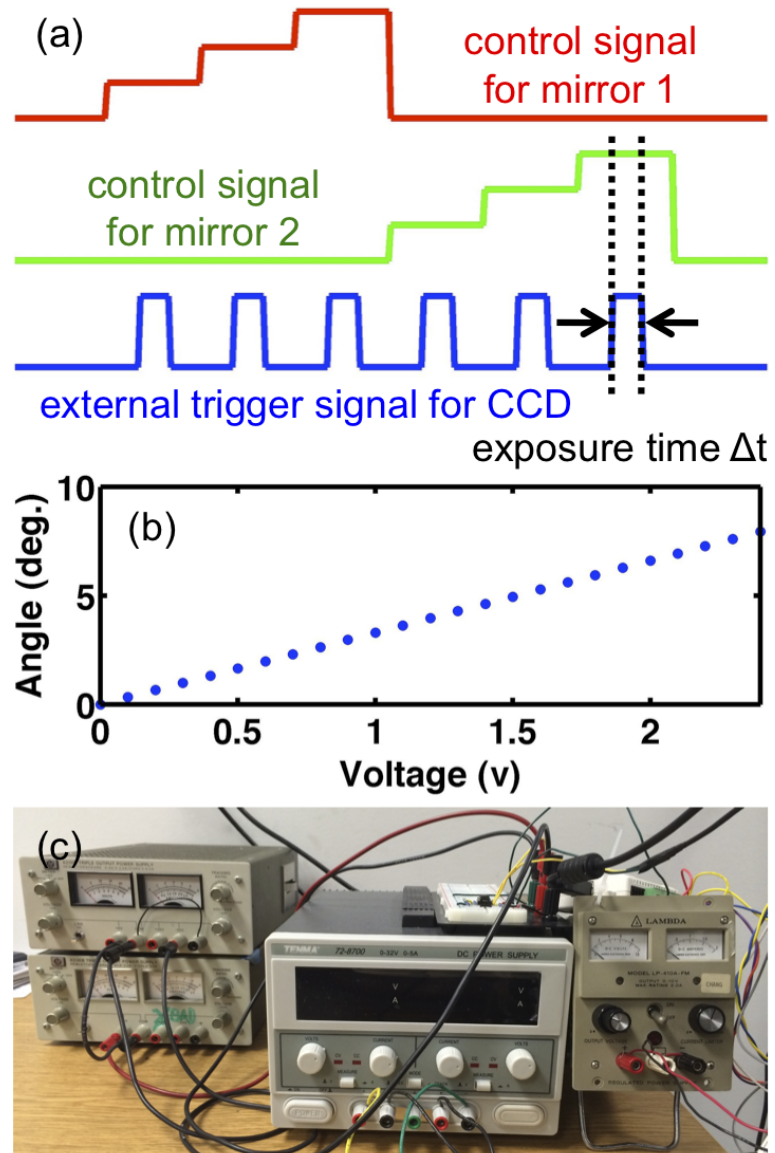


Figure 3.4: (a) Time sequence of the synchronization signals; (b) illumination angle in x-z plane vs. the control signal voltage of the s2 scanning mirror; (c) a photo of the control electronics.

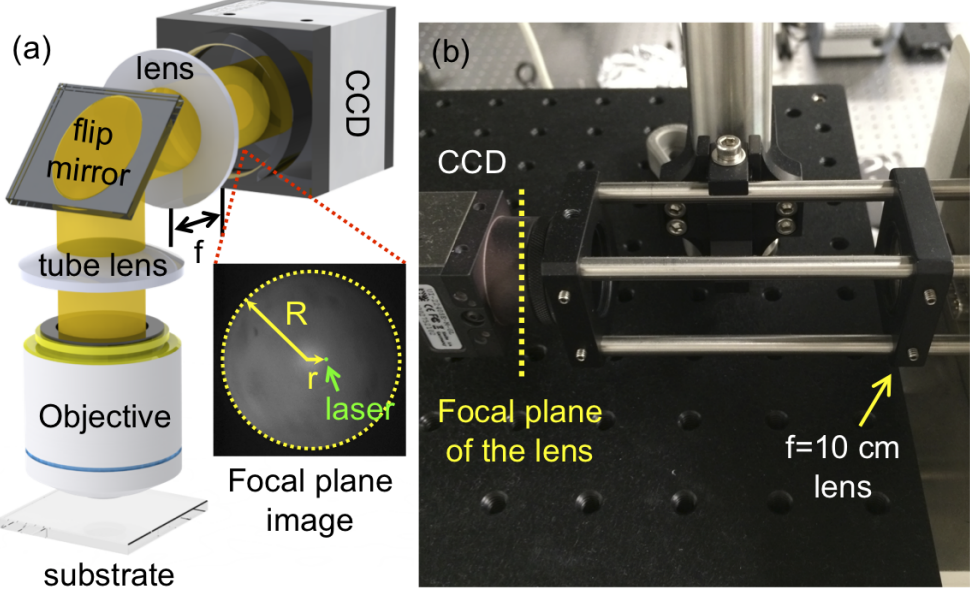


Figure 3.5: (a) Schematics and (b) photo of the illumination angle characterization system.

can be delivered either to the EMCCD for PSIM imaging or to the Fourier-space imaging system for illumination angle characterization. The inset in Figure 3.5 a is a typical Fourier-space image measured with both PSIM laser illumination and conventional LED illumination turned on. The LED illumination fills up the whole illumination aperture of the objective, highlighted by the dashed yellow circle. Due to the small divergence angle of the illumination laser, the laser light focuses to a small green dot in the CCD plane. The illumination angle θ can be estimated by $r/R = \sin(\theta)/NA$, with NA being the numerical aperture of the objective. The r parameter is the distance between the green laser illumination dot and the center of the objective aperture, and R is the radius of the objective aperture, as indicated in Figure 3.5 a inset.

3.2 Plasmonic substrate design and fabrication

In our proposed and theoretically demonstrated PSIM in 2010 [44], the SP is excited by edges or slits and the SPI pattern laterally translated by adjusting

the illumination angle. In this SP excitation configuration, the maximum k_{sp} that could be excited is no longer constrained by the objective NA. Moreover, the slit array excitation configuration, with sub-wavelength slit width and period on the order of the SP propagation length, minimizes the coupling structure area and removes the constraint of the imaging area caused by SP propagation length.

3.2.1 Plasmonic substrate design

The first sets of PSIM experiments are for concept demonstration, to validate the SPI pattern translation and demonstrate image resolving power higher than conventional SIM. Therefore, the plasmonic substrate designed for these experiments only contains a single layer of plasmonic material and is relative easy to fabricate.

In the plasmonic substrate design, fused silica (SiO_2) is chosen as the substrate due to its transparency in the visible spectrum and water is selected as the surrounding media because most of the bio-fluorescence measurements are performed in aqueous environments. In regard to the plasmonic material, silver (Ag) was chosen as the material supporting SP generation because the SP at a Ag/dielectric interface can be generated for the entire visible spectrum with relatively low loss, as long as the wave vector mismatch between the incident photon and SP is compensated. The dispersion of the SP modes supported at semi-infinite Ag/water interface can be calculated from $k_{sp} = \frac{\omega}{c} \sqrt{\frac{\epsilon_s \epsilon_{Ag}}{\epsilon_s + \epsilon_{Ag}}}$, in which ω is the angular frequency of the illumination light; ϵ_s and ϵ_{Ag} are the dielectric constant of the surrounding media and Ag, respectively. The supported SP modes, shown in Figure 3.6 a, could be used to form the SPI needed for PSIM experiments and estimate theoretical resolution improvement. Moreover, the Ag film not only supports SP waves, but also attenuates the illumination light so that the SP field dominates at the object plane for fluorescent dye excitation. The penetration depth can be estimated by $\frac{\lambda}{2\pi \cdot \text{Im}(n_{Ag})}$ for perpendicular illumination [20], in which λ is the illumination laser wavelength and $\text{Im}(n_{Ag})$ is the imaginary component of the refractive index of Ag. Based on the transmitted electric field vs. the Ag film thickness curve shown in Figure 3.6 b, a relatively thick Ag film (250 nm) is chosen in our

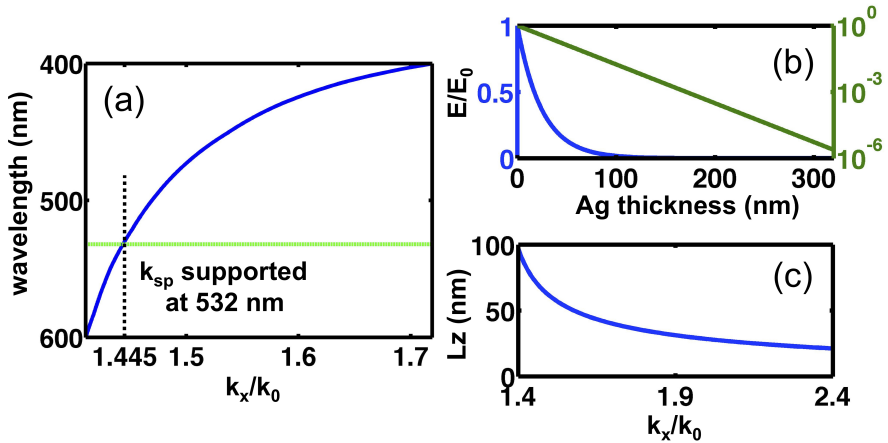


Figure 3.6: (a) The dispersion curve for SP mode supported at a semi-infinite Ag/water interface, with the intersection between the blue line and the green line indicating the k_{sp} mode supported under 532nm illumination. (b) Directly transmitted E-field vs. Ag thickness for perpendicular illumination at 532 nm. The blue line and green line correspond to linear and log scale plot, respectively. (c) The intensity Z decay length vs. SP mode wave vector excited at 532 nm with water as surrounding media ($n=1.33$). The dielectric constant of Ag used in the calculation is adopted from Johnson & Christy paper [55].

plasmonic substrate design to ensure that the SP field is much stronger compared with the directly transmitted laser field.

The slit period is set to be around the propagation length of the SP waves for relatively uniform interference pattern generation. The propagation length is given by $\frac{1}{\text{Im}(k_{sp})}$, with $\text{Im}(k_{sp})$ corresponding to the imaginary part of the SP wave vector and eventually being related to the loss of the Ag film. For 532 nm laser excitation with water as surrounding media ($n=1.33$), 7.6 μm slit period with 100 nm slit width were chosen for the plasmonic substrate. Moreover, in PSIM, the fluorescent object should be placed within the intensity decay length of the SP field, which ranges from several tens of to hundreds of nanometers, depending on the SP wave vector. Fluorescent dyes that are several intensity decay lengths away from the plasmonic substrate surface would provide negligible background fluorescence due to the weak excitation field intensity. Similar to Total Internal Reflection Fluorescence (TIRF) microscopy, this yields a high axial resolution for surface imaging. Figure 3.6 c provides an example of the intensity decay length for

SP field with wave vector (k_{sp}) range from $1.4k_0$ to $2.4k_0$ (k_0 the free space wave vector of the illumination laser), excited at 532 nm with the surrounding media being water (n=1.33).

3.2.2 Plasmonic substrate fabrication

The designed plasmonic substrate could be fabricated by standard nano-fabrication techniques. Figure 3.7 shows the major steps of the substrate fabrication procedures. A fused silica (SiO_2) wafer was chosen as the substrate due to its transparency in the visible spectrum. First, a slit array with 100 nm slit width and $7.6 \mu\text{m}$ period was produced on the fused silica substrate using electron beam lithography (step1). For the millimeter scale sample, the slit array pattern can be fabricated by nano-imprint lithography due to its large area stamping capability, master mode reusability and low cost. The patterned resist served as a dry etching mask to transfer the pattern into fused silica (step 2), followed by the standard piranha solution cleaning process to remove the residue resist (step3). Finally, a 4 nm titanium (Ti) adhesion layer and a 250nm Ag film were deposited on the patterned substrate using electron beam deposition at 2×10^{-7} Torr (step 4). The optical as well as the scanning electron microscopy characterization of the fabricated substrate are presented in Figure 3.8.

3.3 Experimental demonstration of the SPI lateral translation

3.3.1 PSIM sample preparation and measurements

In our experiments, 100 nm diameter fluorescent beads (Life Technologies, F8800) were used as the probes for SPI shift characterization and the object for PSIM imaging capability demonstration. One μl of 100 nm diameter fluorescent bead solution was drop-casted onto the slit-array patterned plasmonic structure and air-dried, with the sparsity of the beads controllable by the solution concentration (about 1.2×10^{10} beads/ml for experiments will be shown in the later section

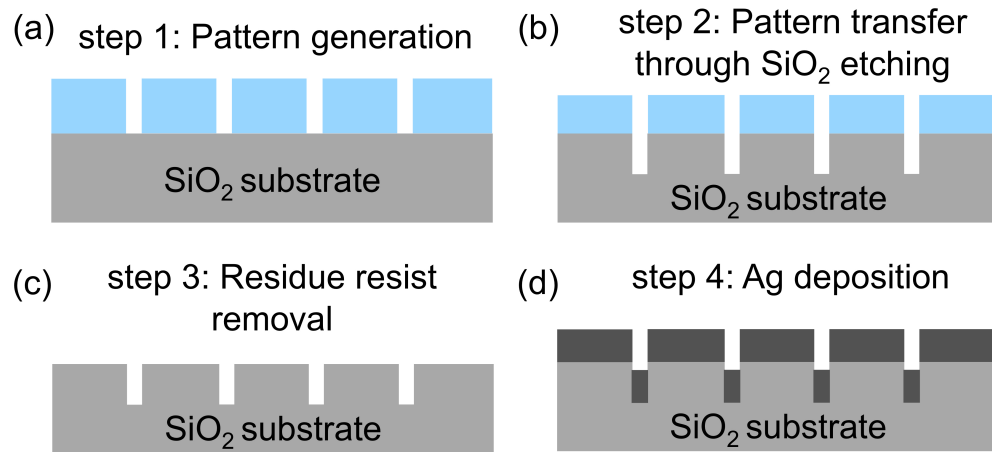


Figure 3.7: Major procedures for substrate fabrication. The blue squares represent the electron beam resist or nano-imprint resist, and the dark gray squares represent the deposited Ag film.

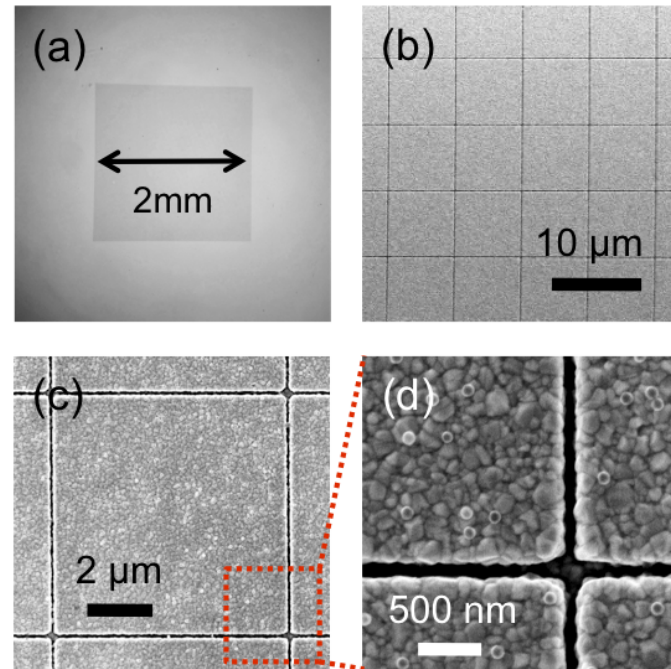


Figure 3.8: The fabricated plasmonic substrate characterization. (a) Reflection bright field image of the nano-imprint fabricated, large area patterned SiO_2 substrate after Ag deposition. (b) The sanning electron microscopy (SEM) image of the electron beam lithography fabricated, small area patterned SiO_2 substrate after Ag deposition. (c) The magnified SEM image of one unit cell and (d) further magnified SEM image of the slits.

of §3.3 and then in §3.4).

The PSIM measurements for experiments shown in this section (§3.3) and §3.4, were performed on our custom-built automated PSIM platform shown in Figure 3.1 and Figure 3.2. The linear polarized light coming out of a 200 mW, 532 nm laser is converted to circular polarized light by a quarter waveplate, and then reflected to the 2D Galvo scanner (Cambridge Technology 6210H) and a 4f system. These elements control the illumination angle variation in x-z and y-z planes. After passing the polarizer plate placed between the scanner and the 4f system, only illumination light with proper polarization is allowed to illuminate the PSIM substrate to excite desired 1D SPI pattern. As the relative incident angle difference varies in x-z and y-z plane, the phase difference between the SP waves excited at the two adjacent edges increases accordingly, leading to a lateral translation of the SPI pattern. Then the PSIM fluorescent images formed by SPI illumination were collected by a $63\times$ water-dipped objective (Zeiss W Plan-Apochromat $63\times$, NA=1.0 Ph3) and then recorded by an EMCCD (Andor 897), with a 593 ± 30 nm band-pass filter (Semrock Inc.) placed in the detection light path. To compensate the angle-dependent illumination intensity variation, the detected fluorescent images were normalized by the corresponding intensity of the scattered laser light at the slits under the same illumination angle. The illumination and image acquisition modules were synchronized by a Labview-controlled DAQ (data acquisition card).

3.3.2 Demonstration of the lateral translation of the SPI

For demonstrating the lateral translation of the SPI pattern, fourteen diffraction limited images were recorded, with relative illumination angle varying from 0 degree to about 4.3 degree at equal step in either x-z or y-z plane. The red dots in Figure 3.9 b and Figure 3.9 c represent the fluorescence intensity variation of a single 100nm fluorescence bead with respect to illumination angle change in x-z and y-z plane, with both the SPI pattern orientation and the x-y plane component of the polarization vector (labeled by the red arrows) along x and y direction respectively. The fluorescence intensity curves can be fitted by a sinusoidal function

indicated by the solid blue lines, which confirms that the SPI is indeed generated through slits coupling and laterally translated by adjusting the incident angle of the illumination laser beam as expected. As for a group of randomly distributed beads, the lateral shift of the PSI pattern results the intensity distribution of the PSIM fluorescence image changes accordingly, as is shown by Figure 3.9 d-i.

3.4 Experimental demonstration of PSIM super-resolution imaging capability

3.4.1 Super-resolution image reconstruction through Fourier space based algorithm

To reconstruct a super resolution image (such as PSIM reconstructed images shown in §3.3), only three diffraction-limited images, illuminated by three 1D SPI patterns with about one third of the period lateral shift between each other, are needed for each direction. This process was performed for both x and y direction oriented interference patterns to achieve two-dimensional resolution improvement, yielding a total of six image acquisitions. The epi-fluorescence images were collected using the same objective and EMCCD under light emission diode (LED) illumination, but with a 523 ± 10 nm and a 585 ± 10 nm filter as the illumination and detection filter, respectively. For our experimental demonstration, a total of 6 diffraction-limited images under 1D SPI illumination laterally translated along both x and y directions were used for super-resolution image reconstruction. The super-resolution image (Figure 3.10 b), reconstructed with a conventional SIM reconstruction algorithm [15], shows obvious resolution improvement compared with the conventional epi-fluorescence image (Figure 3.10 a). The Fourier transform of the reconstructed image (Figure 3.10 d) confirms that the high spatial frequency information (labeled by the four red dashed circles) is indeed extracted from the six diffraction-limited images. The full width half maximum (FWHM) (Figure 3.10 e top) of a single 100 nm diameter fluorescent bead decreases from 342 nm to 129 nm, yielding a factor of 2.65 times resolution improvement, which matches

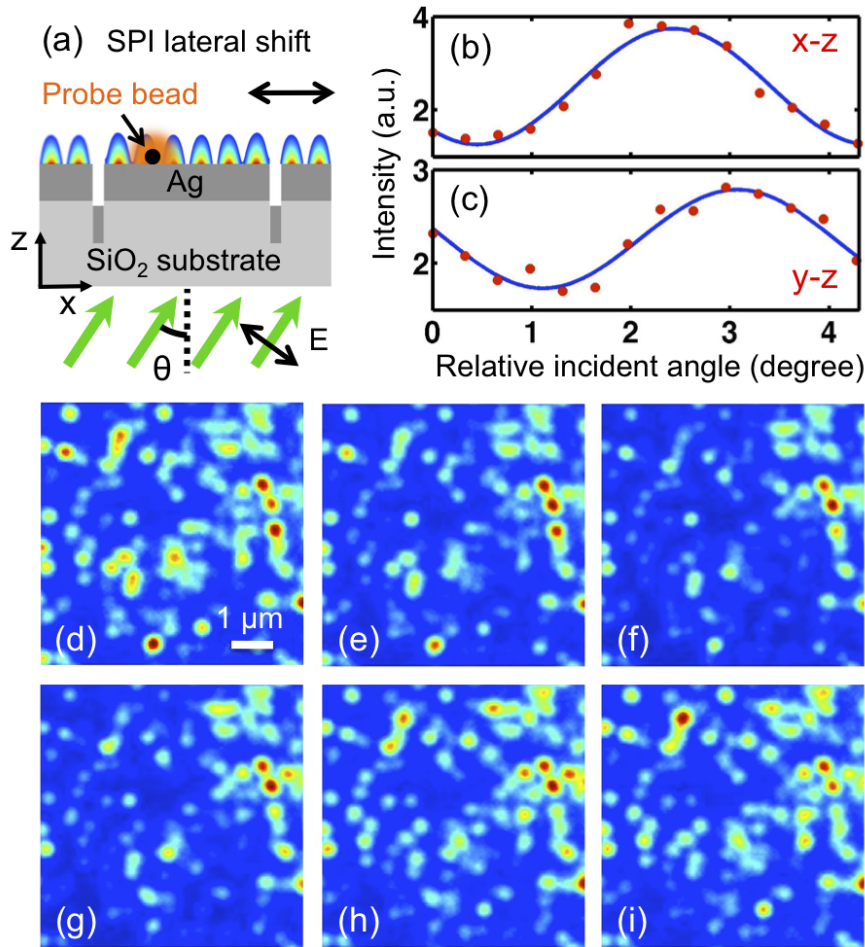


Figure 3.9: Experimental demonstration of the SPI lateral shift. (a) Schematics of the SPI lateral translation characterization configuration. (b-c) Fluorescence intensity vs. illumination angle change in x-z and y-z plane respectively, in which the measured data and the sinusoidal fit are represented by the red dots and the solid blue lines. (d-i) Six PSIM fluorescence images excited by the SPI patterns formed under laser illumination with 6 different incident angles in x-z plane. The corresponding SP shift between adjacent PSIM fluorescence images is about 0.16 SPI period. The fluorescence intensity is normalized by its own maximum and represented by pseudo color, with the range of the color bar from 0 to 1.

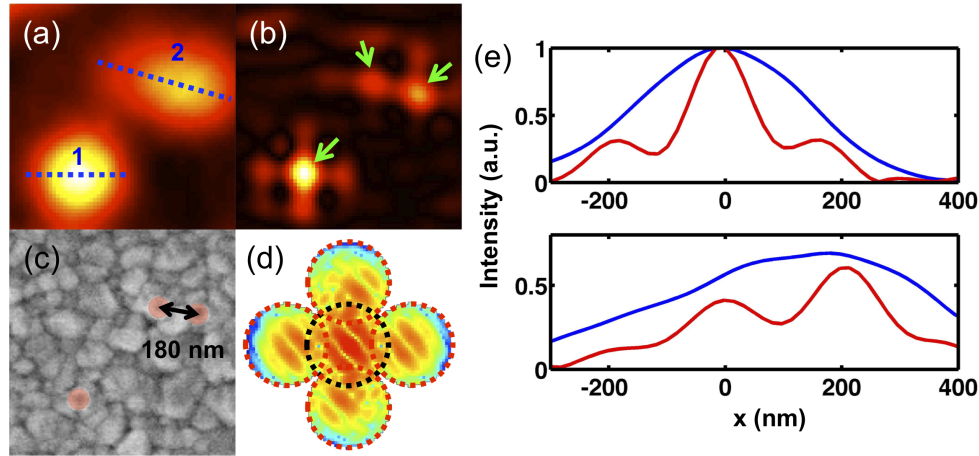


Figure 3.10: (a) Conventional epi-fluorescence image, (b) reconstructed PSIM image of 100 nm fluorescent beads with green arrows indicating the beads location; (d) the SEM image of the object, with beads highlighted by red circles; (d) Fourier transform of (b) in log scale; (e) Cross section comparison along line 1 (top) and line 2 (bottom). The blue lines and red lines correspond to the cross sections of the conventional epi-fluorescence image and the reconstructed PSIM image respectively.

with theoretical estimation (about 2.6 times) based on the SPI period and the numerical aperture of the detection objective. The cross section comparison along line 2 (Figure 3.10 e bottom) clearly shows that two beads with center-to-center distance smaller than diffraction limit (about 180 nm apart) can be separated by PSIM microscopy. Although the conventional SIM reconstruction algorithm works for small area reconstruction of PSIM measurements (such as Figure 3.10 b and Figure 3.10 c), large area image reconstruction shows noticeable distortions caused by the imperfection of the SPI pattern.

3.4.2 Super-resolution image reconstruction through Blind-SIM based algorithm

To avoid the reconstruction artifacts, an iterative code, adapted from a Blind Structured Illumination Microscopy (Blind-SIM) reconstruction algorithm [6] was developed for PSIM image reconstruction. The Blind-SIM reconstruction algorithm exploits multiple measurements under different illuminations to recon-

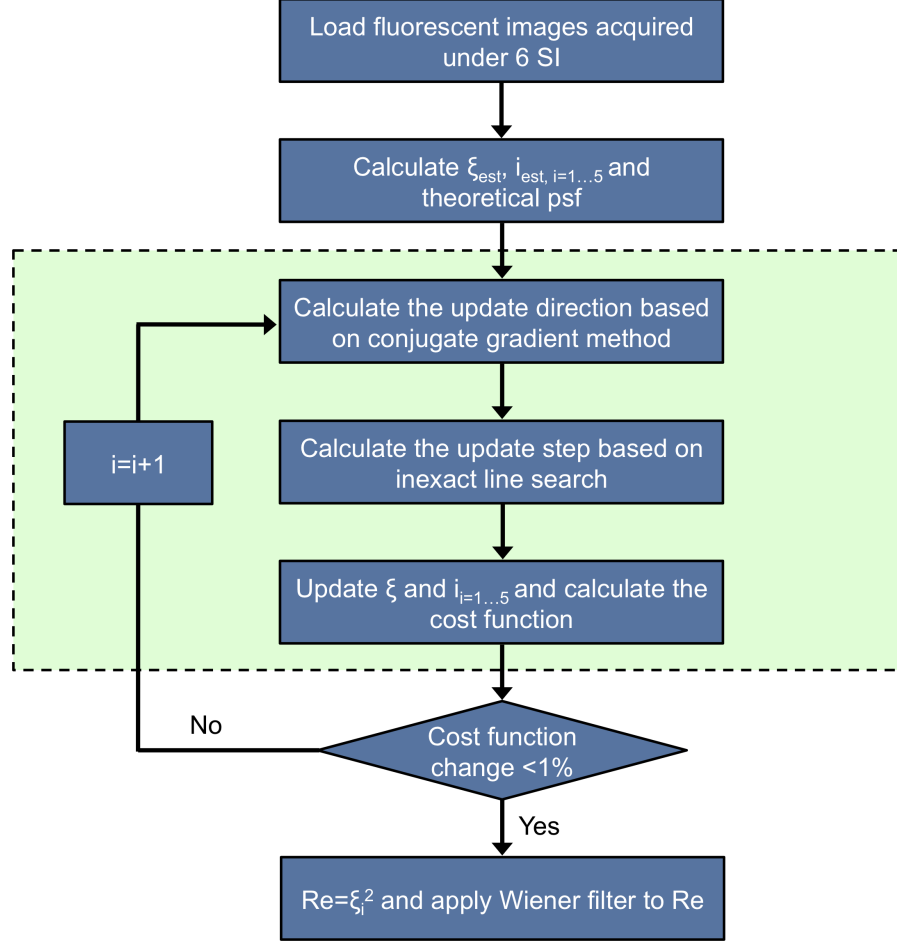


Figure 3.11: The workflow of the Blind-SIM algorithm.

struct the sample fluorescence distribution without knowing the illumination information before hand. This algorithm is capable of reconstructing the desired high-resolution image even if the illumination patterns have distortions compared to predicted interference patterns [63].

The Blind-SIM reconstruction method is an L2 norm-based minimization algorithm that exploits multiple diffraction-limited images taken under various spatially varying illuminations to estimate the fluorescence distribution of the object [7]. The iterative code, used for large area image reconstruction, jointly recovers the object (obj) and the illumination patterns ($I_{i=1,\dots,5}$) through minimizing the cost function, $F(obj, I_{i=1,\dots,5}) = \sum_{i=1}^5 ||im_i - (obj \cdot I_i) * psf||^2 + ||im_6 - (obj \cdot (6I_0 - \sum_{i=1}^5 I_i)) * psf||^2$, under the positivity constraint of obj and

$I_{i=1,\dots,5}$, and the $\sum_{i=1}^6 I_i \approx 6I_0$ constraint [63]. In the cost function, I_0 is constant, meaning that the object is on average uniformly illuminated and the psf stands for the point spread function of the microscope and can be estimated based on the NA of the objective. The $im_{i=1,\dots,6}$ corresponds to the six diffraction-limited images taken under 3 laterally translated 1D SP interference illuminations along both x and y directions; * stands for convolution; and $\| \|^2$ represents the L2 norm. To start the iterative calculation, the diffraction-limited image of the object and uniform intensity illumination are used as the initial guesses. The iterative changes of obj and $I_{i=1,\dots,5}$ are calculated by the conjugate gradient method and an inexact line search. The recovered obj was then filtered by a wiener filter using the theoretical super-resolution psf to enhance the high spatial frequency components in Fourier space for better image contrast. The deconvolution of epi-fluorescence image is estimated based on the same procedures, minimizing $F(obj) = \|im - obj * psf\|^2$ using the diffraction-limited image as the initial guess, and then filtering by a wiener filter using the same theoretical super-resolution psf to enhance the high spatial frequency component. The workflow of this iterative super-resolution image reconstruction algorithm and the evolution of the recovered object are shown in Figure 3.11 and Figure 3.12, respectively. As the iteration number increases, the resolution of the recovered object gets higher and higher (Figure 3.12 a-f), and the cost function value decreases accordingly (Figure 3.12 g). Similar to other error reduction method, the cost function decreases fastest at the beginning, then gradually slows down and finally reaches a local minimum.

The super-resolution image of three beads (Figure 3.13 b) shows obvious resolution improvement compared with the conventional epi-fluorescence image (Figure 3.13 a), with a SEM image provided in Figure 3.13 c to confirm the bead distribution. The comparison of their corresponding Fourier transforms (shown in Figure 3.13 d and Figure 3.13 e respectively) confirms that high spatial frequency information beyond the pass band of conventional epi-fluorescence microscopy is indeed extracted from the six diffraction-limited images. The full width half maximum (FWHM) (Figure 3.13 f) of a single 100 nm diameter fluorescent bead decreases from 327 nm to 123 nm (averaged based on the red and green curves shown

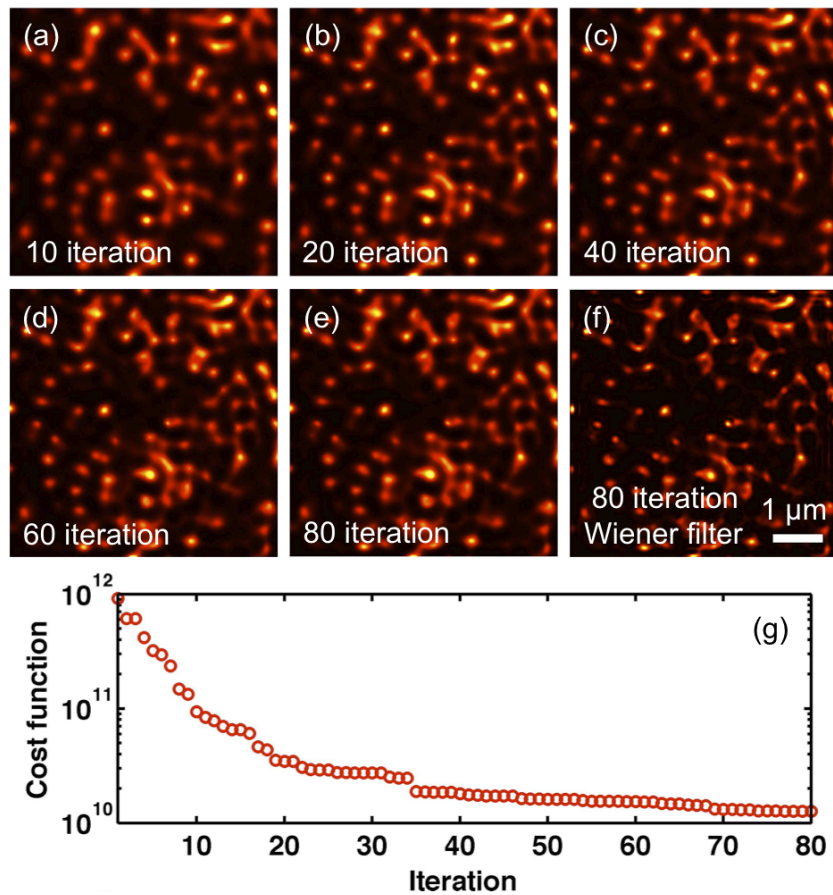


Figure 3.12: (a-e) The recovered object at different iteration steps; (f) The recovered object after applying additional Wiener filter estimated by the theoretical super-resolution psf; (g) The value of the cost function vs. the number of iterations.

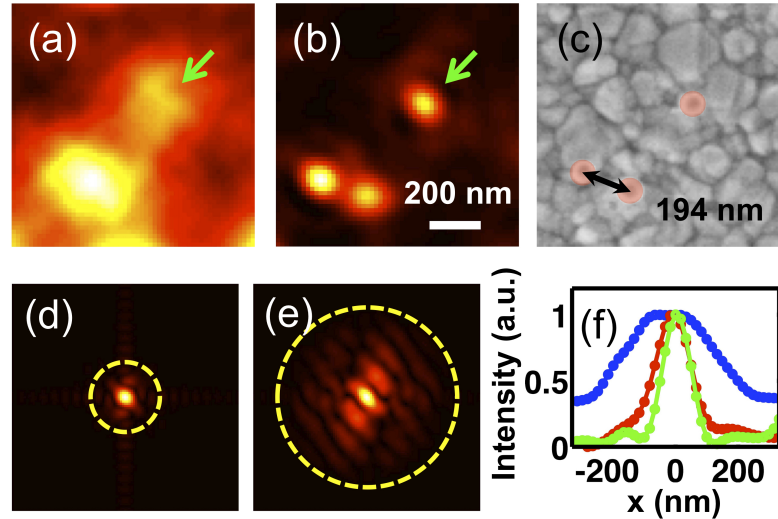


Figure 3.13: Experimental demonstration of the PSIM resolution enhancement factor through a single bead FWHM. Fluorescence beads with 100 nm diameters were used as the object. (a) Conventional epi-fluorescence image. (b) Reconstructed PSIM image. (c) The corresponding SEM image, with beads highlighted in red. (d-e) Fourier transform of (a-b), respectively. The yellow dashed circles in (d) and (e) indicating the optical transfer function (OTF) of the conventional microscope system and that of the PSIM system accordingly. (f) Fluorescence intensity cross-section comparison of the single bead indicated by the green arrows in (a-b). The red line, green line and blue line correspond to the fluorescence intensity cross-section of the reconstructed PSIM image along two perpendicular directions and that of the conventional epi-fluorescence image respectively.

in Figure 3.13 f), yielding a factor of ~ 2.7 times resolution improvement. It agrees with the theoretical 2.6 times enhancement factor estimation based on the SP wave vector ($k_{sp} = 1.44k_0$, in which k_0 is the free space wave vector of the illumination laser) and the numerical aperture of the detection objective (NA=1.0).

The comparison of the conventional epi-fluorescence image, its deconvolution and the reconstructed super-resolution image over large area is shown in Figure 3.14 a-c. Although the deconvolution image shows good resolution improvement for the isolated beads, the closely located beads still remain unresolved, as shown in Figure 3.14 b and the magnified images Figure 3.14 e and Figure 3.14 i. With the PSIM technique, the closely located beads could be resolved in the reconstructed super-resolution image, due to the frequency mixing between the object and the SPI illumination. Figure 3.14 d-g and Figure 3.14 h-k show two sets of comparison within the blue squares in Figure 3.14 a-c. Two sets of beads, with center-to-center distance below the Abbe limit of theoretical epi-fluorescence microscopy 290nm ($\lambda_{em}/2NA$), and the Abbe limit of conventional SIM microscopy 140 nm ($\lambda_{em}/[2NA + 2NA(\lambda_{em}/\lambda_{ex})]$, where λ_{em} and λ_{ex} correspond to the emission and excitation wavelength of the dye, respectively), are resolved in the PSIM super-resolution image in Figure 3.14 f and Figure 3.14 j, with beads center-to-center distance characterized by the SEM images in Figure 3.14 g and Figure 3.14 k, respectively. The corresponding PSIM image intensity curves (the red curves in Figure 3.14 l-m) clearly show two peaks, while the epi-fluorescence image and deconvolution image intensity curves (the blue and green curves in Figure 3.14 l-m) only show one peak.

3.5 Discussion

Compared with conventional epi-fluorescence microscopy, PSIM achieves about 2.7 times resolution improvement due to the small period of the SPI illumination. The resolution of PSIM is given by $\lambda_{em}/2(2NA + 2NA_{eff})$, in which NA_{eff} is defined as k_{sp}/k_{em} with k_{sp} and k_{em} representing the wave vector of the SP and emission light, respectively. The NA_{eff} is independent of the NA of the objective

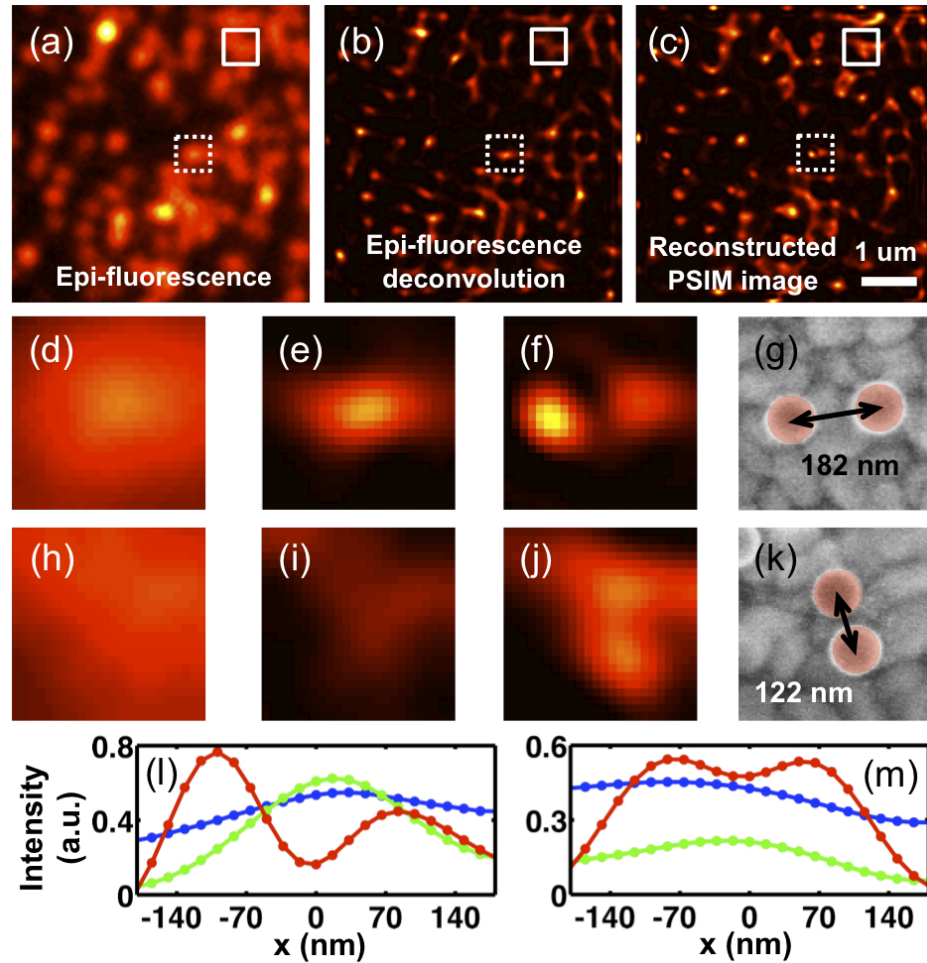


Figure 3.14: Experimental demonstration of the PSIM resolution improvement through closely located beads. Fluorescence beads with 100 nm diameters were used as the object. (a) Conventional epi-fluorescence image. (b) Its corresponding deconvolution. (c) The reconstructed PSIM image. (d-f) Detail images within the white dashed line boxes in (a-c), respectively. (h-j) Detail images within the white solid line boxes in (a-c), respectively. (g, k) The corresponding SEM images with beads highlighted in red. (l-m) The fluorescence intensity cross-section comparison. The blue, green and red lines correspond to the fluorescence cross-section in epi-fluorescence image, their corresponding deconvolved image and the PSIM reconstructed images, respectively.

and mainly determined by the SP wave vector. With proper design, such as utilizing metal/dielectric multilayer geometries, very high k_{sp} could be engineered, leading to exceptionally large NA_{eff} . Therefore, the high resolution of the PSIM is dominantly determined by the NA_{eff} . Since the imaging area commonly increases when the objective NA decreases, the PSIM technique has the unique capacity to achieve both high resolution and large imaging area, because only a relatively small NA objectives can have large NA_{eff} .

Besides its super lateral resolution imaging capability, PSIM also provides high signal-to-noise ratio (SNR) by restricting the excitation of the fluorescence to a thin region very close to the metal/dielectric interface due to the evanescent nature of the SPs. The thickness of this thin region is determined by the z intensity decay length of the SPI field, which varies from several tens of nanometers to several hundreds of nanometers, depending on the wavelength used and the designed SP wave vector. For objects of interest that only exist very close to the interface, such as plasma membranes, PSIM is a good tool to provide sub-diffraction limited lateral resolution and eliminate the unwanted fluorescence signal from the dyes that are far away from the surface.

In the demonstrated PSIM, the slit array configuration for SP excitation removes the imaging area constraint enforced by the SP decay length and extends the usable area to the whole patterned region. Since the SPI lateral translation is accomplished by tuning the incident angle, it is relatively easy to achieve high-speed, e.g. the Galvo scanning mirrors. Therefore, the demonstrated PSIM super-resolution technique has the potential to achieve high frame rate, which is valuable for super-resolution bio-specimen dynamics studies. Moreover, a thin dielectric layer (10-20 nm) could be added on top of the metal film, serving as a protection layer to separate the bio-specimens and the metal, as well as a spacer layer to reduce the quenching of the fluorescent dyes [60, 64].

3.6 Conclusion

In conclusion, we present a proof of concept experimental demonstration of the wide-field PSIM technique. Utilizing slit-coupled SPI as the illumination, PSIM is capable of achieving higher resolution than conventional SIM. Although the reconstructed PSIM images show 2.7-fold resolution improvement in the present experiment, the ultimate PSIM resolution is only limited by the achievable wave-vectors of the SPs and could be drastically improved by plasmonic mode engineering in more optimized structures. The new PSIM may lead to important applications where a high-speed super-resolution imaging tool is needed.

This work was supported by the Gordon and Betty Moore Foundation and NSF-ECCS under Grant 0969405. The authors also thank Li Wang for useful discussions on numerical reconstruction algorithms.

Chapter 3, in part, has been submitted for publication of the material as it may appear in *Nature Photonics*, 2014. Feifei Wei, Dylan Lu, Hao Shen, Weiwei Wan, Joseph Ponsetto, Eric Huang, Zhaowei Liu, “Experimental Demonstration of Wide Field Plasmonic Structured Illumination Microscopy”. The dissertation author was the first author of this paper.

Chapter 4

Plasmonic dark field (PDF) microscopy and plasmonic evanescent field (PEF) microscopy

4.1 Introduction

In this chapter, we will propose and demonstrate two related high-contrast techniques, PDF microscopy and PEF microscop. Both of these techniques utilize the evanescent field nature of SPs to form high-contrast images of the specimens. With PDF microscopy technique, we focus on the on-chip dark field imaging capability and with PEF microscopy, we mainly address its super-z resolution capability.

4.1.1 Background of dark field microscopy

Invented several hundred years ago, the optical microscope is still an irreplaceable tool for life science research today, because light is undoubtedly the best way to examine living cells noninvasively. As a special optical imaging technique, dark-field (DF) microscopy is a spectacular method to form high-contrast images of unstained transparent specimens. In order to form a bright specimen image on a dark background, oblique rays from every azimuth are allowed to strike the samples, but only light scattered from the specimens is collected by the objec-

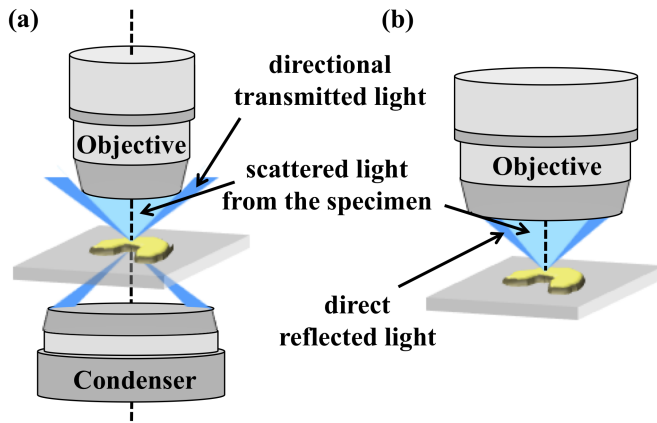


Figure 4.1: Schematics of (a) transmission dark field microscopy and (b) reflection dark field microscopy.

tive, as is shown in transmission mode in Figure 4.1. A bulky condenser, with an opaque light stop in the middle, is used to guide the illumination light and needs to be aligned precisely with a detection objective. In reflection DF microscopy, this requirement is fulfilled by a specially designed DF objective combined with a reflection cube (schematics shown in Figure 4.1 b). In both cases, the numerical aperture (NA) of the imaging objectives used in a DF microscope has to be smaller than that of the illumination optics, which in return hampers the resolution. To further utilize the imaging capability of high NA objectives, NA of 1.2-1.4 DF condensers such as paraboloid or cardioid condensers have been developed [2]. These condensers can greatly improve the imaging resolution, but they require special design and are sensitive to alignment imperfections [2, 65]. Although conventional DF microscopy has excellent imaging capability, it either requires bulky condenser optics and precise alignment or special as well as expensive DF objectives.

4.1.2 Background of total internal reflection fluorescence (TIRF) microscopy

The TIRF microscopy idea was first proposed by E.J. Ambrose in 1956 and then experimentally demonstrated by Daniel Axelrod in 1981 [66, 67]. It is capable to confine the fluorescent dye excitation to an unusually thin region close

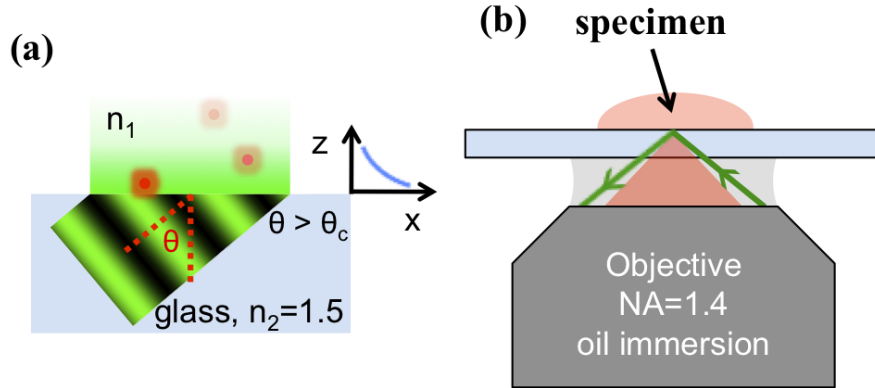


Figure 4.2: Schematics of TIRF microscopy. (a) TIRF microscopy working principle; (b) TIRF microscopy illumination and detection configuration for objective based TIRF.

to the cell/substrate interface and effectively reduce the background fluorescence emerging from dyes or auto-fluorescence deep in the cells. Because of its exceptional background elimination feature, the TIRF microscopy has been widely used for studying biochemical kinetics and single bio-molecule dynamics at cell-substrate regions since then. For example, it can be used to track secretory granules in intact cells, measure the kinetic rates of binding of extracellular and intracellular proteins to cell surface receptors, and to study membrane-proximal ionic transients etc [68].

To achieve this selective excitation of fluorophores, the TIRF microscopy replaces conventional focused light illumination with an evanescent field illumination of only the substrate-specimen interface, as shown in Figure 4.2 a. Since the fluorescent light emitted by a fluorophore is proportional to the intensity of the illumination light (square of the electric field) at that location, the closer the fluorophore to the substrate, the stronger the fluorescence light it emits. The z range of the fluorophore excitation region is about the same as the z decay length of the evanescent field, which is normally less than the wavelength of the illumination light [68]. Due to the exponential decay of the illumination light intensity, the fluorescence emitted by fluorophores that are several decay length away from the substrate surface is negligible.

To generate the desired evanescent field, the incident angle of the illumination light is set to be larger than the critical angle (θ_c) of the substrate/specimen

interface so that the illumination light undergoes total internal reflection (TIR). The TIR critical angle can be calculated by Equation (4.1), with n_1 and n_2 correspond to the refractive index of the specimen and the substrate respectively [68]. As indicated by Equation (4.1), the refractive index of the substrate, which normally is a glass cover slip ($n=1.5$), should be larger than that of the specimen for TIR occurrence. Since the refractive index of most bio-specimens are close to ~ 1.33 , the illumination light with incident angle larger than θ_c will be completely reflected back into the substrate, accompanied by the evanescent field generation at the interface. Figure 4.2 b shows a typical object based TIRF microscopy illumination and detection configuration. To ensure a large enough illumination angle, a high NA objective, such as oil immersion objective with $NA=1.4$, is normally used as the objective to deliver illumination light.

$$\theta_c = \sin^{-1}(n_1/n_2) \quad (4.1)$$

4.2 Experimental demonstration of PDF microscopy

4.2.1 Principles of PDF microscopy

To circumvent the limitations of conventional DF microscopy, several surface plasmon (SP)-related techniques, such as prism- or solid immersion lens (SIL)-based dark-field surface plasmon microscopy [69, 70], and surface-wave-enabled darkfield aperture (SWEDA) [71], have been proposed and demonstrated recently. Although these techniques have many advantages when compared with conventional DF microscopy, they also have their own limitations. For example, they require external light sources to either excite the SP field or project the image of the object to the SWEDA [69, 70, 71], which reduces the compactness of the systems. Also, the SWEDA only work at a narrow wavelength range, limited by the optimized SWEDA structure [71].

To overcome the limitations of conventional dark field microscopy and realize on-chip surface dark field imaging, we propose a novel dark field technology, plasmonic dark field microscopy (PDF) [72]. The PDF microscopy utilizes a

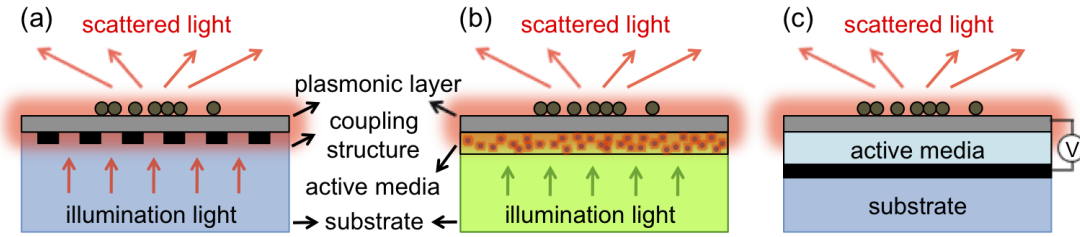


Figure 4.3: Schematics configuration of (a) grating-based passive PC; (b) fluorescence-dye-based active PC; (c) electroluminescence-material-based active PC.

chip-scale, highly integrated plasmonic multilayer structure, termed as plasmonic condenser (PC), to generate SP field for high-contrast surface dark field imaging. The evanescent field property of the SP wave assures a perfectly dark background for the far field dark field detection. The objects within the SP field region act as couplers to convert partial SP energy into propagating light. Therefore, a high-contrast dark-field image of the specimen can be formed if the propagating light is collected by conventional objectives. Since SP waves exponentially decay away from the metal surface, this technique possesses extremely high resolution and sensitivity along the z direction and is suitable for studying the dynamics of molecules and proteins that occur in the vicinity of the cell substrate interface.

In the proposed PDF microscopy, the PC is the key component for realizing the on-chip high-contrast surface dark field imaging. It should be able to couple partial input energy, either in the form of light or electricity, to SPs. Depending on whether the SPs frequency is the same as the illumination light or not, the PC condensers can be separated into two groups: passive PCs (Figure 4.3 a) or active PCs (Figure 4.3 b and Figure 4.3 c). To couple energy to SPs, the passive PCs can use either a grating or prism to compensate for the momentum mismatch between the incident photon and SPs. Contrary to passive PCs, the active PCs integrate the light source and the plasmonic layer together (labeled in Figure 4.3 b and Figure 4.3 c as active media), and utilize the near field interaction between them to couple energy to SPs. With this approach, no specific coupling structure is required as the near field of the excited optical dipoles in the active media already contains large momentum components that match those of the SPs. Therefore, the

light source should be made of luminescent materials, such as photoluminescent or electroluminescent materials, and placed within the near field of the plasmonic layer. Moreover, the direct transmission will be significantly attenuated by the metallic plasmonic layer, leading to a high image contrast.

With electroluminescence-material-based active PC, it not only eliminates the need for an external illumination light source but also significantly reduces the physical size of the light condenser. When voltage is applied between the electrodes of the active media made of an electroluminescence material, as shown in Figure 4.3 c, a portion of the energy automatically couples to SPs and the dark field image of the objects placed at the near field of the plamonic layer could be detected. Therefore, with its many favorable attributes, we mainly focus on electroluminescence-material-based active PC in this thesis. In §4.2.2, we will present the experimental demonstration of the high-contrast imaging capability of organic light-emitting diode (OLED) based active PC.

4.2.2 Experimental demonstration of OLED-based PDF microscopy

The OLED-based PC in our experiment is composed of a layer of aluminum (Al) film deposited on top of an OLED. Figure 4.4 a and Figure 4.4 b illustrate the schematic configurations of the device in top view and cross-sectional view, respectively. The device was fabricated in a standard coater under the base vacuum of about 1×10^{-6} Torr. 60 nm 2-TNATA film (4, 4', 4"-tris-[N-(2-naphthyl)-Nphenylamino]triphenylamine), 10 nm nondoped NPB film (N, N'-bis-(1-naphthyl)-N, N'-diphenyl, 1, 1'-biphenyl-4, 4'-diamine), 20 nm Alq₃ film (tris(8-quinolinolato)aluminium), and 1 nm LiF/60 nm Al film are used for hole injection, hole transport, electron transport, and electron injection layer, respectively [73, 74, 75]. When appropriate bias voltage is applied, the OLED emits white light from the indium tin oxide (ITO) side, as shown in Figure 4.4 c. Figure 4.4 d is a normalized electric luminance spectrum at 20 mA/cm² measured by a PR650 spectrophotometer with a DC source controlled by a connecting computer. The 60 nm Al film serves not only as the electrode for the OLED but also the SP

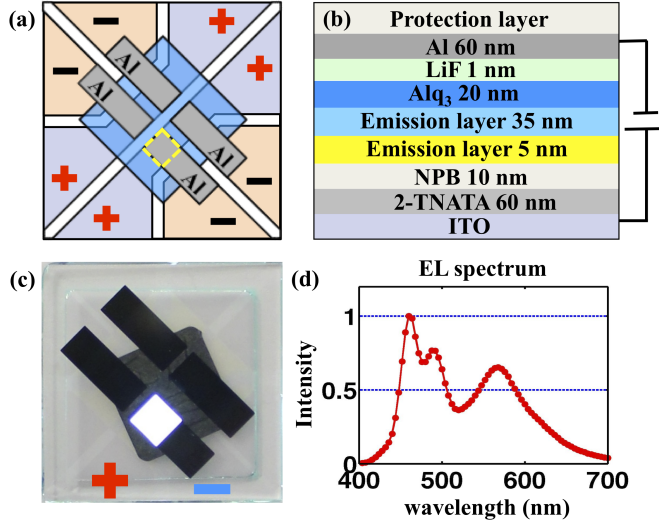


Figure 4.4: Schematic configurations of the device in (a) top view and (b) cross-sectional view. The purple area (labeled with “+”), brown area (labeled with “-”), and blue area are anode, cathode, and organic films (from 2-TNATA to Alq₃), respectively. The overlap region is the light-emitting area, indicated by the (yellow) dashed square. (c) Photo of the OLED taken from the ITO side with 6 V DC voltage applied between the electrodes. (d) Electric luminescence spectrum of the OLED at 20 mA/cm².

supporting medium, where SP can be excited through near-field coupling with the organic light-emitting molecules in the blue and yellow emission layers. Therefore, there is no visible light emission from the Al side, as the SP waves are evanescent field. The choice of white light OLED enables a broadband detection across the whole visible spectrum. Note that a thin passivation layer (40 nm NPB) was also deposited on top of the metal film to keep the organic molecules from oxygen and water vapor to reduce their damage.

To demonstrate the imaging capability of the OLED-based PC, we fabricated a single layer of two-dimensional hexagonally close-packed lattice of the polystyrene beads (diameter 2 μ m) on top of the 40 nm NPB layer using a self-assemble method. Since the illumination SP waves exist only at the metal surface, no alignment between the PC and the detection objective is needed, as opposed to the case of conventional transmission DF microscopy. The scattered white light from the polystyrene particles was collected by a standard optical microscope ob-

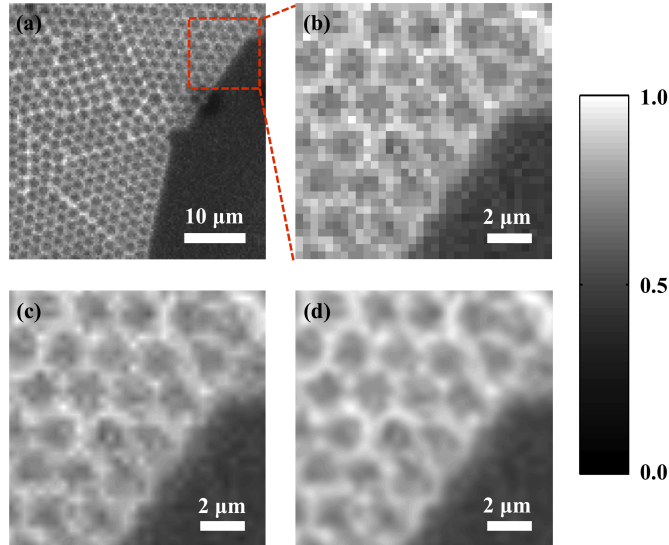


Figure 4.5: (a) Image obtained by OLED-based PDF microscopy, (b) magnified image of chosen area in (a), (c) interpolation of (b), and (d) noise reduction and deconvolution of (c). The objects are self-assembled polystyrene beads (diameter $\sim 2 \mu\text{m}$). The observed image contrast (signal/background) enhancement is approximately 9 dB compared with bright field measurement.

jective (LD EC Epiplan-NEOFLUAR, $50\times$, NA=0.55) and then captured by an Andor camera (iXonEM 897), shown in Figure 4.5 a) and Figure 4.5 b. The images express a bright signal at the region between the particles and a dim signal in the middle of the particles. The area with no presence of particles expresses as a dark background. Considering the refractive indices for polystyrene particle and air are 1.5 and 1, respectively, a bright scattering signal is obtained from the refractive index discontinuous region, which is the edges of the beads. This confirms that the image acquired is indeed a dark-field image, which is also consistent with results obtained by fluorescent-dye-based PDF microscopy demonstrated in our previous publication [72]. Therefore, OLED-based PDF microscopy is capable of forming high contrast images of objects lying close to the metal film with a highly integrated active PC without any additional light sources. We also performed an interpolation, noise reduction, and deconvolution process that have been widely applied to conventional microscopy imaging techniques, and the results are presented in Figure 4.5 c and Figure 4.5 d, respectively. The signal-to-noise (S/N) ratio as well as overall image quality shows visible improvement.

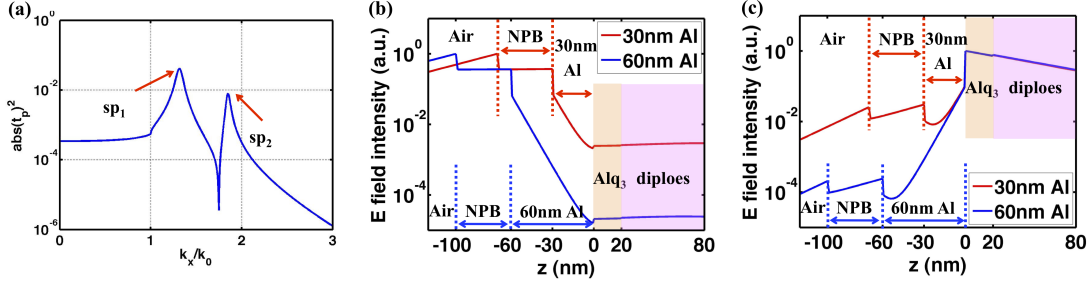


Figure 4.6: (a) Intensity transmission spectrum of p-polarized light for OLED/Al/NPB-Air structure. Two SP modes can be identified from the spectrum. (b) E field intensity distribution of SP mode 1 and (c) E field intensity distribution of SP mode 2 supported by OLED/Al/NPB-Air structure.

4.2.3 Discussion

Since the high-contrast imaging capability of the OLED-based PC comes from the evanescent nature of the SPs, the resolution along the direction perpendicular to the metal film as well as the S/N ratio strongly depend on the decay property of the SPs. Due to its short decay length, unwanted scattering from objects far from the interface can be avoided, and only objects within close vicinity to the plasmonic structure are imaged. Further increasing the z resolution and the S/N ratio can be realized by engineering the SP decay properties. Using carefully designed plasmonic structures suggested in the literature [31], the SP field with decay length much shorter than that created by other techniques such as total internal reflection can be achieved.

Besides the SP decay length, S/N ratio can also be influenced by other factors such as the coupling efficiency to SP and the surface roughness of the films. The coupling between the organic light-emitting molecules and the plasmonic structure can be calculated by modeling the device as isotropically orientated dipoles in the vicinity of a metallic structure [76, 64, 77]. As is known, there are two plasmonic modes existing in OLED/Al/protection layer-air structure, as shown in Figure 4.6 a. Figure 4.6 b and Figure 4.6 c are the E field intensity distribution of the two modes supported by the OLED/Al/NPB-Air structure.

Both of these two modes can be excited by the light emitting dipoles in OLED and contribute to the evanescent field in air. Since the wave vector of mode

2 is always larger than that of the propagating light in OLED, it can only be excited by the evanescent field generated by the light emitting dipoles. As described in reference [76], the power dissipated by the dipole in the presence of metal can be written as $P = \int_0^\infty dk_x (dP/dk_x)$, in which dP/dk_x is the power dissipation spectrum with respect to the in plane wave vector k_x and can be calculated by Equation (4.2) (equation 3.15 in reference [76]).

$$\begin{aligned} \frac{dP}{dk_x} = & \frac{\omega}{2\epsilon_1} \operatorname{Re} \left(\frac{k_x}{k_z} \left(\mu_\perp^2 k_x^2 [1 + r_{12}^P \exp(2ik_z d)] \right. \right. \\ & + \frac{1}{2} \mu_\parallel^2 k^2 [1 + r_{12}^s \exp(2ik_z d)] \\ & \left. \left. + \frac{1}{2} \mu_\parallel^2 k_z^2 [1 - R_{12}^P \exp(2ik_z d)] \right) \right) \end{aligned} \quad (4.2)$$

The energy coupling efficiency from light emitting dipole to mode 2 (η_1) is acquired by calculating the area below the corresponding peak in energy dissipation spectrum (Figure 4.7 a) and normalizing with the total energy of a dipole. Figure 4.7 b shows the energy coupling efficiency to mode 2 (η_1) as a function of dipole/Al film separation for isotropic oriented dipoles. Further more, by considering the electric intensity profile of mode 2 (shown in Figure 4.6 c), we can calculate how much (η_2) of the coupled energy is distributed to the electric field in air for mode 2 as a percentage. Therefore, the final energy coupling efficiency to the field of mode 2 in air is $\eta_1 \cdot \eta_2$, shown in Figure 4.7 c. It exponentially decays as the Al film thickness increases due to the attenuation of Al film.

For mode 1, depending on its wave vector and the refractive index of OLED material, it could be excited by either the evanescent field or the propagating light generated by the light emitting dipoles. For the former situation, the way to calculate the total energy coupling efficiency to mode 1's field in air is identical to that of mode 2. For the latter case, we need to calculate the coupling efficiency to the propagating light that has the appropriate k_x to excite mode 1 (η_0 , Figure 4.8 a) first, by integrating the corresponding area below the power dissipation spectrum (indicated by the red area in Figure 4.7 a), and normalizing with the total energy of a dipole. Then, similar to the coupling efficiency calculation for prism excitation of SP, the energy coupled to mode 1 (η_1 , Figure 4.8 b) can be calculated by considering

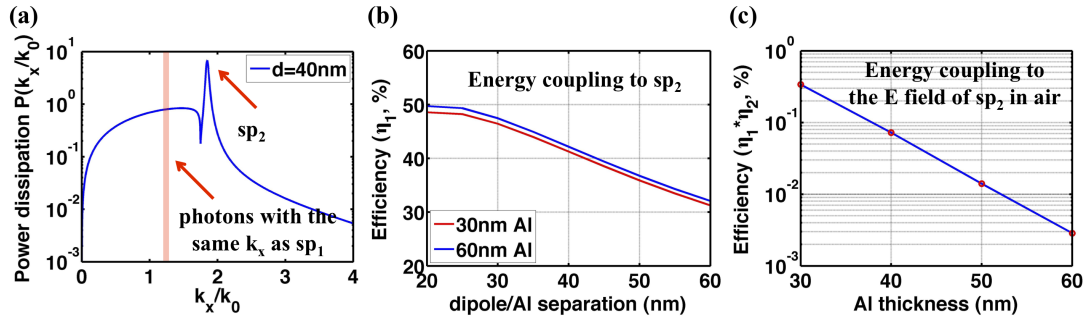


Figure 4.7: (a) Power dissipation spectrum of OLED/60nmAl/NPB-Air structure for $d=40$ nm dipole/Al film separation. (b) The energy coupling efficiency to SP mode 2 (η_1) for 30 nm and 60 nm Al film respectively. (c) The final energy coupling efficiency to the field of mode 2 in air for 40 nm dipole/Al film separation as a function of Al thickness. The dipoles with 460 nm emission peak are isotropic oriented for all calculations.

the reflectivity curve dip at the OLED/Al interface. Finally, after considering the electric intensity profile of mode 1, the total energy coupling efficiency to the field of mode 1 in air can be calculated by $\eta_1 \cdot \eta_2$, shown in Figure 4.8 c. Similar to prism excitation of SP, the total coupled energy exponentially decays as the Al film thickness increases.

After considering the contribution from both SP modes, about 0.01% of the energy is coupled to the field on the air side (Figure 4.9 the blue lower curve), and it can be increased by 100 times by reducing the Al thickness to 30 nm (Figure 4.9 the red upper curve) to decrease the attenuation of the large k vector mode through the metal film as well as increase the coupling efficiency of the relative small k vector mode, as indicated by the total intensity distribution in Figure 4.9 b. Besides decreasing the metal film thickness, the efficiency can be further increased by optimizing the dipole/metal distance and protection layer thickness as well as refractive index, replacing Al to less lossy metal such as Ag, etc.

We want to emphasize three points regarding the coupling efficiency estimation. (1) As we described above, η_1 is the percentage of the dipole energy coupled to a SP mode, and among that, η_2 percent is distributed in air by considering the field distribution. Therefore, the total energy coupling efficiency to the field of a SP mode in air can be calculated by $\eta_1 \cdot \eta_2$. (2) It is possible to design the

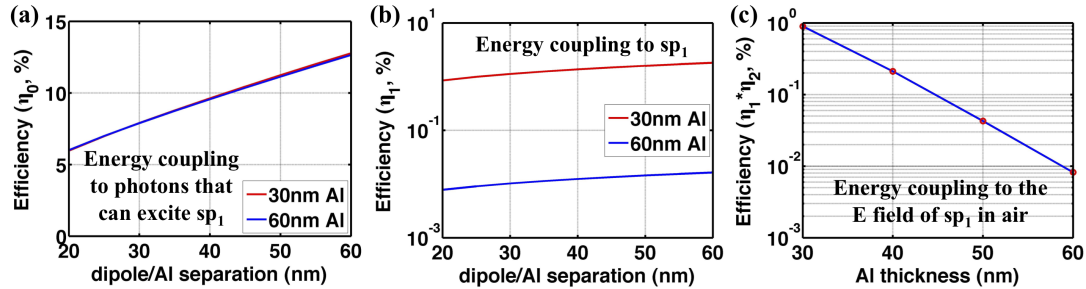


Figure 4.8: (a) The energy coupling efficiency to the propagating light that has the appropriate k_x to excite mode 1 (η_0). (b) The energy coupling efficiency to SP mode 1 (η_1) as a function of dipole/Al separation for 30nm and 60nm Al film respectively. (c) The final energy coupling efficiency to the field of mode 1 in air for 40nm dipole/Al film separation as a function of Al thickness. The dipoles with 460nm emission peak are isotropic oriented in all calculations.

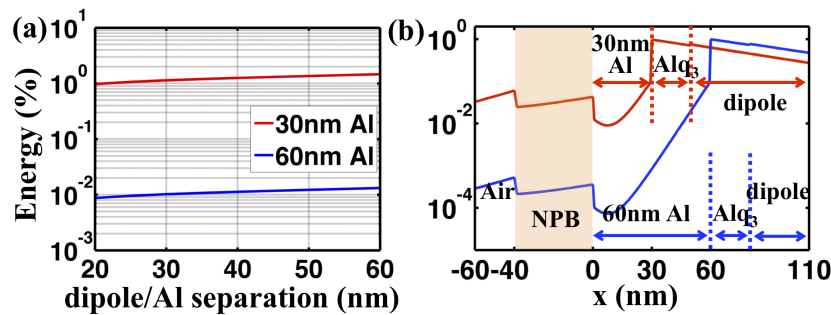


Figure 4.9: c

urve) and 60 nm Al (blue [lower] curve), respectively.] (a) Energy coupled to the field at NPB/air interface for isotropically oriented dipole with emission wavelength at 460 nm, and (b) total E field intensity profile (log scale) with contribution from both SP modes supported by 30 nm Al (red [upper] curve) and 60 nm Al (blue [lower] curve), respectively.

wave vector of SP mode 1 to be large enough so that an evanescent field, instead of propagating light, is required to excite it. This can be achieved by adjusting the refractive index as well as the thickness of protection layer. (3) The proposed device with 30nm Al film is not the final optimized structure. It just serves as the example to show one way of improving the coupling efficiency. By tuning more parameters of the OLED-PDF chip, the energy coupling efficiency could be further increased.

Besides decreasing the metal film thickness, the efficiency can be further increased by optimizing dipole/metal distance and protection layer thickness as well as refractive index, replacing Al to less lossy metal such as Ag, etc. The remaining energy is either coupled to lossy waves, emitted from the ITO side of the OLED, or transmitted through 60 nm Al film. Besides the direct transmitted light through metal film, photons rising from the scattering of the SP by surface roughness (2 nm rms for our device) also contribute to the background. The S/N ratio for the prototype device is about 2.4 and can be enhanced by increasing the coupling efficiency to SP, reducing film surface roughness by better deposition technique, etc. The dark circular defect at the top right of Figure 4.5 a is caused by the damage of the organic light-emitting molecules due to oxygen and water vapor and can be avoided by an improved passivation method [78, 79, 80]. We want to emphasize that the image acquisition time in the current demonstration can be reduced for real-time microscopy applications by increasing the coupling efficiency to SP, increasing OLED power, or using higher electronic gain for an imaging CCD detector.

As our experimental results show, OLED-based PDF microscopy is a highly compact, alignment-free approach to achieve high-contrast imaging of objects close to the interface. Since its dark-field imaging capability is enabled by evanescent field illumination instead of oblique ray illumination, OLED-based PDF microscopy does not set any constraint on the NA of the detection objectives. Therefore, the capability of high NA objectives can be fully utilized to form high-resolution DF images. Moreover, since the principles of OLED-based PDF microscopy are similar to fluorescent-dye-based PDF microscopy, it shares the same

advantages, such as large field of view, potential applications to fluorescent microscopy, etc. [68, 72, 81]. By integrating plasmonic structure with the white light OLED, white light OLED-based PC becomes more compact and can work across the whole visible spectrum compared with fluorescent-dye-based PC, prism- or SIL-based dark-field surface plasmon microscopy, and SWEDA [66, 67, 68, 69]. Through an appropriate specimen-removing process, the device can be recycled for multiple measurements. The PC can also be further integrated with other lab-on-a-chip structures, such as microfluidic channels, etc., to accomplish dark-field high contrast imaging on a multifunction chip. It may have potential applications in fields such as bio-imaging, sensing, and point-of-care diagnostics.

4.3 Numerical demonstration of PEF microscopy

4.3.1 Principles of PEF microscopy

As discussed in §4.1.2, TIRF microscopy is widely used for studying biochemical kinetics and single bio-molecule dynamics at cell-substrate regions due to its superior selective visualization capability and background fluorescence reduction ability enabled by the evanescent nature of the excitation field. Since the thickness of the fluoresphore excitation region is about the same as the z decay length of the evanescent field, TIRF microscopy with extremely short z decay length are needed for studying the dynamics of ultra-thin bio-structures such as cell membranes (thickness 5-10 nm).

In TIRF microscopy, the intensity decay length of the excitation evanescent field can be written as Equation (4.3), in which λ_0 , θ_0 , n_1 and n_2 are the wavelength of the illumination light, the illumination angle, the refractive index of the substrate media and the refractive index of the surrounding media of the object, respectively. NA_{used} represents the numerical aperture used to deliver the illumination light for evanescent field generation purpose and should be smaller than that of the NA of the object. It is clear that the intensity decay length L is eventually determined by the NA of the TIRF objective used. As the NA of the objective increases, the minimum achievable evanescent field intensity decay length

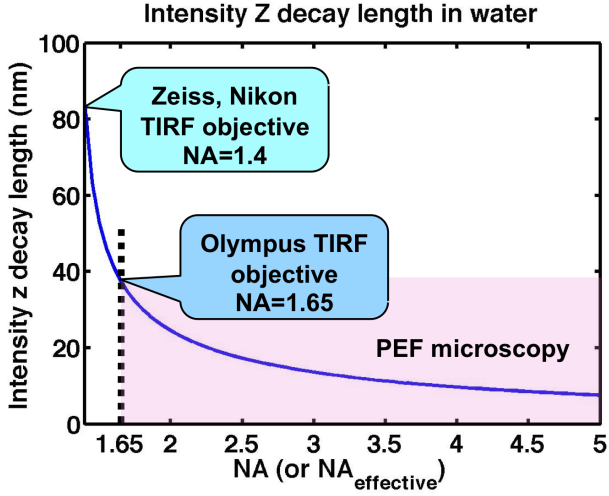


Figure 4.10: Comparison of the intensity decay length for conventional TIRF microscopy and PEF microscopy.

decreases accordingly. However, it is extremely difficult to increase the NA of the TIRF object and currently the highest NA available is 1.65, which corresponds to a minimum evanescent field intensity decay length around 40 nm for visible light.

$$L = \frac{1}{2k_z} = \frac{1}{2\sqrt{k_x^2 - n_2^2 k_0^2}} = \frac{\lambda_0}{4\pi\sqrt{NA_{\text{used}}^2 - n_2^2}} = \frac{\lambda_0}{4\pi\sqrt{n_1^2 \sin^2 \theta - n_2^2}} \quad (4.3)$$

To further reduce the intensity decay length for better background reduction purpose, evanescent field with high k_x is needed. SP is a good candidate for this purpose due to its large wave vector compared with that of the free space light (k_0). Similar to the case for conventional TIRF microscopy, the intensity decay length for SP field can be formulated as Equation (4.4), in which $NA_{\text{effective}}$ is defined as k_{sp}/k_0 . Here we propose a new surface imaging technique, termed as PEF microscopy, by taking advantage of the ultra-high wave vector supported by metamaterials. A metamaterial is an artificially designed material, which possesses exotic properties compared with natural material. Due to the advancement in nano-fabrication, metamaterials with various special properties, such as negative index of refraction, strong anisotropic permittivity etc. have been successfully engineered [82, 83, 84, 85, 86]. With proper design, the SP mode supported by metamaterials such as metal/dielectric multi-layers could reach several times of k_0 , leading to ultra-thin selective fluorescent excitation region and superior background

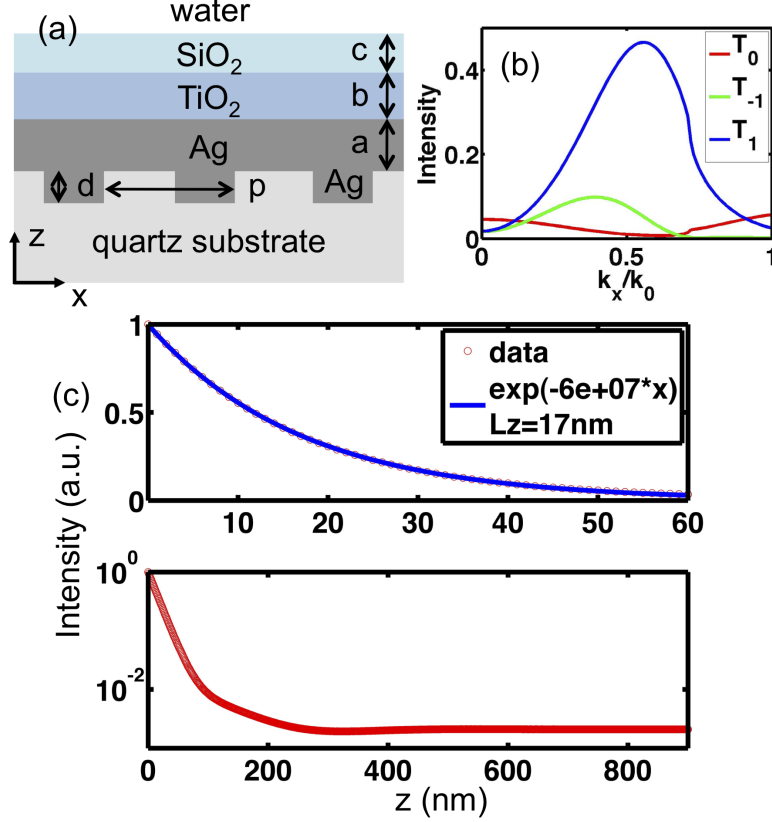


Figure 4.11: (a) Cross section view; (b) RCWA characterization; (c) Comsol characterization of the designed substrate.

fluorescence reduction capability. As shown in Figure 4.10, the intensity decay length for PEF microscopy can reach sub-20 nm, which is less than half of the minimum decay length achievable with conventional objective based TIRF.

$$L = \frac{1}{2k_z} = \frac{1}{2\sqrt{k_x^2 - n_2^2 k_0^2}} = \frac{\lambda_0}{4\pi\sqrt{NA_{\text{effective}}^2 - n_2^2}} = \frac{\lambda_0}{4\pi\sqrt{\left(\frac{k_{sp}}{k_0}\right)^2 - n_2^2}} \quad (4.4)$$

4.3.2 Numerical verification of a metamaterial substrate

Due to the split of the SP modes on a thin metal film, the modes supported by metal/dielectric multilayer forms a band with its location and bandwidth tunable by changing the thickness of the metal and dielectric films. As an example, for fixed metal layer thickness, the tangential wave vector of the supported mode increases as the thickness of the dielectric layer decreases and can reaches $\sim 4\text{-}5$

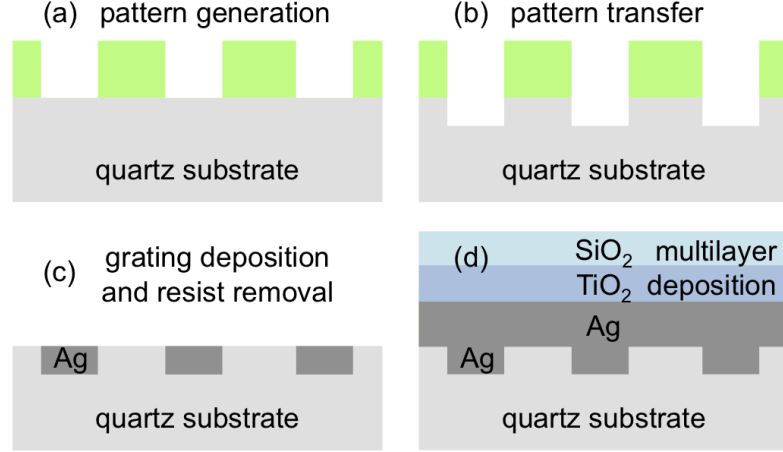


Figure 4.12: Schematics of substrate fabrication. (a) Pattern generation through electron beam lithography; (b) pattern transfer through reactive ion etching; (c) Ag grating deposition and residue resist removal; (d) multilayer deposition.

times that of the wave vector of free space photon [26]. When both the metal and dielectric film thicknesses are much smaller than the working wavelength and the number of periods is relatively large, the material property of the multilayer structure can be calculated by effective media theory shown in Equation (4.5) and Equation (4.6), in which p is the filling ratio of the metal film [31].

$$\epsilon_{eff}(x) = p\epsilon_{metal} + (1 - p)\epsilon_{dielectric} \quad (4.5)$$

$$\epsilon_{eff}(z) = (\epsilon_{metal}\epsilon_{dielectric})/((1 - p)\epsilon_{metal} + p\epsilon_{dielectric}) \quad (4.6)$$

To make sample fabrication easier, here we consider a relatively simple three-layer (Ag/TiO₂/SiO₂) structure, as shown in Figure 4.11 a. As the thickness of the TiO₂ film varies, the tangential wave vector of the supported mode changes accordingly. The thickness of the Ag film, Ag grating and the period of the grating are also optimized to maximize the ratio of the excited desired evanescent field and the direct transmission using a semi-analytical method, rigorous coupled-wave analysis (RCWA). The optimized value for parameters a , b , d and p are 45 nm, 30 nm, 45 nm and 240 nm, respectively, leading to a supported SP mode with wave vector $2.84k_0$ and 17 nm intensity decay length in water along the z direction. Finally, a thin layer (10 nm) of SiO₂ can be added on top of the structure, serving as a protection layer. The 0th, 1st and -1st order scattering intensity of the optimized

structure is represented by the red, blue and green lines, respectively, in Figure 4.11 b. Since the momentum provided by the 240 nm period grating is smaller than that of the SP mode supported ($2.84k_0$), an oblique incident is needed for efficient mode excitation, as indicated by the location of the peak of the 1st scattering intensity. To confirm the intensity decay length, the structure is simulated in Comsol, a finite element based solver for EM wave simulation. The red dots shown in Figure 4.11 c top and bottom are the electric field intensity along z direction starting from the SiO_2 /water interface. Within the first 100 nm, the intensity decay can be fitted by an exponential decay with 17 nm decay length (shown by the blue line in the top of Figure 4.11 c), which matches with the theoretical estimation calculated from the $2.84k_0$ wave vector very well. The field within the first 20 nm is two orders of magnitude stronger than that of the field at 100 nm away from the interface, leading to exceptional background elimination ability. Moreover, the designed substrate can be fabricated by standard cleanroom processes as shown in Figure 4.12. The designed grating pattern can be produced on transparent quartz substrate using electron beam lithography (EBL), followed by a reactive ion etching (RIE) to transfer the pattern on to the substrate. After depositing the Ag grating and removing residue resist, the patterned substrate is ready for $\text{Ag}/\text{TiO}_2/\text{SiO}_2$ deposition.

4.4 Conclusion

In this chapter, we presented an experimental demonstration of the high-contrast imaging capability of the PDF microscopy using a compact, highly integrated OLED-based PC chip and discussed methods of further improving its efficiency. We also discussed a highly related technique, PEF microscopy, which can achieve selective excitation of fluorescent dyes within a region significantly smaller than that of TIRF microscopy by utilizing the SPs as the excitation field. An example design with 17 nm intensity decay length is proposed and numerically verified. Due to its exceptional background reduction ability, the designed structure can be used for ultra-thin specimen, such as membrane, studies.

This work is partially supported by the start-up fund of the University of California at San Diego and the National science foundation, electrical, communication and cyber systems (NSF-ECCS) under Grant No. 0969405.

Chapter 4, in part, is a reprint of the material as it appears in Optics Letters, 2012, vol 37, no 21, 4359-4361. Feifei Wei, Yi Wan O, Guixin Li, Kok Wai Cheah and Zhaowei Liu, "Organic light-emitting-diode-based plasmonic dark-field microscopy". The dissertation author is the first author of this paper.

Chapter 5

Localized SP assisted contrast (LSPAC) microscopy

5.1 Background

Optical microscopy is an important tool for life science because light is a non-invasive probe to examine biological samples. Since the refractive indices of cells and subcellular components are very close to that of water, they normally show only small contrast under a conventional bright field microscope. Several techniques, such as dark field microscopy, phase contrast microscopy, etc. were invented to enhance the image contrast without staining the biological samples with fluorescent dye [2]. As described in §4.1.1, the dark field microscopy relies on the scattering of the illumination light due to the refractive index variation in a sample to form a high contrast image. Whereas the phase contrast microscopy, invented by physicist Frits Zernike, translates the refractive index difference between the specimen and its surrounding media into the intensity variation in the image through interference. The key idea of a phase contrast microscopy is to separate the direct transmitted light (indicated by the red beam) and the scattered light emerging from the specimen (indicated by the yellow beams) and modulate them separately. As shown in Figure 5.1, the partial coherent illumination light passing through a specially designed annulus is focused onto the specimen by a condenser.

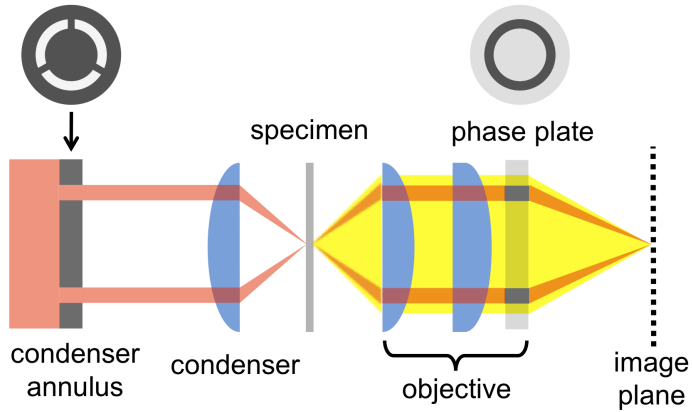


Figure 5.1: Schematics of the optical train of a phase contrast microscope

The phase plate placed inside the objective adds both intensity attenuation and phase adjustment to the direct transmitted light to match its intensity to the same order of magnitude with that of the scattered light and increasing the phase difference between them. As a result, the image formed by the interference of these two beams shows significant contrast enhancement compared with conventional wide field microscopy [2]. Although these techniques can greatly improve the image contrast, they all have corresponding limitations. For example, the dark field microscopy fails to enhance the contrast for specimens with gradual refractive index variation, due to the limited scattered light; whereas the image formed by a phase contrast microscope usually shows a characteristic halo and shade-off artifacts [2].

Localized SP is a non-propagating excitation of the conduction electrons of metallic nano-structures coupled to the electromagnetic field. Under the resonance condition, both the field inside and in the near field region outside the nano-structures are amplified. For spherical nano-particles with diameter much smaller than the wavelength of the illumination light, the localized SP resonance (LSPR) condition is given by Equation (5.1), with $\epsilon(\omega)$ and $\epsilon_d(\omega)$ representing the frequency dependent dielectric constant of the nano-particle and the surrounding dielectric, respectively [87]. Although Equation (5.1) was derived from a simplified model where nano-structures are treated as spherical particles, the underlying physics for the resonance condition are still the same. The LSPR frequency is directly related to the dielectric constant of the surrounding media and is sensitive to its variation.

For a fixed type of surrounding media, the LSPR frequency is then influenced by the shape as well as the dimensions of the nano-structures.

$$\text{Re}[\epsilon(\omega)] = -2\epsilon_d(\omega) \quad (5.1)$$

Different from conventional high contrast imaging methods, propagating surface plasmon (SP) or localized surface plasmon assisted contrast enhancement techniques were also explored during the last few decades. Since the excitation conditions for both propagating and localized SP resonances are very sensitive to the local refractive index variation [20, 87], and therefore they became widely used in label-free bio-sensing [88, 89, 90] and bio-imaging [91, 92, 93, 94, 95, 96, 97, 98, 99, 100, 101, 102]. In the field of optical microscopy, many researchers utilize this high sensitivity to enhance the image contrast [91, 92, 93, 94, 95, 96, 97, 98, 99]. A propagating SP based microscopy technique, in which the Kretschmann configuration is used to excite the SPs, was first demonstrated in late 1980s [91, 92]. Although the image contrast was improved for thin-film samples with small refractive index differences, its spatial resolution is on the order of microns, which is limited by the propagation length of SPs [91, 92]. In order to improve the spatial resolution of the propagating SP assisted microscopy, microscope objectives were used to excite propagating SP over a range of azimuthal angles, based on which several scanning or wide field approaches have been demonstrated [93, 94, 95, 96, 97, 98, 99]. The scanning approaches [93, 94, 95] achieve relatively higher spatial resolution (200-300nm), but sacrifice the image acquisition time compared with the wide field techniques [96, 97, 98, 99].

5.2 Principles of LSPAC microscopy

Compared with propagating SP assisted microscopy, the spatial resolution of localized SP assisted imaging techniques intrinsically possess high spatial resolution thanks to the field confinement and the sub-diffraction limited size of the nano-particles. Moreover, the localized surface plasmon resonance (LSPR) can be excited using a standard dark field microscope with no additional modification of the optical path, which makes the system easy to implement and use. Due to

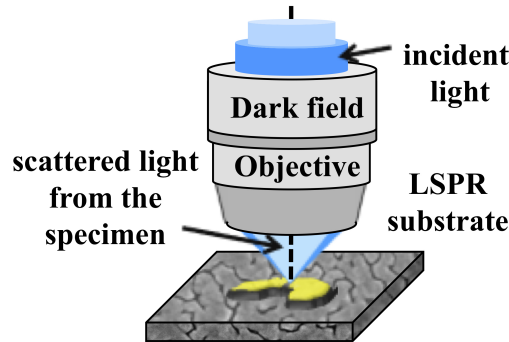


Figure 5.2: Schematic configuration of the LSPAC microscopy system

the above advantages of localized SP assisted technique, molecular-specific nano-particles have been delivered into cells to image and monitor the epidermal growth factor receptors and determine the cellular refractive indices [100, 101]. Besides free-of-move nano-particles, nano-structures patterned on substrates also became widely used for refractive index sensing [89, 102]. However, utilizing nanostructure-patterned substrates to enhance the image contrast of thin-specimen with small or gradual refractive index variation has not been demonstrated yet.

We propose a localized SP assisted contrast (LSPAC) microscopy technique to enhance the image contrast of ultra-thin transparent specimens by combining LSPR of nano-patterned metallic substrate and dark field microscopy. As is shown in Figure 5.2, the thin specimen is placed on a metallic-nanostructure patterned substrate and the light scattered by the thin-sample/patterned substrate is collected using standard dark field configuration and captured by a charge coupled device (CCD). Owing to the sensitive response of the LSPR peak wavelength with respect to the refractive index of the surrounding media, the LSPR peak wavelength of the nano-patterned metallic substrate shifts with the local refractive index variation of the thin specimen placed on top. By utilizing a monochromatic light illumination emerging from an illumination band-pass filter, this LSPR peak wavelength shift is then converted to a scattering intensity difference, which eventually leads to the enhancement in image contrast.

5.3 Experimental demonstration of LSPAC

5.3.1 Sample fabrication

The substrate for LSPAC microscopy can be any nano-patterned metallic surface that supports LSPR. Here we choose the porous silver film due to its strong scattering signal and easy fabrication process for concept demonstration purpose. A layer of 60 nm thick porous Ag film was deposited on a cover slip by electron beam deposition at a deposition rate of 0.7 \AA/s with a base pressure of $2 \times 10^{-7} \text{ Torr}$. In the deposition process, Ag normally starts the growth with sparse islands first and then individual islands gradually merge together to form a continuous film as the film thickness increases [103]. However, the slow deposition rate and small film thickness used in our samples result in lots of random distributed air gaps in the film as indicated by both the SEM and atomic force microscope (AFM) images in Figure 5.3 a and 5.3 b, respectively. In addition to the surface metrology characterization, the scattering image of the deposited porous Ag film (Figure 5.3 c) was also collected with a Zeiss LD EC Epiplan-Neofluar objective of $50\times$ and 0.55 numerical aperture (NA). Due to LSPR, purple to dark blue light were scattered strongly by the deposited porous Ag substrate. The scattering spectrum response of the substrate was then analyzed by a spectrometer. The red and blue curves in Figure 5.3 d correspond to the normalized scattering spectra of the porous Ag film with surrounding media air ($n = 1.0$) and Al_2O_3 ($n = 1.74$), respectively. As the refractive index of the surrounding medium increases, the LSPR peak shifts from a wavelength at $\sim 405 \text{ nm}$ to longer wavelength at $\sim 467 \text{ nm}$.

5.3.2 High contrast imaging capability demonstration for uniform thin object

In order to demonstrate the high contrast imaging capability of LSPAC microscopy, an array of thin Al_2O_3 square was deposited on top of both the porous Ag substrate and bare cover slips, serving as the LSPAC microscopy sample and the control sample, respectively. The $40 \mu\text{m}$ wide and $\sim 40 \text{ nm}$ thick Al_2O_3 squares

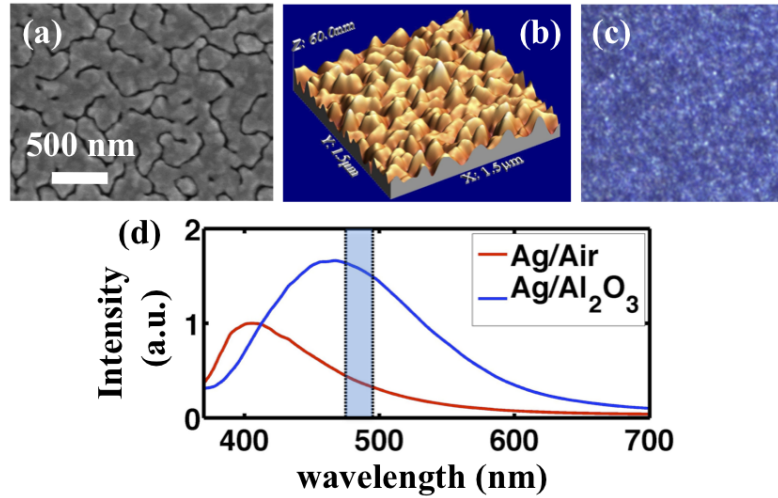


Figure 5.3: (a) SEM image, (b) AFM image, (c) dark field image and (d) the normalized scattering spectra of the deposited porous Ag film. The shaded blue region in (d) corresponds to the wavelength range of the illumination light used for the microscopy measurement.

were fabricated by electron beam deposition with a gold grid as the shadow mask. Both the LSPAC microscopy sample and the control sample were deposited in the same chamber at the same time. Based on the spectra of the porous Ag substrate, the illumination light with a wavelength close to the LSPR peak at the Al₂O₃/Ag interfaces was selected for the LSPAC sample and control sample microscopy measurements as indicated by the blue region ($485 \text{ nm} \pm 10 \text{ nm}$) in Figure 5.3 c. The reflection dark field image of both the LSPAC and the control samples were taken with a Zeiss LD EC Epiplan-Neofluar objective of $50\times$ and $\text{NA} = 0.55$; whereas the phase contrast image of the control sample was measured with a Zeiss Plan-APOCHROMAT Ph3 oil immersion objective of $100\times$ and $\text{NA} = 1.4$, due to different objective function combinations. For the scattering image of the Al₂O₃ squares deposited on the porous Ag substrate, stronger scattering signals are collected at the Al₂O₃/Ag region as shown in Figure 5.4 a. This is due to the red shift of the LSPR peak wavelength introduced by the refractive-index change of the surrounding media from 1.0 (air) to 1.74 (Al₂O₃). By using a LSPR substrate, the whole region with the same refractive index shows the same scattering intensity (Figure 5.4 a) as opposed to the image by dark field microscopy

in which only the region with refractive index discontinuity lights up. The contrast between the bright Al_2O_3 squares and the dark surrounding air region is about 60% (calculated by $(I_{max} - I_{min})/(I_{max} + I_{min})$, I_{max} and I_{min} refers to the intensity maximum and minimum, respectively), which matches the contrast calculated from the scattering spectra of the $\text{Al}_2\text{O}_3/\text{Ag}$ and Air/ Ag (Figure 5.3 c) at $485 \pm 10\text{nm}$. For the phase contrast microscopy of the control sample, the immersion oil was placed on the bottom of the cover slip, where no film was deposited. Owing to the small optical path length difference between the air and the deposited Al_2O_3 squares, the intensity contrast enhancement of the phase contrast image from the control sample is limited as shown in Figure 5.4 c. Moreover, the characteristic halo and shade-off artifacts appear on the Al_2O_3 square edges. In the reflection dark field measurement of the control sample, only the edges that correspond to refractive index discontinuity regions scatter light and form the outline of the Al_2O_3 sheets (Figure 5.4 d). The averaged cross sections of the above mentioned images (Figure 5.4 a, 5.4 c and 5.4 d) clearly show the contrast enhancement of thin object deposited on the porous Ag substrate compared with conventional phase contrast microscopy technique (Figure 5.4 b).

5.3.3 High contrast imaging capability demonstration for non-uniform thin object

As a further demonstration of the contrast enhancement capability of the proposed LSPAC microscopy, an Al_2O_3 taper was fabricated to serve as a test object with a gradual refractive-index variation. The Al_2O_3 taper was deposited on both the 60 nm thick porous Ag substrate and a bare cover slip substrate by electron beam deposition using a cover slip as the shadow mask. The shadow mask is placed 1mm above the top of the substrates so that the thickness of the deposited Al_2O_3 films gradually decreases from ~ 40 nm to 0 nm within about a $20 \mu\text{m}$ region as shown by the schematic drawing (Figure 5.5 a) and the AFM measurement (Figure 5.5 d green line). Therefore, the average refractive index of the taper region linearly decreases from 1.74 to 1.00 accordingly. Figure 5.5 b shows the same taper region deposited on the cover slip imaged by both reflection

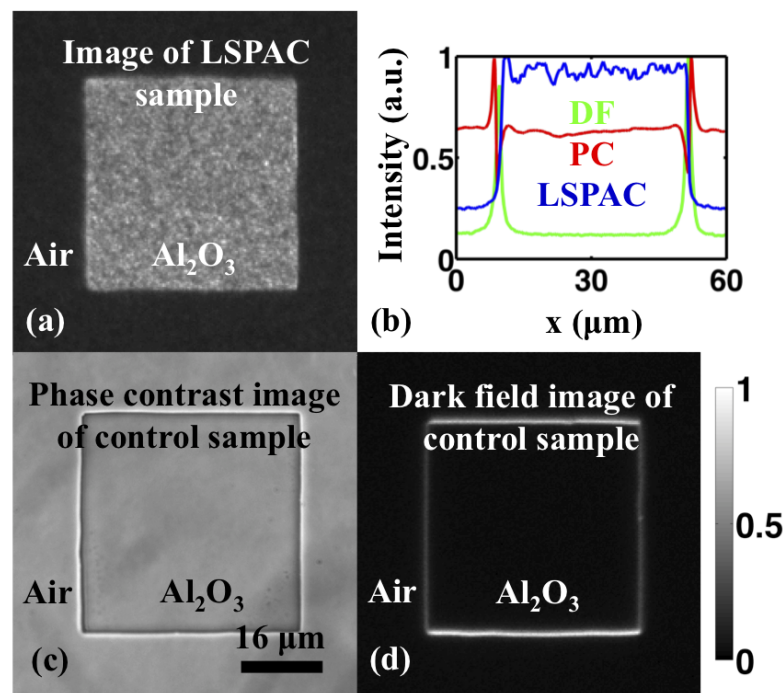


Figure 5.4: (a) The scattering image of the LSPAC sample; (b) The cross section comparison of (a, c-d); (c) The phase contrast image and (d) the reflection dark field image of the control sample.

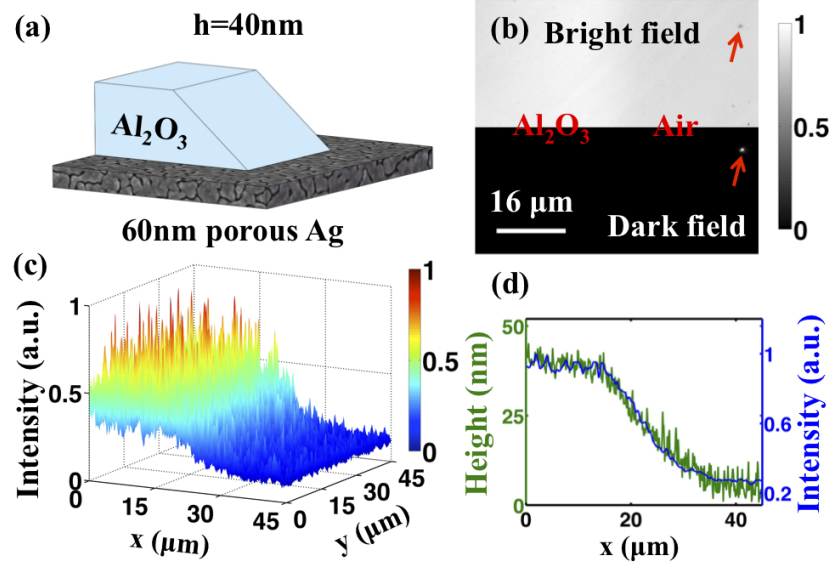


Figure 5.5: (a) Schematics of the Al_2O_3 taper deposited on the porous Ag substrate; (b) the bright field and dark field image of the Al_2O_3 taper deposited on the cover slip. (c) The LSPAC image, (d) its cross section (blue line), and AFM measurement (green line) of the Al_2O_3 taper deposited on the porous Ag substrate.

bright field (top half) and dark field (bottom half) microscopy, with the red arrows indicating the same artifact on the sample. The reflection bright field image shows a weak contrast between Al_2O_3 /coverslip region and air/cover slip region due to the small reflectivity difference between the deposited Al_2O_3 film and the cover slip. Because the scattered light from the taper deposited on the cover slip is extremely weak owing to the slow variation of the average refractive index with respect to spatial location, the taper is not visible under conventional reflection dark field microscopy. Moreover, the conventional phase contrast microscopy also fails to provide contrast enhancement due to the small optical path length variation between the deposited Al_2O_3 and air (about 30nm at the flat Al_2O_3 region).

For the Al_2O_3 taper deposited on the porous Ag substrate, the gradual decrease of the average refractive index causes the LSPR peak wavelength at the taper region to gradually shift toward shorter wavelengths. Therefore, different scattered light intensity will be collected at different locations in the taper region if a narrow band illumination light is used. Figure 5.5 c shows the normalized scattering intensity distribution at the taper region with the height and color rep-

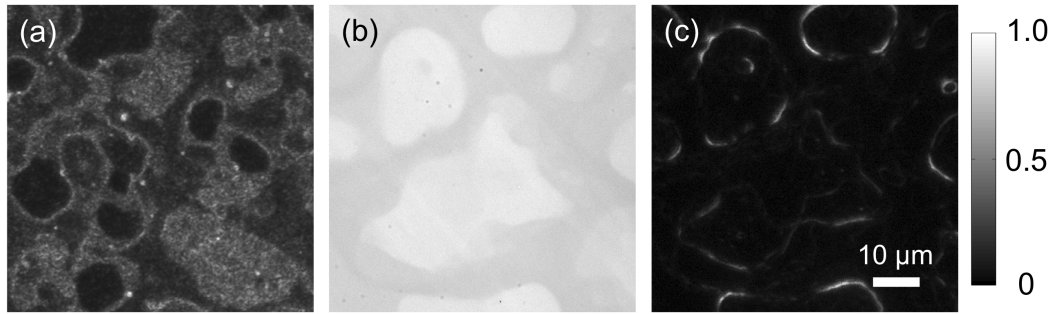


Figure 5.6: (a) The LSPAC image of the lipid deposited on a porous Ag substrate. (b) The bright field image and (c) the dark field image of the control sample with lipid deposited on a cover slip.

resenting the scattering intensity under an illumination light at $485 \pm 10\text{nm}$. Since the passing band of the filter is close to the LSPR peak for $\text{Al}_2\text{O}_3/\text{porous Ag}$ interface, the scattering intensity is the strongest at the uniform 40 nm Al_2O_3 region, and then gradually decreases at the taper area as the Al_2O_3 thickness decreases, and finally stabilizes at the air only region. If the taper region is treated as one object with fixed height and varying refractive index, the scattering intensity can be related to the local refractive index variation of the object. However, if the taper region is considered as an object with fixed refractive index but varying height, the scattering intensity reveals the height variation of the taper, as confirmed by the agreement of averaged scattering intensity at the taper region (Figure 5.5 d blue line) and the AFM height measurement of Al_2O_3 taper (Figure 5.5 d green line).

5.3.4 High contrast imaging capability demonstration using bio-specimens

Since the LSPAC microscopy can greatly enhance the image contrast of thin transparent samples, a layer of mixed lipid is chosen as the bio-samples. The mixed lipids consist of 40% (mol%) of DOPC (1,2-Dioleoyl-sn-glycero-3-phosphocholine), 40% of DPPC (dipalmitoyl-sn-glycero-3-phosphocholine) and 20% of cholesterol, and originally are dissolved in 1:1 chloroform and TFE solution. After spin coated on to both the cover slip substrate (control sample) and porous Ag substrate, the solvent evaporates and Lo/Ld (liquid ordered/ liquid disordered) domains forms

on the substrates through self-assembling. The Lo phase is rich in DPPC and cholesterol, while the Ld phase is rich in DOPC. The samples were then put into vacuum for over 24 hours to further remove traces of solvent. All the images of both the LSPAC and the control samples were taken with a Zeiss LD EC Epiplan-Neofluar objective of $50\times$ and $NA = 0.55$ under monochromatic light illumination at 485nm with 20nm bandwidth. The LSPAC image shown in Figure 5.6 a shows intensity variation between domains due to both the small refractive index as well as thickness variation between the domains formed by different types of self assembled lipid layers. However, for the self assembled lipid layered on cover slip substrate fabricated with the same process, its reflection bright field image shows very weak contrast; while the dark field image is only capable of enhancing the image contrast for refractive index change region or edges, as shown in Figure 5.6 b and Figure 5.6 c respectively.

5.4 Discussion

Since the high contrast imaging capability of the LSPAC microscopy comes from the LSPR resonance peak shift with refractive index variation in the surrounding media, the imaging contrast is mainly determined by the substrate sensitivity and the full width half maximum (FWHM) of its resonance peak. A LSPR substrate with higher sensitivity and narrower resonance peak can provide better contrast enhancement. The porous Ag substrate used in this paper serves only as a concept demonstration. It is not an optimized structure in terms of contrast enhancement due to the lack of control in the porous film metrology. High sensitivity and small resonance peak FWHM could be designed and fabricated to further improve the contrast enhancement. During the image acquisition process, the LSPR peak wavelength shift is converted to intensity variation by illumination filters. Therefore, the image contrast is also influenced by the center wavelength and the bandwidth of the band-pass filter. Using filters with appropriate center wavelength and narrower bandwidth can result in higher contrast enhancement for the same sample. Besides sensitivity, spatial resolution is also an important factor

for an imaging system. The spatial resolution of LSPAC microscopy is intrinsically diffraction limited due to the field confinement and the sub-diffraction limited size of the nanoparticles. The non-uniform scattering intensity in uniform Al₂O₃ or air region is caused by the non-uniformity of the porous Ag substrate and it can be significantly reduced by better substrate designs and fabrication techniques, such as uniform nano-disk array fabricated by electron beam lithography or nano-imprint techniques.

5.5 Conclusion

In conclusion, our experimental results show that by replacing conventional cover slips with nano-patterned metallic substrates, LSPAC microscopy is capable of acquiring wide field, high contrast images of thin specimens with small and gradual refractive index variations. Since its high contrast imaging capability originates from localized SP instead of propagating SP, its spatial resolution is sub-diffraction limited, about several hundred nanometers. Moreover, this technique is a wide field technique, and thus no scanning or additional modification of the optical path is needed for the image acquisition, which makes the system easy to implement and use. Finally, the LSPR substrate can be further integrated with other lab-on-a-chip structures for on-chip scale high contrast imaging and may have potential applications in fields such as bio-imaging and point-of-care diagnostics.

This work is partially supported by the NSF-ECCS under Grant No. 0969405.

Chapter 5, in part, is currently being prepared for submission for publication. The dissertation author was the first author of this paper.

Chapter 6

Future directions and summary

6.1 Future directions

6.1.1 Future directions for PSIM

To further increase the PSIM resolution improvement, one method is utilizing a SP mode with wave vector much higher than that of the photon to form the interference pattern. Various plasmonic substrates that support high wave vector SP modes, such as thin metal films or metal/dielectric multilayer structures, could be explored. Another method is utilizing the localized SP field for fluorescence excitation. Since the localized SP field is confined to the metallic structure, the spatial frequency of this kind of illumination can be higher than that provided by the propagating SP. Figure 6.1 show the schematics of a localized SP substrate that could be used for super-resolution microscopy. The intensity distribution of the illumination pattern can be adjusted with the illumination angle (θ, ϕ) as well as polarization direction.

In order to apply the PSIM technique in biological research, a large area biocompatible, patterned plasmonic substrate is needed. For large area substrate fabrication, nano-imprint lithography can be used for slit array pattern generation due to its low-cost and stamp reusability. Although Ag is suitable for SP generation across the visible frequency with a relatively low loss, it is toxic for bio-specimens. Therefore, a thin (10-20 nm) biocompatible dielectric protection layer, such as

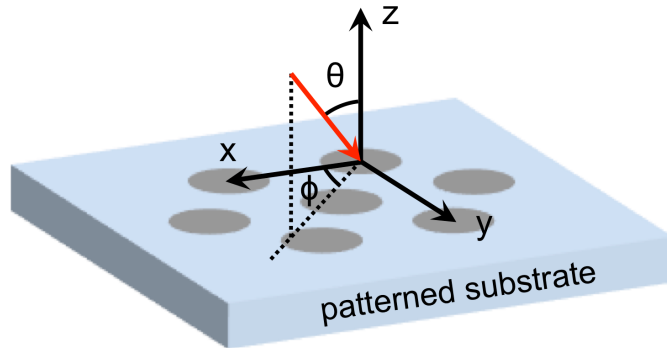


Figure 6.1: Schematics of a localized SP substrate. The blue region represents a transparent SiO_2 substrate. The hexagonal array of the gray circles corresponds to metallic nano-disks embedded into the SiO_2 substrate.

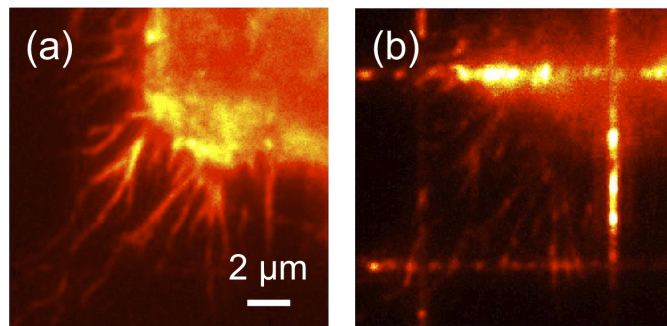


Figure 6.2: The fluorescence image of actin filaments of HeLa cells grown on a SiO_2 protected Ag plasmonic substrate, with (a) LED and (b) SPI as the excitation source, respectively.

SiO_2 , should be added on top of the patterned plasmonic substrate. To deposit a dense film as well as accurately control the protection layer thickness, the atomic layer deposition (ALD) technique can be used for the protection layer deposition, in which the film is grown one atom layer at a time.

For initial biocompatibility check, HeLa cells can be grown on the protected plasmonic substrate, serving as testing cells because they are robust. The actin filament bundles inside the cell can be labeled with fluorescent dyes, serving as the object for super-resolution microscopy (fluorescence image shown in Figure 6.2) due to their small diameter (6 nm for each actin filament) and its wide distribution in cytoplasm of eukaryotic cells.

Besides exploring the biological application of the PSIM technique, another

research direction is to increase its imaging speed. To achieve 20 super-resolution frames per second, the system needs to operate at 120 frames per second because 6 diffraction-limited images are needed for 1 super-resolution image reconstruction. A micro-controller chip or synchronized function generators can be used to synchronize the scanning mirrors and the CCD camera. Moreover, a series of tests should be performed using images taken under different exposure time for PSIM reconstruction to determine the necessary signal-to-noise ratio (SNR) for desired reconstruction resolution. As the frame rate increases, the exposure time decreases accordingly. Therefore, the illumination laser power density may need to be adjusted accordingly to achieve the necessary SNR.

6.1.2 Future directions for PDF microscopy, PEF microscopy and LSPAC microscopy

To increase the performance of the integrated PC chips for PDF microscopy, more durable light source such as light emitting diodes (LED) can also be explored. The thickness of the p-type semiconductor as well as the thickness and material of the top electrode (such as Ag, Al, Au or multi-layer structures) should be systematically studied to optimize the coupling efficiency between the light-emitting structures and the SP modes supported at the surrounding media/top electrode interface. In regard to the experimental demonstration of PEF microscopy, the substrate proposed in Chapter 4 can be fabricated by standard cleanroom electron beam lithography, etching and film deposition techniques. The intensity decay length of the excited SP field can be characterized by carefully controlling the distance between the fluorescent molecules and the substrate and monitoring their intensity. After experimentally demonstrating the super-z resolution of the designed structure and confirming its biocompatibility, cells with fluorescent-labeled membrane proteins can be grown on the substrate for protein dynamics studies. In terms of the LSPAC microscopy, the substrate uniformity as well as image contrast can be improved by replacing the porous Ag substrate, which consists of metallic scatters with varying shapes and diameters, to uniformly nano-patterned substrate such as nano-disk arrays embedded in a transparent substrate. The dimensions

of the nano-disks can be optimized to achieve shape resonance peaks and large spectrum shift with respect to the local refractive index variation.

6.2 Thesis summary

In this thesis, we demonstrated several high-resolution and high-contrast microscopy techniques by combining plasmonics with optical microscopy techniques.

The PSIM technique is a wide-field, SP assisted super-resolution imaging technique. It is capable of achieving a higher resolution improvement compared with conventional SIM. The numerical simulations shown in Chapter 2 show a 3-fold and a 4-fold resolution improvement compared with epi-fluorescence microscopy, respectively. The proof-of-concept experiment presented in Chapter 3, using slit array configuration for SPI generation, processes a 2.7-fold resolution improvement compared with epi-fluorescence microscopy. Moreover, the ultimate PSIM resolution is only limited by the achievable wave-vectors of the SPs and could be drastically improved by plasmonic mode engineering. The demonstrated PSIM may lead to important applications where a high-speed super-resolution imaging tool is needed.

The PDF microscopy and the PEF microscopy are two closely related techniques that exploit the SP evanescent field for high contrast surface imaging purpose. The PDF microscopy mainly focuses on on-chip dark field imaging with highly integrated PCs and is experimentally demonstrated in the first part of Chapter 4, using a compact white light OLED-based PC. The PCs can be further integrated with other lab-on-a-chip structures, such as micro-fluid channels or CCD sensors, to accomplish high-contrast imaging on a multifunction chip and may have potential applications in bio-imaging, sensing, and point-of-care diagnostics etc. While the PEF microscopy addresses ultra-thin region of selective fluorescent excitation for superior background fluorescence reduction by taking advantage of the ultra-high wave vector supported by metamaterials. The optimized design presented in the second part of Chapter 4 shows sub-20 nm intensity decay length, which is less than half of the minimum decay length achievable with

conventional objective based TIRF. The demonstrated PEF microscopy can potentially be used for studying the dynamics of ultra-thin bio-structures such as cell membranes (thickness 5-10 nm).

The LSPAC microscopy is a wide-field, high contrast, diffraction-limited imaging technique designed for thin transparent specimens with small or gradual refractive index variations. Its high contrast imaging capability is demonstrated in Chapter 5 using uniform thin object, non-uniform thin object, as well as self-assembled lipid films. Further more, the LSPR substrate can be further integrated with other lab-on-a-chip structures for on-chip scale high contrast imaging and may have potential application in fields such as bio-imaging and point-of-care diagnostics.

Bibliography

- [1] J. W. Goodman. *Introduction to Fourier Optics*. Roberts and Company Publishers, Greenwood Village, CO, 2005.
- [2] D. B. Murphy. *Fundamentals of Light Microscopy and Electronic Imaging*. John Wiley & Sons, Inc., Hoboken, NJ, 2001.
- [3] D. W. Pohl, W. Denk, and M. Lanz. Optical stethoscopy: Image recording with resolution $\lambda/20$. *Applied Physics Letters*, 44:651–653, April 1984.
- [4] S. W. Hell and J. Wichmann. Breaking the diffraction resolution limit by stimulated emission: stimulated-emission-depletion fluorescence microscopy. *Opt Lett*, 19(11):780–782, Jun 1994.
- [5] M. Dyba and S. W. Hell. Focal spots of size $\lambda/23$ open up far-field fluorescence microscopy at 33 nm axial resolution. *Phys. Rev. Lett.*, 88(16):163901, Apr 2002.
- [6] K. I. Willig, S. O. Rizzoli, V. Westphal, R. Jahn, and S. W. Hell. STED microscopy reveals that synaptotagmin remains clustered after synaptic vesicle exocytosis. *Nature*, 440(7086):935–939, Apr 2006.
- [7] V. Westphal, S. O. Rizzoli, M. A. Lauterbach, D. Kamin, R. Jahn, and S. W. Hell. Video-rate far-field optical nanoscopy dissects synaptic vesicle movement. *Science*, 320(5873):246–249, Apr 2008.
- [8] M. J. Rust, M. Bates, and X. Zhuang. Sub-diffraction-limit imaging by stochastic optical reconstruction microscopy (STORM). *Nat. Methods*, 3(10):793–795, Oct 2006.

- [9] B. Huang, W. Wang, M. Bates, and X. Zhuang. Three-dimensional super-resolution imaging by stochastic optical reconstruction microscopy. *Science*, 319(5864):810–813, Feb 2008.
- [10] B. Huang, S. A. Jones, B. Brandenburg, and X. Zhuang. Whole-cell 3D STORM reveals interactions between cellular structures with nanometer-scale resolution. *Nat. Methods*, 5(12):1047–1052, Dec 2008.
- [11] L. Zhu, W. Zhang, D. Elnatan, and B. Huang. Faster STORM using compressed sensing. *Nat. Methods*, 9(7):721–723, Jul 2012.
- [12] E. Betzig, G. H. Patterson, R. Sougrat, O. W. Lindwasser, S. Olenych, J. S. Bonifacino, M. W. Davidson, J. Lippincott-Schwartz, and H. F. Hess. Imaging intracellular fluorescent proteins at nanometer resolution. *Science*, 313(5793):1642–1645, Sep 2006.
- [13] S. Manley, J. M. Gillette, G. H. Patterson, H. Shroff, H. F. Hess, E. Betzig, and J. Lippincott-Schwartz. High-density mapping of single-molecule trajectories with photoactivated localization microscopy. *Nat. Methods*, 5(2):155–157, Feb 2008.
- [14] R. Heintzmann and C. Cremer. Laterally modulated excitation microscopy: improvement of resolution by using a diffraction grating. pages 185–195.
- [15] M. G. Gustafsson. Surpassing the lateral resolution limit by a factor of two using structured illumination microscopy. *J Microsc*, 198(Pt 2):82–87, May 2000.
- [16] L. Schermelleh, P. M. Carlton, S. Haase, L. Shao, L. Winoto, P. Kner, B. Burke, M. C. Cardoso, D. A. Agard, M. G. Gustafsson, H. Leonhardt, and J. W. Sedat. Subdiffraction multicolor imaging of the nuclear periphery with 3D structured illumination microscopy. *Science*, 320(5881):1332–1336, Jun 2008.
- [17] P. Kner, B. B. Chhun, E. R. Griffis, L. Winoto, and M. G. Gustafsson.

- Super-resolution video microscopy of live cells by structured illumination. *Nat. Methods*, 6(5):339–342, May 2009.
- [18] R. Heintzmann, T. M. Jovin, and C. Cremer. Saturated patterned excitation microscopy—a concept for optical resolution improvement. *J Opt Soc Am A Opt Image Sci Vis*, 19(8):1599–1609, Aug 2002.
 - [19] M. G. Gustafsson. Nonlinear structured-illumination microscopy: wide-field fluorescence imaging with theoretically unlimited resolution. *Proc. Natl. Acad. Sci. U.S.A.*, 102(37):13081–13086, Sep 2005.
 - [20] H. Raether. *Surface Plasmons on Smooth and Rough Surfaces and on Gratings*. Springer-Verlag, Berlin Heidelberg, Germany, 1988.
 - [21] I. Pockrand, J. D. Swalen, J. G. Gordon, and M. R. Philpott. *Surf. Sci.*, 74:237–244, 1978.
 - [22] C. Nylander, B. Liedberg, and T. Lind. *Sens. Actuators*, 3:79–88, 1982.
 - [23] R. P. Jeanmaire, D. L.; Van Duyne. *Electroanal. Chem.*, 84:1–20, 1977.
 - [24] J. A. Albrecht, M. G.; Creighton. *Am. Chem. Soc.*, 99(15):5215, 1977.
 - [25] M. Moskovits. Surface-enhanced spectroscopy. *Reviews of Modern Physics*, 57:783–826, July 1985.
 - [26] X. Luo and T. Ishihara. Surface plasmon resonant interference nanolithography technique. *Applied Physics Letters*, 84:4780, June 2004.
 - [27] Z.-W. Liu, Q.-H. Wei, and X. Zhang. Surface Plasmon Interference Nanolithography. *Nano Letters*, 5:957–961, May 2005.
 - [28] Y. Xiong, Z. Liu, and X. Zhang. Projecting deep-subwavelength patterns from diffraction-limited masks using metal-dielectric multilayers. *Applied Physics Letters*, 93(11):111116, September 2008.
 - [29] S. Durant, Z. Liu, J. M. Steele, and X. Zhang. Theory of the transmission properties of an optical far-field superlens for imaging beyond the diffraction

- limit. *Journal of the Optical Society of America B Optical Physics*, 23:2383–2392, November 2006.
- [30] Z. Liu, S. Durant, H. Lee, Y. Pikus, N. Fang, Y. Xiong, C. Sun, and X. Zhang. Far-Field Optical Superlens. *Nano Letters*, 7:403–408, February 2007.
- [31] Y. Xiong, Z. Liu, C. Sun, and X. Zhang. Two-Dimensional Imaging by Far-Field Superlens at Visible Wavelengths. *Nano Letters*, 7:3360–3365, November 2007.
- [32] A. Salandrino and N. Engheta. Far-field subdiffraction optical microscopy using metamaterial crystals: Theory and simulations. *Physical Review B*, 74(7):075103, August 2006.
- [33] Z. Jacob, L. V. Alekseyev, and E. Narimanov. Optical Hyperlens: Far-field imaging beyond the diffraction limit. *Optics Express*, 14:8247–8256, September 2006.
- [34] Z. Liu, H. Lee, Y. Xiong, C. Sun, and X. Zhang. Far-Field Optical Hyperlens Magnifying Sub-Diffraction-Limited Objects. *Science*, 315:1686–, March 2007.
- [35] C. Ma and Z. Liu. Focusing light into deep subwavelength using metamaterial immersion lenses. *Optics Express*, 18:4838, February 2010.
- [36] D. F. P. Pile and D. K. Gramotnev. Plasmonic subwavelength waveguides: next to zero losses at sharp bends. *Optics Letters*, 30:1186–1188, May 2005.
- [37] S. I. Bozhevolnyi, V. S. Volkov, E. Devaux, J.-Y. Laluet, and T. W. Ebbesen. Channel plasmon subwavelength waveguide components including interferometers and ring resonators. *Nature*, 440:508–511, March 2006.
- [38] J. Yao, Z. Liu, Y. Liu, Y. Wang, C. Sun, G. Bartal, A. M. Stacy, and X. Zhang. Optical Negative Refraction in Bulk Metamaterials of Nanowires. *Science*, 321:930–, August 2008.

- [39] F. Lemoult, G. Lerosey, J. de Rosny, and M. Fink. Resonant Metalenses for Breaking the Diffraction Barrier. *Physical Review Letters*, 104(20):203901, May 2010.
- [40] F. Lemoult, M. Fink, and G. Lerosey. A polychromatic approach to far-field superlensing at visible wavelengths. *Nature Communications*, 3, June 2012.
- [41] D. Lu and Z. Liu. Hyperlenses and metalenses for far-field super-resolution imaging. *Nature Communications*, 3, November 2012.
- [42] A. Sentenac, P. C. Chaumet, and K. Belkebir. Beyond the Rayleigh Criterion: Grating Assisted Far-Field Optical Diffraction Tomography. *Physical Review Letters*, 97(24):243901, December 2006.
- [43] E. Chung, Y.-H. Kim, W. T. Tang, C. J. Sheppard, and P. T. So. Wide-field extended-resolution fluorescence microscopy with standing surface-plasmon-resonance waves. *Optics Letters*, 34:2366, July 2009.
- [44] F. Wei and Z. Liu. Plasmonic Structured Illumination Microscopy. *Nano Letters*, 10:2531–2536, July 2010.
- [45] Q. Wang, J. Bu, P. S. Tan, G. H. Yuan, J. H. Teng, H. Wang, and X. C. Yuan. Subwavelength-Sized Plasmonic Structures for Wide-Field Optical Microscopic Imaging with Super-Resolution. *Plasmonics*, 7:427–433, September 2012.
- [46] B. Gjonaj, J. Aulbach, P. M. Johnson, A. P. Mosk, L. Kuipers, and A. Lagendijk. Focusing and Scanning Microscopy with Propagating Surface Plasmons. *Physical Review Letters*, 110(26):266804, June 2013.
- [47] J. T. Frohn, H. F. Knapp, and A. Stemmer. True optical resolution beyond the Rayleigh limit achieved by standing wave illumination. *Proceedings of the National Academy of Science*, 97:7232–7236, June 2000.
- [48] A. Sentenac, K. Belkebir, H. Giovannini, and P. C. Chaumet. High-resolution total-internal-reflection fluorescence microscopy using periodically nanos-

- tructured glass slides. *Journal of the Optical Society of America A*, 26:2550, November 2009.
- [49] J. Girard, G. Scherrer, A. Cattoni, E. Le Moal, A. Talneau, B. Cluzel, F. de Fornel, and A. Sentenac. Far-Field Optical Control of a Movable Subdiffractive Light Grid. *Physical Review Letters*, 109(18):187404, November 2012.
 - [50] Z. Liu, J. M. Steele, H. Lee, and X. Zhang. Tuning the focus of a plasmonic lens by the incident angle. *Applied Physics Letters*, 88(17):171108, April 2006.
 - [51] G. Bartal, G. Lerosey, and X. Zhang. Subwavelength dynamic focusing in plasmonic nanostructures using time reversal. *Physical Review B*, 79(20):201103, May 2009.
 - [52] D. B. Shao and S. C. Chen. Direct Patterning of Three-Dimensional Periodic Nanostructures by Surface-Plasmon-Assisted Nanolithography. *Nano Letters*, 6:2279–2283, October 2006.
 - [53] L. Pan, Y. Park, Y. Xiong, E. Ulin-Avila, Y. Wang, L. Zeng, S. Xiong, J. Rho, C. Sun, D. B. Bogy, and X. Zhang. Maskless Plasmonic Lithography at 22nm Resolution. *Scientific Reports*, 1, November 2011.
 - [54] M. J. Weber. *Handbook of Optical Materials*. The CRC Press, Boca Raton, FL, 2003.
 - [55] P. B. Johnson and R. W. Christy. Optical Constants of the Noble Metals. *Physical Review B*, 6:4370–4379, December 1972.
 - [56] V. Krishnamurthi, B. Bailey, and F. Lanni. Image processing in 3D standing-wave fluorescence microscopy. In C. J. Cogswell, G. S. Kino, and T. Wilson, editors, *Three-Dimensional Microscopy: Image Acquisition and Processing III*, volume 2655 of *Society of Photo-Optical Instrumentation Engineers (SPIE) Conference Series*, pages 18–25, April 1996.
 - [57] W. H. Richardson. Bayesian-Based Iterative Method of Image Restoration. *Journal of the Optical Society of America (1917-1983)*, 62:55, January 1972.

- [58] J. Yao, Y. Liu, Z. Liu, C. Sun, and X. Zhang. Surface plasmon beats formed on thin metal films. In *Society of Photo-Optical Instrumentation Engineers (SPIE) Conference Series*, volume 6323 of *Society of Photo-Optical Instrumentation Engineers (SPIE) Conference Series*, September 2006.
- [59] H. Ditlbacher, J. R. Krenn, G. Schider, A. Leitner, and F. R. Aussenegg. Two-dimensional optics with surface plasmon polaritons. *Applied Physics Letters*, 81:1762–1764, September 2002.
- [60] W. H. Weber and C. F. Eagen. Energy transfer from an excited dye molecule to the surface plasmons of an adjacent metal. *Optics Letters*, 4:236–238, August 1979.
- [61] H. Ditlbacher, J. R. Krenn, N. Felidj, B. Lamprecht, G. Schider, M. Salerno, A. Leitner, and F. R. Aussenegg. Fluorescence imaging of surface plasmon fields. *Applied Physics Letters*, 80:404, January 2002.
- [62] Cambridge Technology. <http://www.camtech.com>, Dec 2013.
- [63] E. Mudry, K. Belkebir, J. Girard, J. Savatier, E. Le Moal, C. Nicoletti, M. Alain, and A. Sentenac. Structured illumination microscopy using unknown speckle patterns. *Nature Photonics*, 6:312–315, May 2012.
- [64] W. L. Barnes. Fluorescence near interfaces: the role of photonic mode density. *Journal of Modern Optics*, 45:661–699, April 1998.
- [65] S. M. Prince and W. G. McGuigan. Alignment and tolerancing of a cardioid condenser. In *Society of Photo-Optical Instrumentation Engineers (SPIE) Conference Series*, volume 6676 of *Society of Photo-Optical Instrumentation Engineers (SPIE) Conference Series*, September 2007.
- [66] E. J. Ambrose. A Surface Contact Microscope for the study of Cell Movements. *Nature*, 178:4543, November 1956.
- [67] D. Axelrod. Cell-substrate contacts illuminated by total internal reflection fluorescence. *The Journal of Cell Biology*, 89:141–145, April 1981.

- [68] D. Axelrod. Total internal reflection fluorescence microscopy in cell biology . *Traffic*, 2:764–774, November 2001.
- [69] J. Zhang, M. C. Pitter, S. Liu, C. See, and M. G. Somekh. Surface-plasmon microscopy with a two-piece solid immersion lens: bright and dark fields. *Applied Optics*, 45:7977–7986, November 2006.
- [70] S. Balci, E. Karademir, C. Kocabas, and A. Aydinli. Direct imaging of localized surface plasmon polaritons. *Optics Letters*, 36:3401–3403, September 2011.
- [71] G. Zheng, X. Cui, and C. Yang. The ePetri dish, an on-chip cell imaging platform based on subpixel perspective sweeping microscopy (SPSM). In *Proceedings of the National Academy of Sciences 108*, volume 9043 of *Proceedings of the National Academy of Sciences 108*, 2010.
- [72] H. Hu, C. Ma, and Z. Liu. Plasmonic dark field microscopy. *Applied Physics Letters*, 96(11):113107, March 2010.
- [73] M.-F. Lin, L. Wang, W.-K. Wong, K.-W. Cheah, H.-L. Tam, M.-T. Lee, and C. H. Chen. Highly efficient and stable sky blue organic light-emitting devices. *Applied Physics Letters*, 89(12):121913, September 2006.
- [74] M.-F. Lin, L. Wang, W.-K. Wong, K.-W. Cheah, H.-L. Tam, M.-T. Lee, M.-H. Ho, and C. H. Chen. Highly efficient and stable white light organic light-emitting devices. *Applied Physics Letters*, 91(7):073517, August 2007.
- [75] C.-L. Ho, M.-F. Lin, W.-Y. Wong, W.-K. Wong, and C. H. Chen. High-efficiency and color-stable white organic light-emitting devices based on sky blue electrofluorescence and orange electrophosphorescence. *Applied Physics Letters*, 92(8):083301, February 2008.
- [76] G. W. Ford and W. H. Weber. Electromagnetic interactions of molecules with metal surfaces. *Physics Reports*, 113:195–287, November 1984.
- [77] P. Andrew and W. L. Barnes. Energy Transfer Across a Metal Film Mediated by Surface Plasmon Polaritons. *Science*, 306:1002–1005, November 2004.

- [78] S. K. Park, J. Oh, C. Hwang, J. Lee, Y. S. Yang, and H. Y. Chu. Ultrathin Film Encapsulation of an OLED by ALD. *Electrochemical and Solid-State Letters*, 8:H21–H23, 2005.
- [79] J.-S. Park, H. Chae, H. K. Chung, and S. In Lee. Thin film encapsulation for flexible AM-OLED: a review. *Semiconductor Science Technology*, 26(3):034001, March 2011.
- [80] T. Riedl, J. Meyer, H. Schmidt, T. Winkler, and W. Kowalsky. Thin Film Encapsulation of Top-Emitting OLEDs Using Atomic Layer Deposition. In *Proceedings of Solid-State and Organic Lighting*, Proceedings of Solid-State and Organic Lighting, 2010.
- [81] Daniel Axelrod. Chapter 7 total internal reflection fluorescence microscopy. In Dr. John J. Correia and III Dr. H. William Detrich, editors, *Biophysical Tools for Biologists, Volume Two: In Vivo Techniques*, volume 89 of *Methods in Cell Biology*, pages 169 – 221. Academic Press, 2008.
- [82] C. M. Soukoulis, S. Linden, and M. Wegener. Physics. Negative refractive index at optical wavelengths. *Science*, 315(5808):47–49, Jan 2007.
- [83] R. A. Shelby, D. R. Smith, and S. Schultz. Experimental Verification of a Negative Index of Refraction. *Science*, 292:77–79, April 2001.
- [84] V. A. Podolskiy and E. E. Narimanov. Strongly anisotropic waveguide as a nonmagnetic left-handed system. *Physical Review B*, 71(20):201101, May 2005.
- [85] V. A. Podolskiy, L. V. Alekseyev, and E. E. Narimanov. Strongly anisotropic media: the THz perspectives of left-handed materials. *Journal of Modern Optics*, 52:2343–2349, November 2005.
- [86] Yongmin Liu and Xiang Zhang. Metamaterials: a new frontier of science and technology. *Chem. Soc. Rev.*, 40:2494–2507, 2011.
- [87] S. A. Maier. *Plasmonics: Fundamentals and Applications*. Springer Science+Business Media LLC, New York, NY, 2007.

- [88] J. Homola. Present and future of surface plasmon resonance biosensors. *Analytical and Bioanalytical Chemistry*, 377(3):528–539, October 2003.
- [89] K. A. Willets and R. P. van Duyne. Localized Surface Plasmon Resonance Spectroscopy and Sensing. *Annual Review of Physical Chemistry*, 58:267–297, May 2007.
- [90] P. L. Stiles, J. A. Dieringer, N. C. Shah, and R. P. van Duyne. Surface-Enhanced Raman Spectroscopy. *Annual Review of Analytical Chemistry*, 1:601–626, July 2008.
- [91] B. Rothenhaeusler and W. Knoll. Surface-plasmon microscopy. *Nature*, 332:615–617, April 1988.
- [92] W. Hickel, D. Kamp, and W. Knoll. Surface-plasmon microscopy. *Nature*, 339:186, May 1989.
- [93] M. G. Somekh, S. G. Liu, T. S. Velinov, and C. W. See. Optical Vz for high-resolution 2 p surface plasmon microscopy. *Optics Letters*, 25:823–825, June 2000.
- [94] K. Watanabe, N. Horiguchi, and H. Kano. Optimized measurement probe of the localized surface plasmon microscope by using radially polarized illumination. *Applied Optics*, 46:4985–4990, August 2007.
- [95] K. Watanabe, M. Ryosuke, G. Terakado, T. Okazaki, K. Morigaki, and H. Kano. High resolution imaging of patterned model biological membranes by localized surface plasmon microscopy. *Applied Optics*, 49:887, February 2010.
- [96] G. Stabler, M. G. Somekh, and C. W. See. High-resolution wide-field surface plasmon microscopy. *Journal of Microscopy*, 214(3):328–333, May 2004.
- [97] M. Mahadi Abdul Jamil, M. Youseffi, P. C. Twigg, S. T. Britland, S. Liu, C. W. See, J. Zhang, M. G. Somekh, and M. C. T. Denyer. High resolution imaging of bio-molecular binding studies using a widefield surface plasmon

- microscope. *Sensors and Actuators B: Chemical*, 129(2):566–574, February 2008.
- [98] R. Vander and S. G. Lipson. High-resolution surface-plasmon resonance real-time imaging. *Optics Letters*, 34(1):37–39, January 2009.
- [99] M. G. Somekh, G. Stabler, S. Liu, J. Zhang, and C. W. See. Wide-field high-resolution surface-plasmon interference microscopy. *Optics Letters*, 34(20):3110–3112, January 2009.
- [100] A. C. Curry, M. Crow, and A. Wax. Molecular imaging of epidermal growth factor receptor in live cells with refractive index sensitivity using dark-field microspectroscopy and immunotargeted nanoparticles. *Journal of Biomedical Optics*, 13(1):014022, 2008.
- [101] J. Aaron, K. Travis, N. Harrison, and K. Sokolov. Dynamic Imaging of Molecular Assemblies in Live Cells Based on Nanoparticle Plasmon Resonance Coupling. *Nano Letters*, 9:3612–3618, October 2009.
- [102] M. P. Raphael, J. A. Christodoulides, S. P. Mulvaney, M. M. Miller, J. P. Long, and J. M. Byers. A new methodology for quantitative LSPR biosensing and imaging . *Anal Chem*, 83(3):1367–1373, February 2012.
- [103] R. S. Sennett and G. D. Scott. Structure of evaporated metal films and their optical properties. *Journal of the Optical Society of America (1917-1983)*, 40:203, April 1950.